Cell

Intravital observation of neuronal and immune cell dynamics in the developing mammalian brain

Graphical abstract

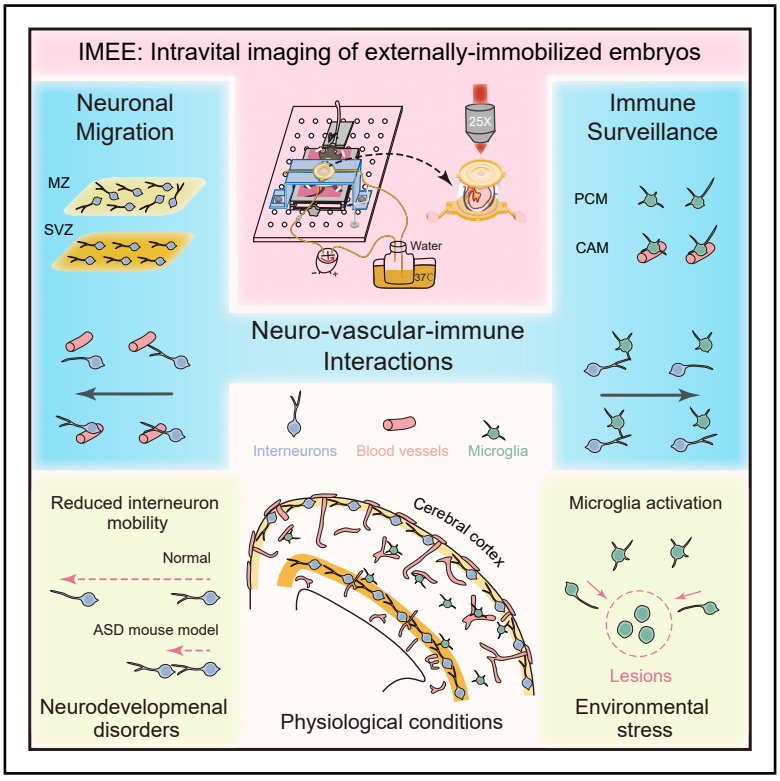

Highlights

- IMEE achieves stable, long-term intravital imaging of mouse embryos
- Distinct neuronal migration patterns are characterized *in vivo*
- Dynamic neuro-vascular-immune interactions are revealed *in vivo*
- Microglial immune surveillance and activation are demonstrated *in vivo*

Authors

Zhen Long, Yongzhen Yu, Chenyi He, ..., Zhuoru Li, Zengcai V. Guo, Da Mi

Correspondence

guozengcai@tsinghua.edu.cn (Z.V.G.), mida@tsinghua.edu.cn (D.M.)

In brief

The establishment of the intravital imaging of externally immobilized embryos (IMEE) method enables stable, high-resolution imaging of mouse embryos to investigate cellular dynamics in the developing mouse brain, including neuronal migration patterns, neurons' dynamic interactions with vasculature and microglia, and microglial surveillance behaviors under physiological conditions and environmental stress.

Long et al., 2026, Cell *189*, 528–547
January 22, 2026
https://doi.org/10.1016/j.cell.2025.11.017

CellPress

CellPress
OPEN ACCESS

Cell

Article

Intravital observation of neuronal and immune cell dynamics in the developing mammalian brain

Zhen Long,[1,2,3,5] Yongzhen Yu,[4,5] Chenyi He,[1,3,5] Linhe Xu,[1,2,3] Yiming Yan,[1,2,3] Zhuoru Li,[1] Zengcai V. Guo,[2,3,4,*] and Da Mi[1,2,3,6,*]

[1]State Key Laboratory of Membrane Biology, School of Life Sciences, Tsinghua University, Beijing 100084, China
[2]Tsinghua-Peking Center for Life Sciences, Tsinghua University, Beijing 100084, China
[3]IDG/McGovern Institute for Brain Research, Tsinghua University, Beijing 100084, China
[4]School of Basic Medical Sciences, Tsinghua University, Beijing 100084, China
[5]These authors contributed equally
[6]Lead contact
*Correspondence: guozengcai@tsinghua.edu.cn (Z.V.G.), mida@tsinghua.edu.cn (D.M.)
https://doi.org/10.1016/j.cell.2025.11.017

SUMMARY

The mammalian brain contains diverse neuronal and immune cell types that exhibit dynamic motions in response to distinct extracellular environments. However, technical limitations make it difficult to investigate complex cellular motions in the developing brain *in vivo*. Here, we establish the intravital imaging of externally immobilized embryos (IMEE) method for long-term, large-field, and deep-depth imaging of mouse embryos, excelling in viewing angle flexibility, procedural simplicity, and functional applicability. Through combining IMEE with *in utero* retro-orbital injection and topological analysis of vector fields, we characterize distinct neuronal migration patterns and illustrate interactions among neurons, immune cells, and vasculature under physiological conditions and environmental stress during brain development. Our results suggest that neuronal migration guidance and immune surveillance depend on cellular adaptation to the local environment through distinct motion patterns of somata or processes. Our findings provide critical insight into the environmentally adaptive nature of neural cells in the developmental landscape.

INTRODUCTION

The mammalian cerebral cortex is a complex, highly organized structure that is composed of neurons (excitatory glutamatergic and inhibitory GABAergic neurons) and non-neuronal cells (macroglial, immune, and endothelial cells).[1–6] During cortical development, neurons originate from progenitors within the ventricular zone (VZ) inside the brain,[7,8] whereas microglia, the brain's immune cells, arise from early erythro-myeloid progenitors (EMPs) in the yolk sac outside the brain.[9,10] The establishment of a precise spatiotemporal distribution of neurons and the unceasing protection from microglia are both indispensable for cortical development.[11–13] Dynamic cellular motions facilitate the neuronal migration and the surveillance functions of embryonic microglia.[11,13–16] On one hand, newborn neurons migrate with diverse patterns of cellular motions across different cortical zones[17–23] and interact with surrounding neurons as well as non-neuronal cells during their migration.[24–29] However, the way by which migrating interneurons interact with non-neuronal cells in their local environment, such as endothelial cells and microglia, has not been investigated *in vivo*. On the other hand, the resting microglia monitor their local environment with dynamic motions of cellular processes[16,30–35] and are ready to transform into the activated state in response to the environmental stress,[16,36–43] which is largely studied in adults. Nevertheless, as for embryonic microglia, there are few time-lapse studies of their dynamic motions in physiological environments or in response to environmental stress.

Despite the strong desire for intravital imaging of cellular dynamics, most studies resort to *ex vivo* methods, which face inevitable limitations. First, *ex vivo* studies using acute brain slices for time-lapse imaging are limited by the lack of blood flow as a result of the detachment from the vascular circulatory system.[44–48] Second, the slicing of brain tissue disrupts the central nervous system (CNS) homeostasis, in which microglia are activated in nonphysiological immune responses.[47–52] The above limitations deem *ex vivo* time-lapse methods unsuitable for studies about cellular dynamics under physiological conditions, especially those associated with blood vessels or microglia.

Existing intravital imaging methods for mouse embryos remain limited. For example, an internal immobilization strategy enables day-long observation but suffers from unstable immobilizations, restricted views, and complicated operations.[53] Existing external immobilization approaches, which involve emptying the amniotic fluid, disrupt the intrauterine environment and permit only short imaging windows.[54–59] Furthermore, these intravital imaging methods have not been optimized to visualize

vascular- or immune-related interactions in the mammalian embryonic brains.[53–59]

Here, we establish a method of intravital imaging of externally immobilized embryos (IMEE), especially for the embryonic mouse brains, which keeps the embryos developing normally in the amniotic fluid and maintains their connection with the placenta. The IMEE enables long-term, large-field, and deep-depth *in vivo* imaging of cellular dynamics in the embryonic mouse brains (E10.5–E16.5), excelling in viewing angle flexibility, procedural simplicity, and functional applicability. By combining IMEE with the *in utero* retro-orbital injection (IU-ROI) for labeling the vasculature and the topological analysis of vector fields (TVF) for delineating the motion patterns, we characterize both migration patterns of distinct neuronal populations during mouse cortical development and interneuron migration defects in an autism spectrum disorders (ASDs) mouse model, demonstrate that the migrating interneurons interact with blood vessels or microglia through contact-mediated modulation in the local environment, and illustrate the dynamic behaviors of brain immune cells under physiological conditions or environmental stress. Our results provide *in vivo* evidence showing the diverse cellular motion patterns of somata and processes across distinct extracellular environments, which has a significant implication for understanding the cellular environmentally adaptive behaviors in the context of cell migration and immune surveillance during the development of mammalian brains.

RESULTS

IMEE

We developed an easy-to-use device that allowed stable immobilization of embryonic mouse brains under two-photon microscopes for continuous intravital imaging (Figure 1). The IMEE device provides stable support, constant temperature, and continuous gas anesthesia that fits pregnant mice of different sizes (Figure 1A; Methods S1). The core immobilization component contains a donut-shaped chuck and pallet (Methods S1). The water circulation component maintains a proper temperature of the microenvironment around the embryo via a warm water current that continuously pumps through the chuck and the pallet (Figure 1B; Methods S1).

We partially strip off the uterine wall near the top of the embryonic mouse head, which is stabilized beneath the cover glass (Methods S1). The polyurethane (PU) film attached to the bottom of the pallet gives the embryo upward support (Figure 1C; Methods S1). Besides, suction from a syringe filled with warm saline solution causes the fetal membrane to slightly expand above the hole and completely seal off the chuck (Figure 1C; Methods S1). Furthermore, agarose embedment of embryos in the space between the chuck and the pallet provides surrounding support for the embryos (Methods S1).

As a result of the flexibility of the device, our IMEE method is compatible with a long prenatal developmental time window, ranging from E10.5 to E16.5, while supporting both the lateral and the top viewing angles (Figure 1D; Video S1). Chucks of suitable sizes fit embryos at different developmental time points, while all are compatible with the one-size-fits-all bracket. In addition, the simplicity of the IMEE procedure allows the rapid switching of embryos during the operation of a single pregnant mouse. Embryos with positive fluorescent signals are selected for long-term imaging via two-photon microscopy (Figure 1E). Since the amnion remained intact, embryos were kept inside the amniotic fluid under stable and appropriate temperature and humidity, which could be maintained by the IMEE device throughout the prolonged imaging duration (Methods S1).

Using the IMEE device and two-photon microscopy, we can acquire fluorescent signals within the cortical parenchyma of living embryos, where the excitation light first needs to penetrate multiple optical obstacles, such as the fetal amnion, scalp, and meninges (Figure 1F). In addition, we can identify the precise location of small image stacks by mapping them back to the three-dimensional reconstructed whole brains (Figure 1H; Video S1). Furthermore, individual image stacks acquired via IMEE can be stitched together to obtain the large-field image stacks (Figure 1G). The fluorescent signals at a parenchymal depth up to ~900 μm (limited by objective working distance and the above optical obstacles) can be observed by IMEE (Figure 1I; Video S1).

IMEE does not disrupt the embryonic development

To assess the vitality of embryos during IMEE, we used cerebral blood supply as a reliable proxy. We applied the IU-ROI with tomato lectin, previously used only in adult mice and *ex utero* embryos,[60–62] to label the embryonic vasculature *in vivo* (Figure S1A). We found that the perineural vascular plexus (PNVP) at the pial side was labeled within 10 min, including venous sinuses, veins, and arteries distributed over the meninges[63] (Figure S1B). In addition, the intraneural vascular plexus (INVP) in the brain parenchyma was clearly labeled 2 h after IU-ROI, including arterioles, venules, and capillaries (Figure S1C). Co-staining with the vascular markers IB4 and PDGFRB confirmed the complete and precise labeling of embryonic cerebral vasculature via the IU-ROI method (Figures S1D and S1E). By combining IU-ROI with IMEE (Figure S1A), we made *in vivo* observations of the real-time flowing leukocytes[64] in the superior sagittal sinus (Sss; Figure S1F; Video S1). Quantification showed stable leukocyte flow throughout the first 4 h of IMEE, with a 65% ± 1% preservation rate by the 6th hour (Figure S1G). In addition, we also continuously monitored blood flow in the Sss based on hemoglobin autofluorescence.[65] We found persistent blood flow with a visible slowdown by the 8th hour of IMEE (Video S1). Importantly, the expression of hypoxia-response genes[66] was unaltered by the 8th hour of IMEE but was significantly upregulated by the 12th hour (Figures S1H–S1L). These results indicate that mouse embryos maintain vitality without inducing a brain hypoxic response during 8 h of IMEE.

We further assessed embryonic development following 8 h of IMEE. Embryos showed no visible anatomical changes and preserved normal brain structure (Figures S2A–S2D). In addition, IMEE did not elicit an inflammatory response in the mouse embryos, as evidenced by unchanged leukocyte numbers (Figures S2E and S2F; STAR Methods), inflammatory cytokine expression[67] (Figures S2G–S2I), and microglial activation[68] (Figures S2J–S2L). Immunostaining for key developmental markers (PAX6, TBR1, OLIG2, DCX, PH3, and cleaved caspase-3) confirmed that the numbers of neural progenitors, neurons, dividing cells, and apoptotic cells were comparable between control and IMEE groups (Figures S2M–S2V). Besides,

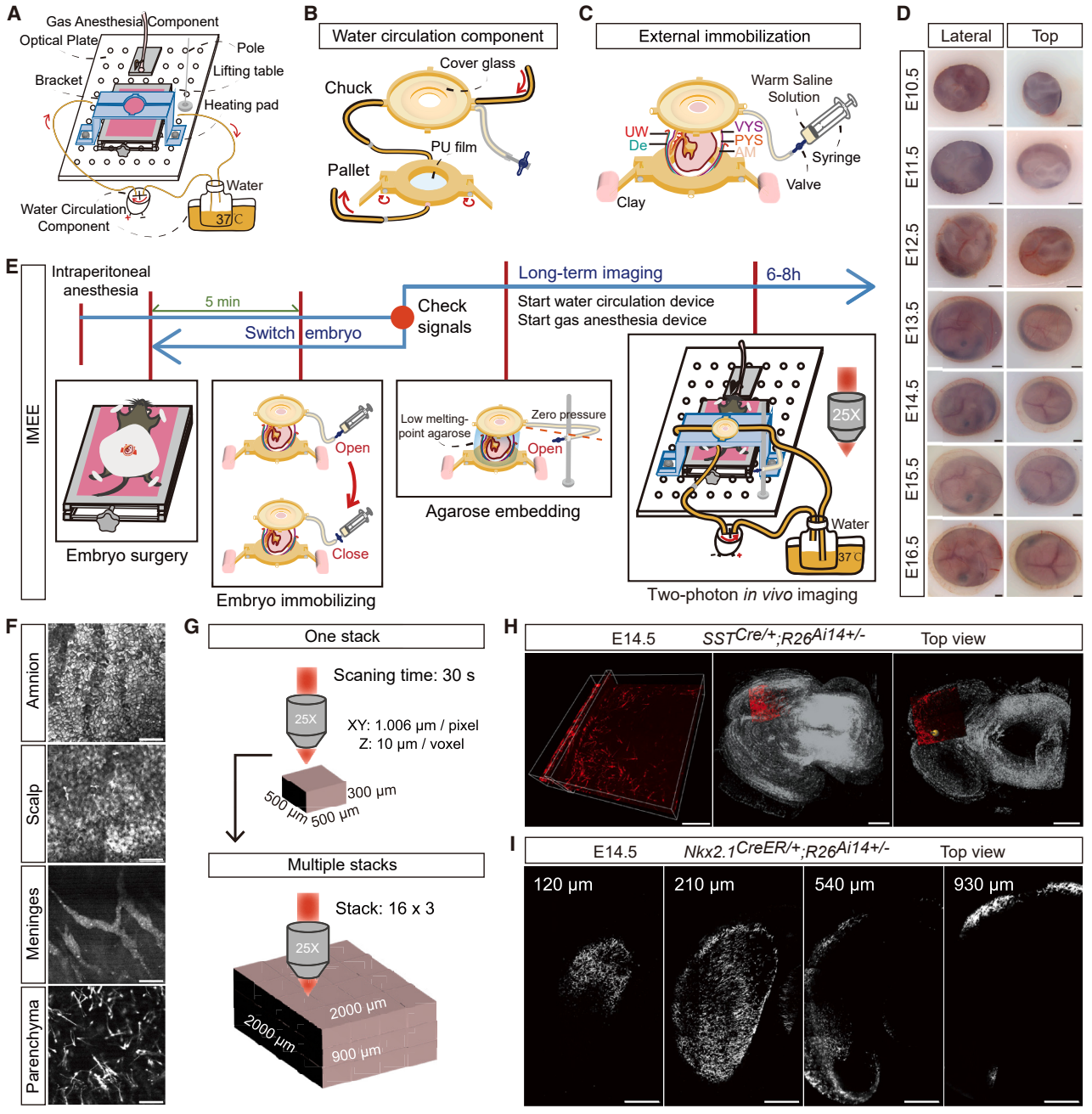

Figure 1. Intravital imaging of embryonic mouse brain

(A) IMEE device schematic.

(B) Water circulation component schematic. PU film, polyurethane film.

(C) Embryo immobilization schematic. UW, uterine wall; De, decidua; PYS, parietal yolk sac; VYS, visceral yolk sac; Am, amnion.

(D) Lateral and top views of embryonic mouse brains (E10.5–E16.5). Scale bars, 1 mm.

(E) IMEE procedure flowchart.

(F) Top view *in vivo* images of fetal amnion, scalp, meninges, and brain parenchyma of *Nkx2.1*$^{CreER+/-}$; *R26*$^{Ai14+/-}$ embryos at E14.5. Scale bars, 50 μm.

(G) IMEE single- and multi-stack imaging schematic.

(H) The top view *in vivo* image of SST^{+} interneurons at E14.5 (z = 500 μm; left), and its registration to 3D reconstructed brain (z = 1,300 μm; middle), and the cross-section (70 μm depth; right). Scale bars, 200 μm.

(I) Top view *in vivo* images of MEG-derived cortical interneurons at E14.5. Scale bars, 500 μm.

See also Figures S1 and S2, Video S1, and Methods S1.

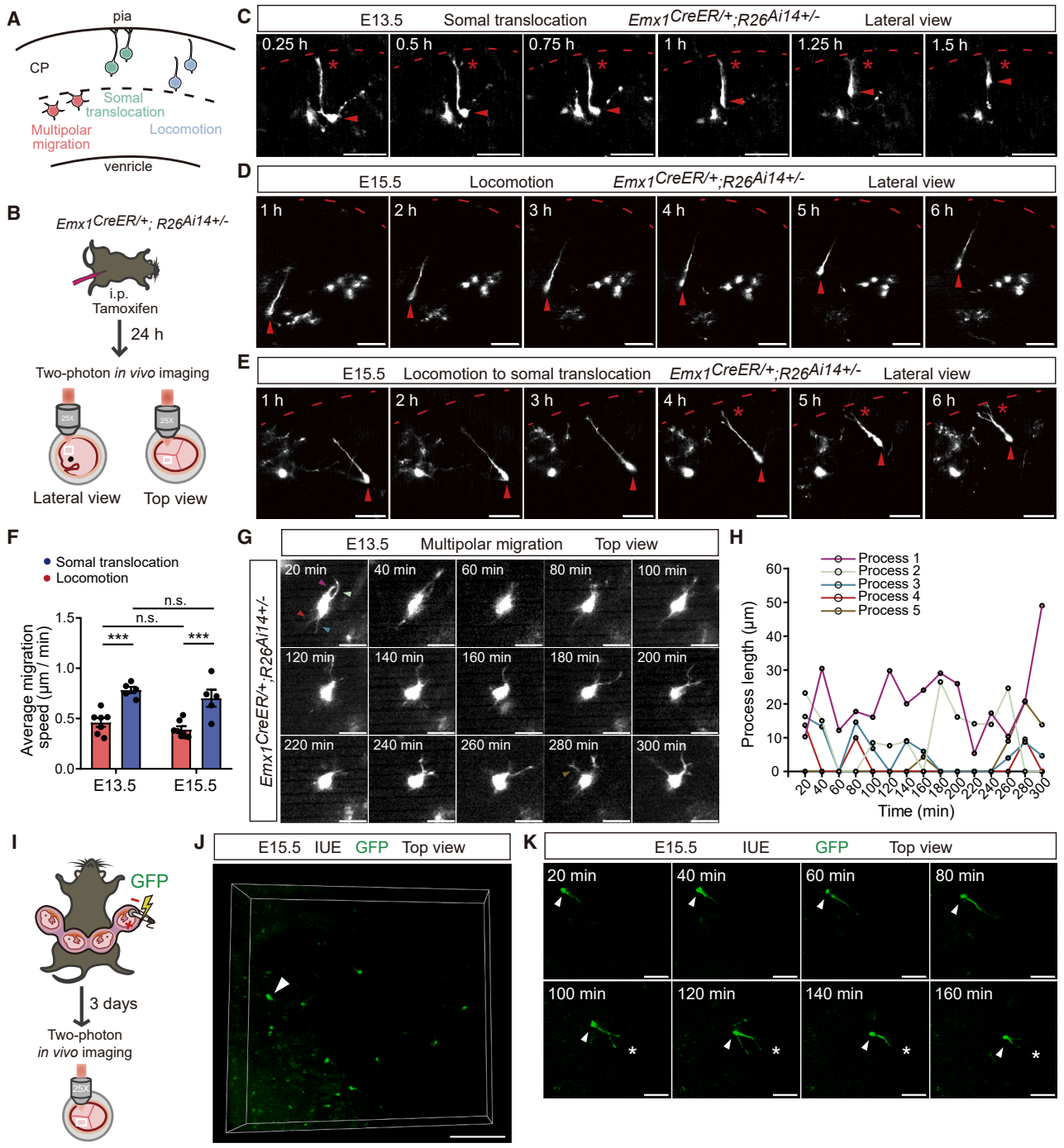

Figure 2. Intravital imaging of dynamic migration of cortical excitatory neurons in the developing mouse cortex

(A) Schematic of three migration modes of cortical excitatory neurons.

(B) Endogenous labeling of cortical excitatory neurons and two-photon *in vivo* imaging.

(C–E) The *in vivo* time-lapse sequence of somal translocation (C), locomotion (D), and locomotion-to-somal-translocation transition (E). Arrowheads, somata; asterisks, branched leading process terminals; and red dashed lines, pial surface. Scale bars, 50 μm.

(F) Quantification of migration speeds of excitatory neurons (locomotion, $n = 7$ cells at E13.5 and E15.5; soma translocation, $n = 5$ cells at E13.5 and E15.5; 2 embryos from 2 dams per group).

(G) The *in vivo* time-lapse sequence showing dynamic extensions/retractions of an excitatory neuron processes (arrowheads) during multipolar migration. Scale bars, 50 μm.

(H) Quantification of the length of each process on an excitatory neuron (shown in Figure 1G).

(legend continued on next page)

cell viability was unaltered, as measured by an acridine orange/propidium iodide (AOPI) staining assay[69] (Figures S2W and S2X). Altogether, these results demonstrate that mouse embryos maintain normal development during IMEE.

Newborn excitatory neurons exhibit diverse migration modes across different cortical zones

Previous studies using time-lapse imaging of acute cortical slices have shown that during the radial migration from the cortical germinal zone toward the pial surface, newborn excitatory neurons undergo multipolar migration before entering the cortical plate (CP) while proceeding with locomotion or somal translocation after entering the CP[17–20] (Figure 2A). However, such diverse migration modes of excitatory neurons have not been systematically characterized *in vivo*. To address this, we sparsely labeled cortical excitatory neurons whose births were timestamped by the injection of tamoxifen in the *Emx1*$^{CreERT2/+}$; *R26*$^{Ai14+/-}$ mouse embryos and performed IMEE (Figure 2B). We observed both translocating and locomoting excitatory neurons within the CP through the lateral view: translocating neurons moved radially with their leading processes' branched terminals maintaining attachment to the pial surface, while locomoting neurons had unbranched leading processes that did not reach the pial surface (Figures 2C and 2D; Video S2). In addition, we found that some neurons switched their migration modes from locomotion to somal translocation as they were approaching the pial side (Figure 2E; Video S2). The average migration speed of locomoting cells was significantly slower (26 ± 6 μm/h) than that of translocating cells (45 ± 9 μm/h) at both early and late developmental stages, and there was no change in the migration speed between different developmental stages (Figure 2F). Furthermore, we characterized the cellular dynamics of neurons undergoing multipolar migration below the CP through the top view and found that they continuously extended and retracted their processes while their somata remained in place within a 5-h time window (Figures 2G and 2H; Video S2).

It is important to note that the IMEE method is versatile and compatible with additional methods commonly used in studies of embryonic development. By combining the *in utero* electroporation (IUE) method[70] with the IMEE, we observed the excitatory neurons changing their migration modes *in vivo* (Figures 2I–2K; Video S2).

Altogether, our results not only characterize different migration modes of excitatory neurons before versus after entering the CP *in vivo* but also prove the capability of the IMEE method for observing dynamic cellular motions during the embryonic development.

Cortical interneurons exhibit diverse tangential migration patterns across different cortical zones

Unlike excitatory neurons, cortical interneurons originate from the ventral telencephalon, mostly from the medial ganglionic eminence (MGE).[71–73] These neurons initially migrate tangentially through the cortex in defined streams, including a superficial route that courses through the marginal zone (MZ) and a deep route that traverses through the subventricular zone (SVZ).[22,73–77] However, the migration patterns of cortical interneurons within these two routes have not been characterized *in vivo*. To investigate the tangential migration patterns of cortical interneurons at the cell population level, we crossed *Nkx2.1*$^{CreER+/-}$ mice, which are homozygous lethal, with *R26*$^{Ai14+/+}$ mice and switched E14.5 embryos during the IMEE until the embryo with the desired *Nkx2.1*$^{CreER+/-}$; *R26*$^{Ai14+/-}$ genotype was encountered. The MGE-derived cortical interneurons, including somatostatin-expressing (SST$^+$) and parvalbumin-expressing (PV$^+$) interneurons,[73] were densely labeled after tamoxifen injection (Figure 3A). We acquired time-lapse image stacks of entire embryonic cortical hemispheres at 20-min intervals and performed motion correction of time-lapse stacks based on boundary structures and non-specific vasculature signals (Figure 3B; Video S3; STAR Methods). By overlapping the image stacks of two adjacent time points, we found that a number of interneurons showed movements of their somata along the leading processes (Figure 3C). Interestingly, interneurons in the MZ showed tangled movements, while SVZ interneurons moved in an ordered fashion (Figure 3C). To quantify these differences, we modeled interneurons' hour-long migration trajectories at 20-min intervals (Figures 3D, S3A, and S3B) and projected them onto a two-dimensional plane parallel to the imaging view to delineate their tangential migration patterns (Figure S3C). We found significant differences in the distribution of migratory directions between MZ and SVZ interneurons, either averaged across the three time points (Figure 3E) or tested at each of the three time points (Figure S3D). Notably, we found that the MZ interneurons showed a platykurtic (flatter) distribution of migratory directions, while SVZ interneurons exhibited a leptokurtic (more peaked) distribution—consistent with our original observations (Figures 3C, 3E, and S3D). In addition, we clustered the migratory directions at different time points and found a clear correspondence within each migration route (Figure S3G). We further quantified angular and linear speed for each interneuron and found no significant difference between MZ and SVZ interneurons (Figures 3F, 3G, S3E, and S3F). Furthermore, there was no evidence of clustering for the distribution of angular or linear speeds within migration routes (Figures S3H and S3I).

To further delineate interneuron migration patterns, we constructed velocity fields at 20-min intervals based on interneuron migration trajectories projected onto the 2D plane (Figures 3H, S3J, and S3K; STAR Methods). We clustered the velocity fields at different time points and found a correspondence within each migration route (Figure 3I). Utilizing Helmholtz-Hodge decomposition (HHD),[78] each original velocity field was decomposed into three orthogonal components: a curl-free vector field,

(I) Schematic of *in utero* electroporation (IUE) labeling and two-photon *in vivo* imaging.
(J) The top view *in vivo* image of IUE-labeled excitatory neurons at E15.5 (z = 160 μm). Scale bar, 200 μm.
(K) The *in vivo* time-lapse sequence showing the locomotion-to-somal-translocation transition at E15.5. Arrowheads, soma; asterisks, branched leading process terminals. Scale bars, 50 μm.
Data: mean ± SEM (F). Statistics: two-way ANOVA followed by Bonferroni's multiple comparisons (F); ***$p < 0.001$, n.s., non significant ($p > 0.05$).
See also Video S2.

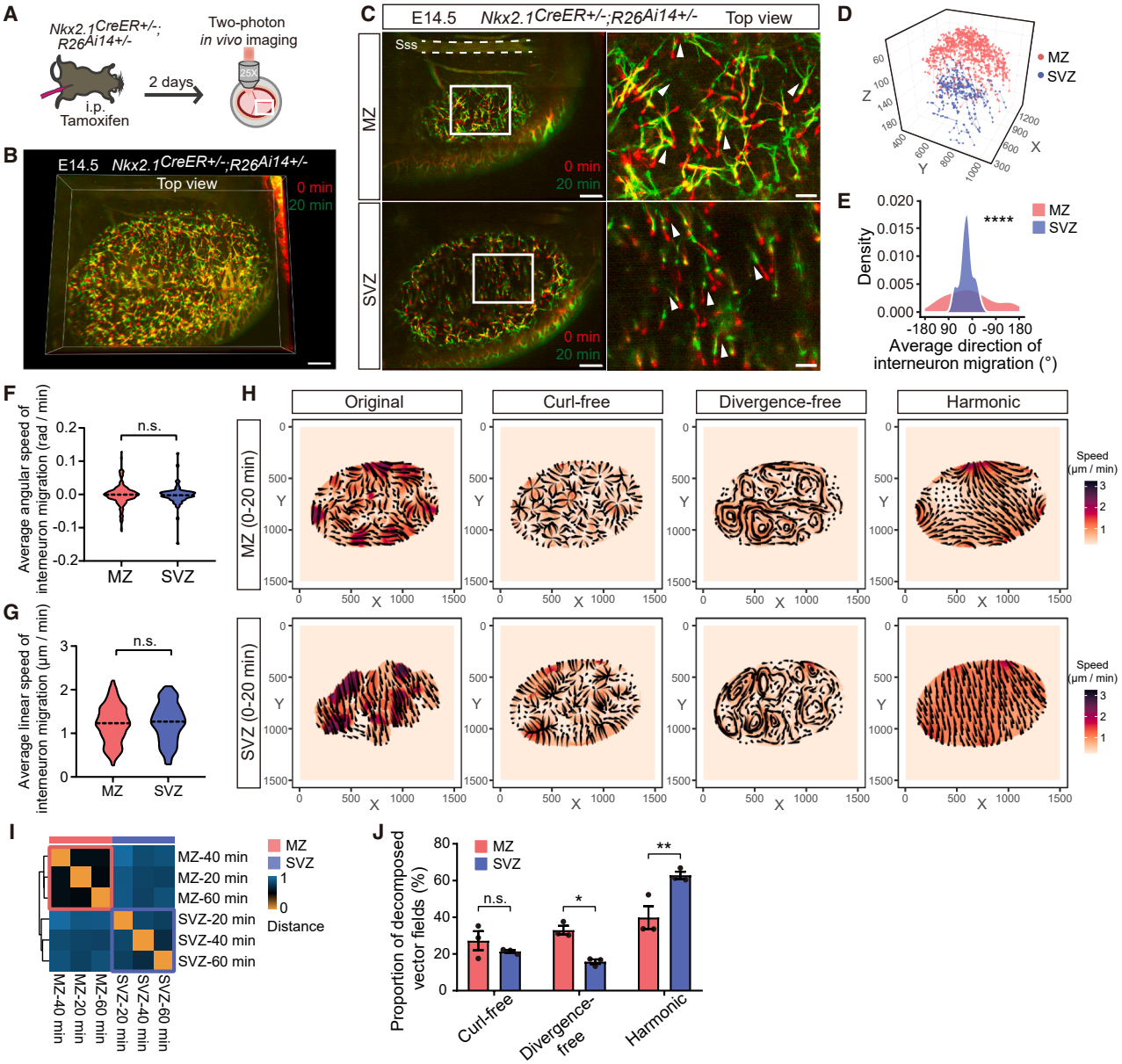

Figure 3. Intravital imaging of tangential migration of interneurons in the developing mouse cortex

(A) Endogenous labeling of MGE-derived cortical interneurons and two-photon *in vivo* imaging.

(B) The top view *in vivo* image stacks of E14.5 MGE-derived cortical interneurons overlapping observations at 0 and 20 min (z = 340 μm). Scale bar, 200 μm.

(C) Top view *in vivo* images of E14.5 MGE-derived cortical interneurons (arrowheads) migrating in the marginal zone (MZ) and subventricular zone (SVZ) overlapping observations at 0 and 20 min. Sss, superior sagittal sinuses. Scale bars, 200 μm (left) and 50 μm (right).

(D) Modeling of interneuron migration trajectories.

(E–G) Quantification of the average direction (E), angular speed (F), and linear speed (G) of each migrating interneuron (MZ, $n = 249$ cells; SVZ, $n = 70$ cells; all cells from one embryo). Values represent mean measurements per cell over 1-h imaging.

(H) Velocity fields (0–20 min) with decomposition.

(I) Heatmap illustrating the distance of the velocity fields at different time points.

(J) Contribution of decomposed components to velocity fields.

Data: violin plots (F and G) and mean ± SEM (J). Statistics: Watson test (E), Mann-Whitney U test (F and G), and two-way ANOVA followed by Bonferroni's multiple comparisons (J); ****$p < 0.0001$, **$p < 0.01$, *$p < 0.05$, n.s., nonsignificant ($p > 0.05$).

See also Figure S3 and Video S3.

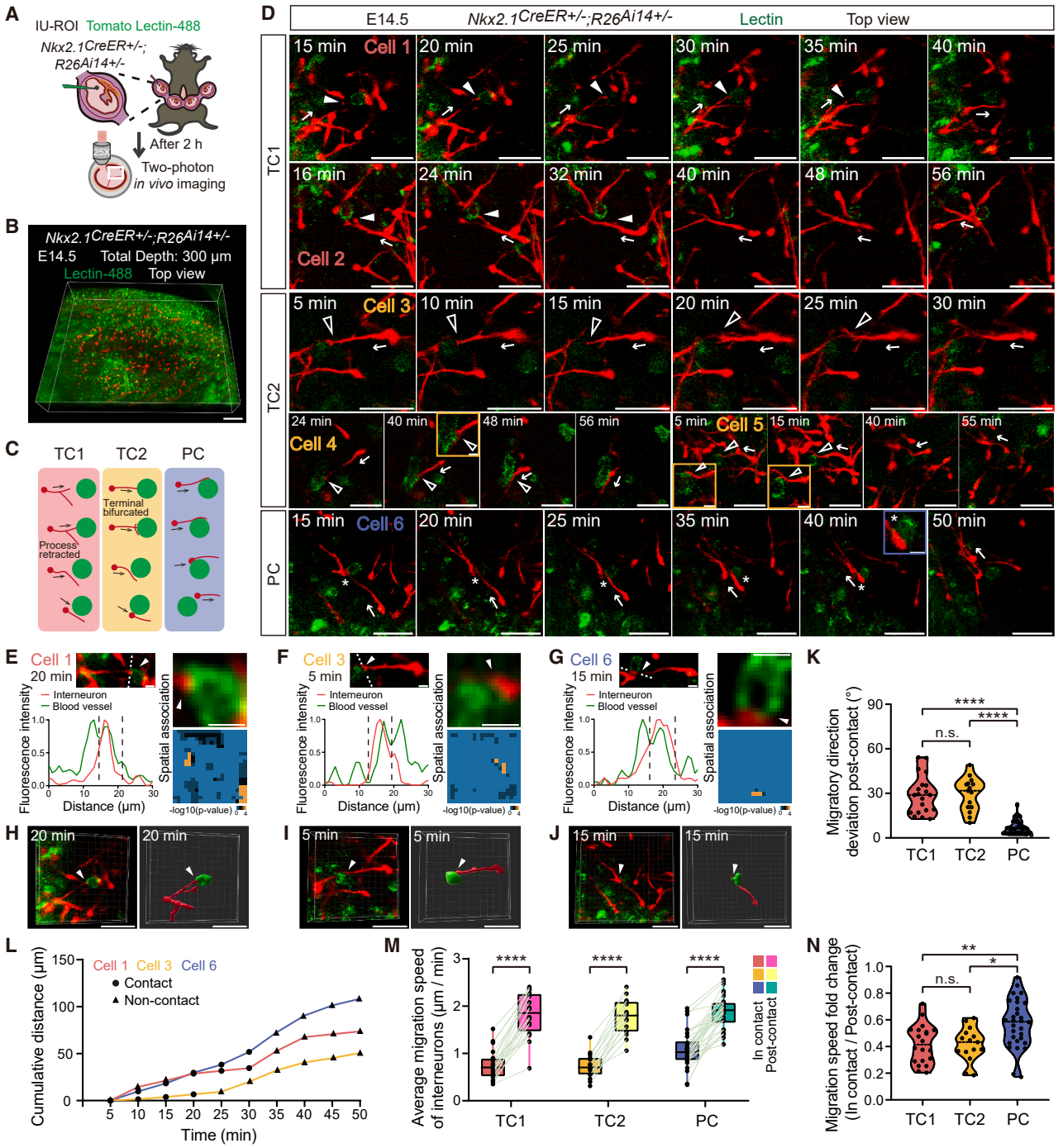

Figure 4. Intravital imaging of interactions between migrating interneurons and blood vessels in the developing mouse cortex

(A) IU-ROI labeling of blood vessels, endogenous labeling of MGE-derived cortical interneurons, and two-photon *in vivo* imaging.

(B) The top view *in vivo* image stack of blood vessels and MGE-derived cortical interneurons at E14.5 (z = 300 μm). Scale bars, 200 μm.

(C) Schematic of interneuron-vasculature contact modes: type 1/2 terminal contact (TC1, TC2) and process contact (PC).

(D) Representative *in vivo* time-lapse sequences showing interneuron-vasculature interactions at E14.5. Arrows, migratory direction; solid arrowheads, TC1 with subsequent retractions of interneuron leading process branches; hollow arrowheads, TC2 with subsequent bifurcations of interneuron leading processes; asterisks, PC. Scale bars, 50 and 10 μm (high magnification).

(E–G) Magnified images (rectangles) showing TC1 (E), TC2 (F), and PC (G) of interneurons (shown in Figure 4D) with blood vessels. Arrowheads, interneuron-vasculature contacts; distribution plots, fluorescence intensity along dotted lines of magnified images; and heatmaps, spatial associations between red and green fluorescent signals. Scale bars, 10 μm.

(legend continued on next page)

a divergence-free vector field, and a harmonic vector field (Figures 3H, S3J, and S3K; STAR Methods). The harmonic vector fields, representing homogeneous swarm movements, were more prominent in the SVZ compared with the MZ (Figure 3J). By contrast, the divergence-free vector fields (spiral swarm movements) contributed more in the MZ, while the curl-free vector fields (radiating and concentrating swarm movements) showed no significant difference between two routes (Figure 3J). These results indicate that the more heterogeneous swarm movements of MZ interneurons mainly result from the ebb of straight swarm movements and the flow of spiral swarm movements.

Altogether, these results demonstrate that the cortical interneurons migrating through the two routes exhibit equivalent properties of linear and angular speeds of migration, while the migration patterns are different—heterogeneous in the MZ with more spiral swarm movements and homogeneous in the SVZ with more straight swarm movements.

Migrating interneurons interact with blood vessels or microglia in their local environment

Next, to further characterize the cellular dynamics of tangentially migrating interneurons *in vivo*, we sparsely labeled MGE-derived cortical interneurons at E14.5 (Figures S4A and S4B). We found that individual cortical interneurons moved forward along the direction of their leading processes, while the leading process branches dynamically retracted or extended to modify the migration trajectory of interneurons (Figures S4C–S4G; Video S4). In addition, the speed of their tangential migration varied over time, ranging from 0.1 to 2.4 μm per min (Figures S4H and S4I).

Precise tangential migration of cortical interneurons during development serves as a fundamental prerequisite for circuit assembly and function of the cerebral cortex.[11,22] Previous studies have shown that early perturbations in interneuron migration are mechanistically linked to the pathogenesis of ASD.[79–82] However, *in vivo* evidence for interneuron migration defects in ASD pathogenesis is currently lacking. To address this, we investigated interneuron migration in a sodium valproate (VPA)-induced ASD mouse model[83,84] using IMEE at 5-min intervals. We found that both the migration speed of cortical interneurons and the motility of their leading processes were significantly impaired in VPA-exposed mouse embryos (Figures S4J–S4M; Video S4). Our findings offered *in vivo* evidence for interneuron migration defects in an ASD mouse model, providing crucial insights into the etiology of ASD.

One potential way of regulating interneuron migratory trajectories involves their dynamic interactions with non-neuronal cells in the local environment.[27–29] Although the guidance role of oligodendrocyte precursors in interneuron migration has been characterized *ex vivo*,[27–29] the roles of other non-neuronal cells, such as endothelial cells and microglia, have not been investigated, as their physiological states are disrupted in *ex vivo* models.[44–52] To observe the interneuron-vasculature interaction *in vivo*, we labeled MGE-derived cortical interneurons and brain vasculature in *Nkx2.1*$^{CreER+/-}$; *R26*$^{Ai14+/-}$ embryos (Figure 4A). We then captured large-field image stacks at 5–8 min intervals from the top viewing angle (Figure 4B). Building on our *in vivo* observations, we classified interneuron-vasculature interactions into three distinct modes by leading process dynamics: (1) type 1 terminal contact (TC1), characterized by leading process terminal contact with vascular surfaces followed by leading process branch retraction; (2) type 2 terminal contact (TC2), involving terminal-vasculature contact followed by the bifurcation of a single leading process; and (3) process contact (PC), featuring sustained leading process-vasculature interaction enabling unidirectional sliding of interneurons along vascular surfaces (Figures 4C and 4D; Video S5). Direct cell-cell contacts were validated through colocalization analyses of fluorescence intensity and spatial associations (Figures 4E–4G; STAR Methods) and three-dimensional reconstructions (Figures 4H–4J). Furthermore, to systematically characterize the impact of neurovascular interactions on the migrating interneurons, we tracked interneuron migration (Figure 4L) and quantified their migratory directions and speeds during and after contact. Notably, all modes of contact significantly slowed interneuron migration (Figure 4M), with TC1 and TC2 causing greater deceleration than PC (Figure 4N). Interneurons also exhibited significant migratory direction deviations following TC1 and TC2 (Figure 4K). These deviations resulted from either retraction of leading process branches, enabling migration redirection to follow other pre-existing branches after TC1, or bifurcation of leading processes, facilitating reorientation to follow newly generated leading process branches after TC2 (Figure 4D; Video S5). By contrast, after PC, interneurons slide along the vascular surface with minimal trajectory deviation, accompanied by somatic deformation (Figures 4D and 4K; Video S5). Together, these results reveal that during mouse cortical development, migrating interneurons exhibit distinct contact-modulated behaviors to navigate the local environment, away from blood vessels.

To observe the interneuron-microglia interaction *in vivo*, we crossed *Nkx2-1*$^{CreER+/-}$;*R26*$^{Ai14+/+}$ mice, for the labeling of interneurons, with *Cx3cr1*$^{GFP+/+}$ mice, which we validated against P2Y12^{+} cells in the brain parenchyma for the labeling of microglia[85,86] (Figures 5A, S6A, and S6B). We performed IMEE at E14.5 from the top viewing angle, capturing large-field image stacks at 5–10 min intervals (Figures 5A and 5B). We found that some migrating interneurons made terminal contact (TC)

(H–J) The top view *in vivo* image stack (z = 20 μm) showing interneuron-vasculature contacts (arrowheads) in three-dimensional space (left) and its surface rendering (right). Scale bars, 50 μm.

(K, M, and N) Quantification of the migratory direction deviation (K), average migration speed (M), and migration speed fold change (N) of each migrating interneuron in contact with a blood vessel versus post-contact (TC1, n = 20 cells; TC2, n = 15 cells; PC, n = 30 cells; 4 embryos from 4 dams).

(L) Quantification of cumulative distances of cell 1, cell 2, and cell 3 (shown in Figure 4D).

Data: violin plots (K and N) and boxplots (M). Statistics: conditional permutation test (10,000 iterations, E–G), Kruskal-Wallis H test followed by Dunn's multiple comparisons (K and N), and Wilcoxon signed-rank test (M); ****$p < 0.0001$, **$p < 0.01$, *$p < 0.05$, n.s., nonsignificant ($p > 0.05$).

See also Figures S4 and S5 and Video S5.

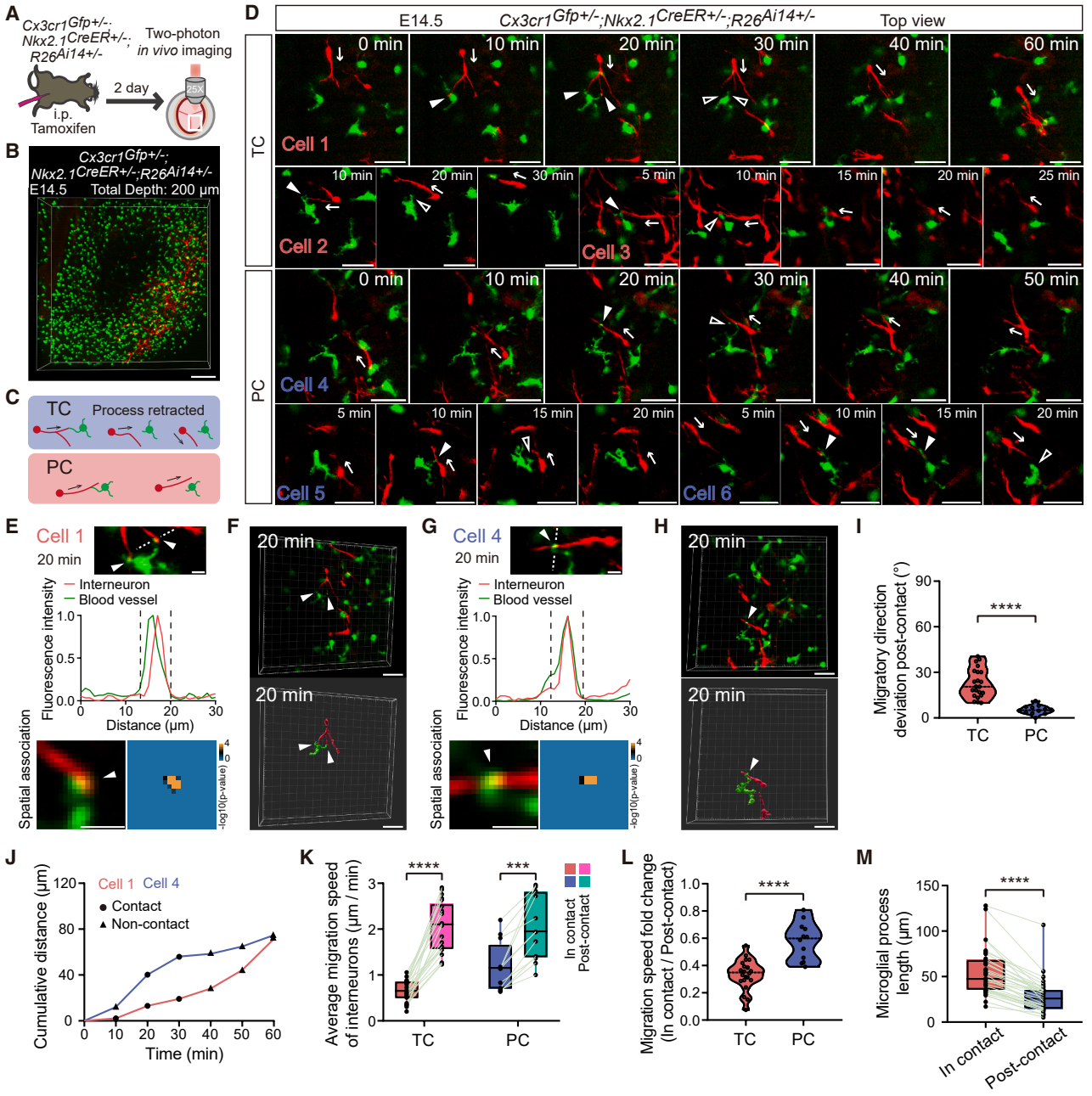

Figure 5. Intravital imaging of interactions between interneurons and microglia in the developing mouse cortex

(A) Endogenous labeling of microglia and MGE-derived interneurons, and two-photon *in vivo* imaging.

(B) The top view *in vivo* image stack of microglia and MGE-derived cortical interneurons at E14.5 (z = 200 μm). Scale bar, 200 μm.

(C) Schematic of interneuron-microglia contact modes: TC and PC.

(D) Representative *in vivo* time-lapse sequences showing interneuron-microglia interactions at E14.5. Arrows, migratory direction; solid arrowheads, microglial process-interneuron contacts; and hollow arrowheads, microglial process retraction post-contact. Scale bars, 50 μm.

(E and G) Magnified images (rectangles) showing TC (E) and PC (G) of interneurons (shown in Figure 5D) with microglial process terminals. Arrowheads, interneuron-microglia contacts; distribution plots, fluorescence intensity along dotted lines of magnified images; and heatmaps, spatial associations between red and green fluorescent signals. Scale bars, 10 μm.

(F and H) The top view *in vivo* image stack (z = 50 μm) showing interneuron-microglia contacts (arrowheads) in three-dimensional space (left) and its surface rendering (right). Scale bars, 50 μm.

(legend continued on next page)

with microglial process terminals through interneurons' leading process terminals, while others established PC with microglial process terminals in the developing mouse cortex (Figures 5C and 5D; Video S5). The overlap between fluorescence intensity distributions and significant spatial associations indicated direct contact between interneurons and microglia (Figures 5E and 5G; STAR Methods), as confirmed by three-dimensional reconstruction (Figures 5F and 5H). Analysis of interneuron migration trajectories revealed that interneuron TC with microglia induced their leading process retraction and subsequent migration redirection along pre-existing branches, whereas interneurons maintained original migratory paths without significant deviation following their PC with microglia (Figures 5D, 5I, and 5J; Video S5). In addition, interneurons exhibited a significant decrease in migration speed during microglial contact (Figure 5K), with TC causing more pronounced deceleration compared with PC (Figure 5L). Notably, we also found that microglia retracted their processes following the contact with migrating interneurons (Figures 5D and 5M; Video S5).

To elucidate molecular mechanisms underlying the contact-mediated modulation of interneuron migration, we focused on the interneuron TC with vasculature or microglia, which may involve repulsive guidance cues during these interactions. We first analyzed a published single-cell RNA sequencing (scRNA-seq) dataset of E14.5 mouse brains, containing neuronal, mural, endothelial, and microglial cells[87] (Figures S5A and S5B). After inferring the cell-cell communication network, we characterized the receptor-ligand pairing patterns of major membrane-bound chemorepulsive molecules, including the members of signaling families Eph-ephrin and Plexin (Plxn)-Semaphorin (Sema) (Figure S5C). These results showed strong receptor-ligand interactions of Plxnb-Sema4[88] in neuro-immune communication as well as Eph-ephrin[89] and Plxna-Sema6[90] in neurovascular communication (Figure S5C). We subsequently analyzed published bulk RNA sequencing (RNA-seq) datasets of embryonic mouse brains (E13.5–E15.5)[85,91,92] encompassing interneurons, microglia, and endothelial cells to systematically characterize the differential expression patterns of Eph-ephrin and Plxn-Sema signaling families across these cell populations (Figure S5D). We found that Eph members were predominantly enriched in interneurons, whereas ephrins showed complementary enrichment in endothelial cells (Figure S5D). Besides, most Plxns and Semas showed preferential enrichment in interneurons, with a limited subset enriched in endothelial cells or microglia (Figure S5D). We further profiled the top ten highly expressed membrane-bound members of the Eph-ephrin and Plxn-Sema signaling families for each cell population (Figure S5E). Given the predominant expression of EphA4 (which binds to both ephrinAs and ephrinBs)[93,94] in interneurons and the complementary high expression of ephrinBs (Efhb1-Efhb3) in endothelial cells (Figure S5E), we performed pharmacological blockade using a specific EphA4 antagonistic peptide, the KYL peptide (KYLPYWPVLSSL),[95] followed by IMEE (Figure S5F). We found that during interneuron TC1 with blood vessels, EphA4 blockade disrupted the retraction of interneuron leading process branches, instead resulting in interneurons wrapping around the vasculature (Figures S5G–S5I). The *in vivo* evidence demonstrates that EphA4 acts as a critical participant in the retraction of leading process branches during neurovascular interaction.

Taken together, here we report *in vivo* observations of interactions between migrating interneurons and blood vessels or microglia in the developing mouse cortex. Our findings demonstrate that migrating interneurons undergo contact-mediated modulation during their interactions with vasculature or microglia, revealing an adaptation strategy employed by migrating neurons to navigate complex extracellular environments.

Embryonic resting microglia survey the local environment through different manners of cellular processes' motions

We observed that microglial processes actively retracted upon contact with migrating interneurons, indicating their capacity for dynamic environmental sensing and response (Figures 5D and 5M). The resting microglia have highly motile processes by which they exert surveillance functions not only on neuronal cells[30,33,42,96–99] but also on blood vessels.[34,36,100–102] Based on the positions of their somata in the brain parenchyma, microglia were further divided into parenchymal microglia (PCMs) and capillary-associated microglia (CAMs), whose somata located on the blood vessels[34] (Figures S6A and S6B). PCMs and CAMs were similar in number, each accounting for nearly 50% of the total number of microglia at E14.5 (Figure S6C).

To investigate the dynamic motions of PCMs as well as CAMs, we labeled brain vasculature of *Cx3cr1*$^{GFP+/-}$ embryos by IU-ROI 2 h before IMEE at E14.5 (Figure 6A). The large-field image stacks were then acquired at 10-min intervals (Figure 6B). We found that while some microglia migrated along their leading processes, almost all the ramified microglia, considered to be in a resting state, actively scanned their extracellular environment with the constant motions of their fine cellular processes (Figure 6C; Video S6). By three-dimensional reconstruction and surface rendering, we confirmed that CAMs resided on the vasculature, brandishing their processes around blood vessels (Figures 6D and 6E). We found that CAM and PCM processes showed comparable lengths, but PCMs exhibited significantly higher process motility (Figures S6D and S6E). Besides, primary branch number and branching dynamics were similar between PCMs and CAMs (Figures S6F and S6G).

To further delineate the dynamic scanning behaviors of microglial processes over time, we extracted the morphological profiles of PCMs and CAMs from images captured *in vivo* every 10 min

(I, K, and L) Quantification of the migratory direction deviation (I), average migration speed (K), and migration speed fold change (L) of each migrating interneuron in contact with a microglial cell versus post-contact (TC, $n = 22$ cells; PC, $n = 12$ cells; 4 embryos from 4 dams).
(J) Quantification of cumulative distances of cell 1 and cell 2 (shown in Figure 5D).
(M) Quantification of the microglial process length in contact with interneurons versus post-contact ($n = 34$ cells per group; 4 embryos from 4 dams).
Data: violin plots (I and L) and boxplots (K and M). Statistics: conditional permutation test (10,000 iterations, E and G), Mann-Whitney U test (I and L), and Wilcoxon signed-rank test (K and M); $^{****}p < 0.0001$, $^{***}p < 0.001$.
See also Figure S5 and Video S5.

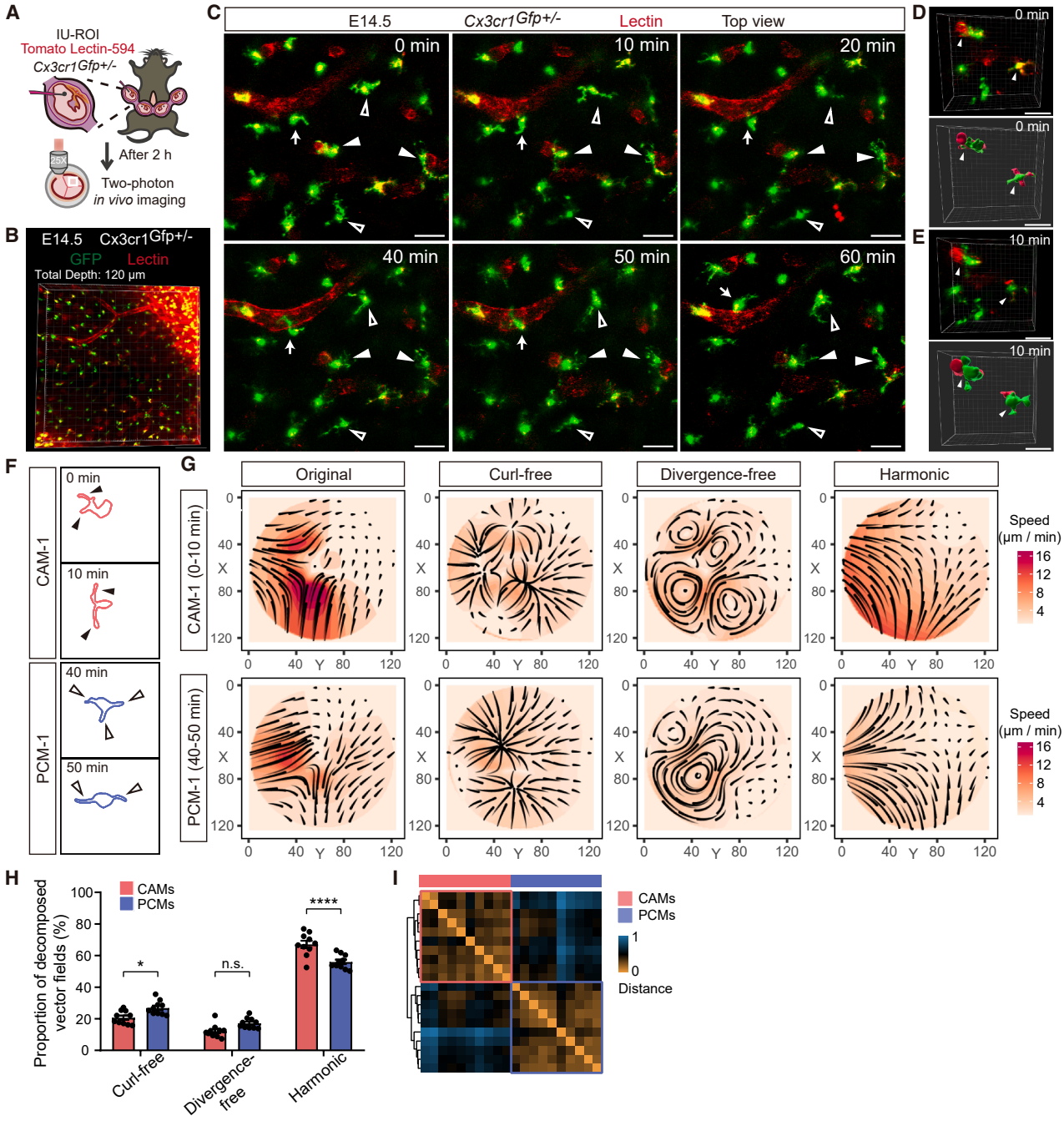

Figure 6. Intravital imaging of dynamic scanning behaviors of PCMs and CAMs in the developing mouse cortex

(A) IU-ROI labeling of blood vessels, endogenous labeling of microglia, and two-photon *in vivo* imaging.

(B) The top view *in vivo* image stack of microglia and blood vessels at E14.5 (z = 120 μm). Scale bar, 200 μm.

(C) The representative *in vivo* time-lapse sequence showing PCMs (hollow arrowheads) and CAMs (solid arrowheads) scanning behaviors. Arrows, migrating microglia. Scale bars, 50 μm.

(D and E) The top view *in vivo* image stacks (z = 60 μm) showing microglia-vasculature contacts (arrowheads) in three-dimensional space (left) and its surface rendering (right). Scale bars, 50 μm.

(F) Representative morphological profiles of CAMs and PCMs at two adjacent time points.

(G) The original vector fields constructed by microglial motions at two adjacent time points and their decomposed components.

(legend continued on next page)

during a 60-min time window (Figure S6H). We then constructed the original vector fields based on the morphological profiles of each microglial cell at two adjacent time points by the optical flow method[103] (Figures 6F, 6G, and S6I–S6K; STAR Methods). Through TVF analysis of each microglial cell (Figure S6I), we found that the curl-free vector fields showed increased contribution in PCMs compared with CAMs, confirming that PCM processes had more retracting and extending motions, while the divergence-free vector fields, representing brandishing motions of processes, showed no significant difference between the two microglial types (Figure 6H). According to the contribution of the curl-free vector fields to the original vector fields, we found a clear correspondence within the same microglial types (Figure 6I).

Altogether, here we report *in vivo* observations of the interactions between blood vessels and microglia in the embryonic mouse brains. We reveal that embryonic resting microglia exert different manners of cellular processes' motions when surveying the parenchyma versus blood vessels, suggesting that embryonic resting microglia engage in adaptive cellular behaviors in response to different extracellular environments.

Embryonic resting microglia are activated and recruited in response to environmental stress

The resting microglia continuously survey the brain and rapidly activate in response to environmental stress.[38,41,97,104,105] However, how they respond to environmental stress during embryonic development remains elusive. Consistent with a prior report of microglia accumulating at morphogenetic lesion boundaries,[106] we found P2Y12$^+$ microglia accumulation at the cortico-striato-amygdalar (CSA) boundary of E14.5 mouse embryos, without local microglia proliferation (Figures S7A and S7B). The accumulated microglia at the CSA were embedded deep into the ventral end of subcortical region, posing a natural challenge to clearly visualize them through intravital imaging methods. Thus, we induced *in utero* lesions (IULs) in the cortex to mimic physiological morphogenetic injuries.[106] We found minimal colocalization of CX3CR1$^+$ cells with either KI67 or EdU signals at the lesion site (Figures S7C and S7D), demonstrating that CX3CR1$^+$ cell accumulation primarily occurred through cellular recruitment rather than local proliferation. In addition, immunostaining showed that recruited CX3CR1$^+$ cells consist predominantly of P2Y12$^+$ microglia (94% ± 3%), with a minor population of CD206$^+$ border-associated macrophages (BAMs)[85] (Figures S7E and S7F).

To observe the recruitment of embryonic microglia *in vivo*, we performed cortical IULs in *Cx3cr1*$^{GFP+/-}$ embryos 30 min before IMEE at E14.5 and acquired image stacks of the lesion site at 5-min intervals (Figures 7A and 7B). Microglia, as far as 350 μm away from the lesion site, were soon recruited, traveling at an average speed of 2.3 ± 0.7 μm per min (Figures 7C, 7D, 7F, and 7G; Video S7). The speed at which each microglial cell traveled varied over time, with a maximum speed of 10.8 μm per min (Figure 7H). We found that microglia exhibited a canonical migratory morphology with specialized leading processes guiding their migration to the lesion site (Figure 7E; Video S7). Interestingly, we also noticed that upon arrival at the lesion site, microglial processes retracted and became more dormant (Figure 7E; Video S7), displaying significant reduction in length as well as motility (Figures 7I and 7J). These results indicated microglial cells' transition to the activated state at the lesion site. Besides, we observed intense and punctuated fluorescent signals of fibronectin 1 (FN1) within microglia at the lesion site (Figure S7G), suggesting the engulfment and tissue repair roles of these recruited microglia under environmental stress.[106,107] Using three-dimensional reconstruction and immunostaining of the post-IMEE brain, we acquired the location of microglia accumulation in the entire embryonic brain, and we further confirmed that the recruited cells at the lesion site were predominantly P2Y12$^+$ microglia (Figures 7K and 7L). Together, these results suggest that embryonic microglia rapidly transit from a resting state to directed migration in response to environmental stress, adopting an activated state at lesion sites to promote tissue protection and homeostatic restoration.

The communication between the nervous and immune systems plays a critical role in tissue homeostasis.[108–112] During a stressful event in the nervous system, a rapid immune activation occurs not only in resident microglia but also in other blood-borne immune cells.[35,39,113–115] To investigate how the immune system responded to the environmental stress inside the CNS, we performed IU-ROI and brain IULs in *Cx3cr1*$^{GFP+/-}$ embryos 10 min before IMEE (Figure S7H). Immediately after brain lesions at E12.5 or E14.5, we found a large number of CX3CR1$^+$ cells traveling inside the cerebral venous sinuses, which was absent in brains without lesions (Figure S7I; Video S8). Moreover, these flowing CX3CR1$^+$ cells—identified as CSF1R$^+$ circulating monocytes[116]—maintained consistent diameters at E12.5 and E14.5 (Figures S7J and S7K), indicating that CNS stress triggers rapid circulation of monocytes through the cerebral vasculature. Another possible way by which immune cells can be carried to the CNS is through the cerebrospinal fluid.[117–119] We observed that CX3CR1$^+$ cells gathered and accumulated en masse in the fourth ventricle after brain lesions at E11.5 (Figure S7L), a phenomenon absent in non-lesioned controls (Figure S7M). Subsequent immunostaining revealed that these rapidly accumulating CX3CR1$^+$ cells were CD206$^+$ BAMs (Figure S7M).

Altogether, here we report *in vivo* observations of cellular dynamics of microglia and circulating immune cells in response to cortical lesions. These results reveal that microglia can be activated and recruited into lesion sites while other immune cells can travel through the CNS via the circulatory systems, indicating the neuro-immune communication in response to the environmental stress during the embryogenesis.

DISCUSSION

During development, both immature, developing cells and mature, functional cells coexist and respond to the changing extracellular

(H) Contribution of decomposed components to original vector fields (CAMs, n = 10 cells; PCMs, n = 10 cells; 2 embryos from 2 dams).
(I) Heatmap illustrating the distance of the averaged decomposed curl-free vector fields of CAMs and PCMs.
Data: mean ± SEM (H). Statistics:two-way ANOVA followed by Bonferroni's multiple comparisons (H); ****$p < 0.0001$, *$p < 0.05$, n.s., nonsignificant ($p > 0.05$).
See also Figure S6 and Video S6.

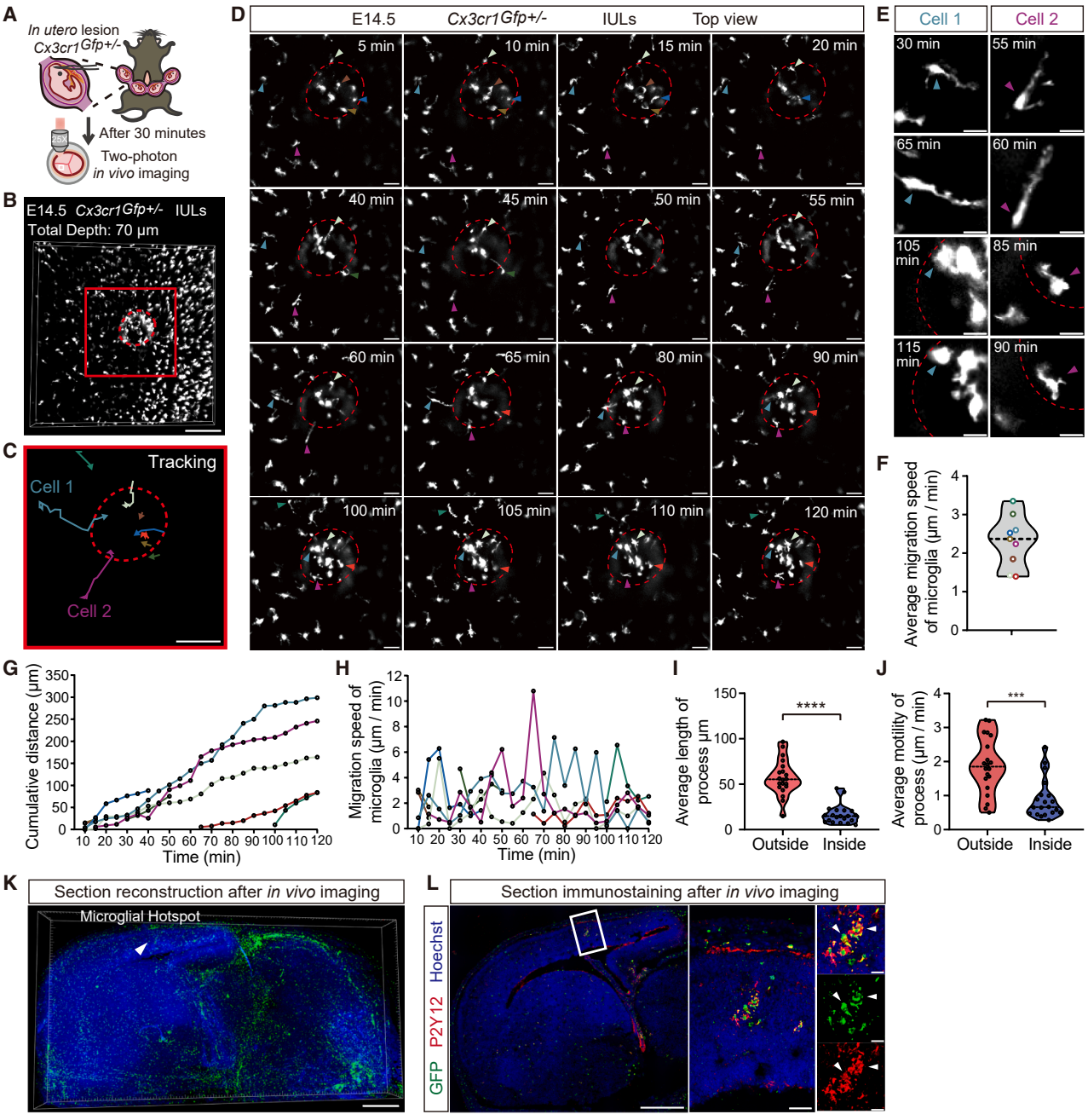

Figure 7. Intravital imaging of the recruitment and activation of microglia in the developing mouse cortex

(A) *In utero* lesions (IULs), endogenous labeling of microglia, and two-photon *in vivo* imaging.

(B) The top view *in vivo* image stack of microglial hotspots at the lesion site at E14.5 (z = 70 µm). Marked regions are also shown in Figures 7C and 7D. Scale bar, 200 µm.

(C) Microglial recruitment trajectories to lesion site. Scale bar, 50 µm.

(D) The *in vivo* time-lapse sequence showing microglia (arrowheads; color coded as in Figure 7C) migrating to the lesion site after IULs. Scale bars, 50 µm.

(E) The representative *in vivo* time-lapse sequences showing recruited microglia (arrowheads) outside and inside the lesion site. Scale bars, 20 µm.

(F–H) Quantification of the accumulative distance (F), average migration speed (G), and migration speed (H) of nine cells indicated by corresponding colored arrowheads in Figures 7C and 7D.

(I and J) Quantification of the average process length (I) and motility (J) of recruited microglia outside versus inside the lesion site (outside, *n* = 20 cells; inside, *n* = 20 cells; 3 embryos from 3 dams).

(legend continued on next page)

environments.[120,121] Considering the significant disruptions of physiological conditions in *ex vivo* approaches[44–52] and limitations of existing intravital imaging methods, we establish the IMEE method that comes with stable immobilization, flexible viewing angles, a simple procedure, and broad applications, allowing for long-term, large-field, and deep-depth intravital imaging of mouse embryos (Figures 1, S1, and S2). In addition, the inherent versatility of IMEE enables its application across diverse experimental paradigms through compatibility with various labeling methods and genetic manipulations (Figure 2), including transgenic mouse lines, IUE, *in utero* injection of chemical reagents or virus, and tissue transplantation. Furthermore, studies using IMEE can be conducted in the context of a range of developmental defects and diseases within and outside the CNS (Figure S4), providing crucial translational knowledge for human pathologies. Moreover, the maneuverability of the IMEE device will empower developmental studies across multiple organs and species, extending its utility beyond rodent neurodevelopment.

Prior *ex vivo* imaging of acute mouse brain slices reveals "random walk" migration of MZ interneurons,[21] consistent with our *in vivo* observations by IMEE (Figures 3 and S3). Beyond this, we also simultaneously characterized the unidirectional migration of SVZ interneurons *in vivo*. Moreover, quantitative analysis reveals comparable tangential migration speeds between MZ and SVZ interneurons, and TVF analysis demonstrates that heterogeneous swarm movements of MZ interneurons result from the spiral rather than radiating or concentrating movements. Although some studies suggest that cortical interneurons display a preference for migratory routes by expressing receptors that correspond to the route-specific guidance cues,[23,74,77,122,123] e.g., SST^+ Martinotti cells migrate through the MZ while SST^+ non-Martinotti cells disperse via the SVZ,[23] future studies are still needed to combine the IMEE method with spatial transcriptomics, thereby systematically revealing the migratory behaviors of different neuronal subtypes in the developing mouse brain. In addition, interneurons may have an internal clock that paces their maturation,[124,125] which would initiate the transition from tangential to radial migration when cells autonomously switch off their responsiveness to specific attractants.[126,127] In our data, we also noticed that some interneurons exited from the migratory streams, prompting further *in vivo* investigation into the tangential-to-radial switch and the subsequent allocation to specific cortical layers.

The vascular network and the immune system serve as important components of the extracellular environment in the developing cortex.[12,85,98,128–131] We used IMEE to successfully characterize the distinct interaction modes among migrating interneurons, microglia, and vasculature in mouse embryos *in vivo* (Figures 4, 5, and S5). Although previous *ex vivo* studies showed that migrating interneurons are guided by oligodendrocyte precursors through contact repulsion,[29] our findings demonstrate that interneurons employ contact-mediated modulation during their interactions with vasculature or microglia *in vivo*. In contrast to the complete reversal of migratory directions during interactions with oligodendrocyte precursors,[29] interneurons avoid blood vessels by either selecting alternative leading process branches or generating new ones, resulting in migration deceleration and directional deviation rather than directional reversal (Figure 4). Notably, previous *ex vivo* studies demonstrated that cortical interneurons exhibit biased selection of leading process branches during tangential migration,[15] a phenomenon that we also observed *in vivo* (Figure S4). Beyond this, our findings further reveal that direct cell-cell contact with either vasculature or microglia mediates interneurons' biased selection of leading process branches. Our *in vivo* evidence reinforces the notion that contact-mediated modulation acts as a fundamental strategy for migrating cells to navigate through the complex local environments.

Microglia are the resident macrophages in the CNS parenchyma, which are different from BAMs residing in the meninges, choroid plexus, and perivascular spaces.[85,86] Due to aforementioned methodological challenges of previous methods, we use the IMEE method to observe the dynamics of embryonic microglial motions *in vivo* (Figures 6 and 7). Our results suggest that PCMs, one of two types of microglia, exhibit more extensions and retractions of cellular processes than CAMs in the mouse developing cortex, exemplifying yet another case of environmentally adaptive cellular behaviors (Figures 6 and S6). Importantly, our characterization of microglial surveillance behaviors in the developing cortex enhances our understanding of the "physiological" performance of embryonic resting microglia *in vivo*, which has been previously overlooked. These surveillance behaviors of resting microglia serve the purpose of integrating and interpreting the environmental cues, enabling them to be constantly ready to transform to the activated states.[38,40,41,97] A recent study demonstrated that microglia maintained the structural integrity of embryonic mouse brains by accumulating at the boundaries between brain regions under morphogenetic stress.[106] Our study further elucidates the dynamic recruitment and activation of embryonic microglia under environmental stress *in vivo* (Figure 7). In addition, we also notice that other immune cells, in response to the environmental stress, rapidly travel to the CNS through the vascular as well as cerebrospinal fluid circulatory systems, providing a critical perspective on our understanding of the trinity of neuro-vascular-immune communication during embryogenesis (Figure S7).

On one hand, our IMEE method offers opportunities for studies on diverse cellular dynamic behaviors during embryogenesis in the context of physiological development or developmental defects and diseases. On the other hand, our biological findings advance our understanding of the environmentally adaptive cellular behaviors in the developing mammalian brain and open avenues for exploring the neuro-vascular-immune communication in mammalian embryos.

(K) 3D reconstruction of the brain after *in vivo* imaging. Arrowhead indicates the microglial hotspot observed in Figures 7B and 7D. Scale bar, 500 μm.
(L) Sagittal sections of the brain (shown in Figure 7K) were stained for GFP (green), P2Y12 (red), and Hoechst (blue). Arrowheads, GFP^+P2Y12^+ microglia. Scale bars, 500 μm (left), 50 μm (middle), and 20 μm (right).
Data: violin plots (G, I, and J). Statistics: Mann-Whitney U test; $^{****}p < 0.0001$, $^{***}p < 0.001$.
See also Figure S7 and Video S7.

Limitations of the study

While IMEE sustains embryonic blood supply for hours, prolonged imaging may be achieved by designing biocompatible immobilization materials that minimize mechanical stress on the vasculature. In addition, whereas multi-viewing angles of IMEE coupled with two-photon microscopy allow the *in vivo* observation of cellular dynamics, clear observations cannot be achieved in tissues deeply embedded in the embryos, such as the germinal zones of the subpallium. Future studies on these deeper regions of embryos can combine our IMEE with multi-photon microscopies or live-tissue clearing.[132] Finally, for the large-field images, here we only showcased those obtained by stitching, which unavoidably decreased the temporal resolution. This might be addressed by applying mesoscale imaging methods[133] compatible with our IMEE device to achieve large-scale imaging without compromising the temporal resolution.

RESOURCE AVAILABILITY

Lead contact

Further requests and information concerning this study should be addressed to the lead contact, Da Mi (mida@tsinghua.edu.cn).

Materials availability

All the reagents are available on request to the lead contact.

Data and code availability

The codes generated during this study with example data are available at GitHub with the following link: https://github.com/MiLabTsinghua/IMEE. The published article includes all data generated during this study, and all the raw data are also available from the corresponding author upon request. Any additional information required to reanalyze the data reported in this paper is available from the lead contact upon request.

ACKNOWLEDGMENTS

We thank Drs. Oscar Marín, Songhai Shi, Xin Liang, and Jiamin Wu for discussions and valuable suggestions. We thank Dr. Qionghai Dai for sharing the *CX3CR1*^{GFP} mice and Yuwei Peng for providing technical assistance. This work was supported by grants from the Ministry of Science and Technology of China and the National Natural Science Foundation of China (STI2030-Major Projects [2021ZD0202300] to D.M., 32525032 to Z.V.G., 2024YFA1802600 to D.M., 32271024 to D.M., STI2030-Major Projects [2021ZD0203600] to Z.V.G., and 32170998 to Z.V.G.), the Natural Science Foundation of Beijing Municipality (Z240011) to Z.V.G., the Tsinghua-Peking Joint Center for Life Sciences start-up grant to D.M., the Tsinghua University Dushi Program to D.M., and the support from THU-IDG/McGovern Open Laboratory of Shared Instruments for Brain Science.

AUTHOR CONTRIBUTIONS

Conceptualization: Z. Long, Y. Yu, Z.V.G., and D.M.; methodology: Z. Long and Y. Yu; biological experiments: Z. Long, C.H., Y. Yu, and Z. Li; investigation: Z. Long, Y. Yu, and C.H.; visualization: Z. Long, Y. Yu, and Y. Yan; data curation: Z. Long, Y. Yu, C.H., and Y. Yan; writing – original draft: Z. Long, Y. Yu, L.X., Z.V.G., and D.M.; funding acquisition: Z.V.G. and D.M.; project administration: Z.V.G. and D.M.; supervision: Z.V.G. and D.M.

DECLARATION OF INTERESTS

Z. Long, Y. Yu, Z.V.G., and D.M. have pending patent applications related to the IMEE method described in this work.

STAR★METHODS

Detailed methods are provided in the online version of this paper and include the following:

- KEY RESOURCES TABLE
- EXPERIMENTAL MODEL AND STUDY PARTICIPANT DETAILS
- METHOD DETAILS
  - IMEE device
  - IMEE experiments
- ENDOGENOUS TRANSGENIC LABELING
- VPA-INDUCED MOUSE MODEL
- *IN UTERO* RETRO-ORBITAL INJECTION
- *IN UTERO* ELECTROPORATION
- *IN UTERO* LESIONS
- IMMUNOHISTOCHEMISTRY
  - EdU labeling and detection
  - H&E staining
- CARDIOVASCULAR BLOOD TEST
- CELL VIABILITY MEASUREMENT
- REAL-TIME PCR
- SECTION RECONSTRUCTION AND ALIGNMENT
- MOTION CORRECTION OF TIME-LAPSE IMAGE STACKS
- MODELING OF CELLULAR MOVEMENT TRAJECTORIES
- INDIVIDUAL CELL TRACKING
- TRANSCRIPTOMIC ANALYSIS
  - Single-cell RNA-seq data analysis
  - Bulk RNA-seq data analysis
- QUANTIFICATION AND STATISTICAL ANALYSIS
  - Statistical analysis
  - Topological analysis of vector fields
  - Fluorescence intensity analysis
  - Spatial association analysis
  - Cell density

SUPPLEMENTAL INFORMATION

Supplemental information can be found online at https://doi.org/10.1016/j.cell.2025.11.017.

Received: December 11, 2024
Revised: July 11, 2025
Accepted: November 11, 2025
Published: December 16, 2025

REFERENCES

1. Rakic, P. (2009). Evolution of the neocortex: a perspective from developmental biology. Nat. Rev. Neurosci. *10*, 724–735. https://doi.org/10.1038/nrn2719.
2. Tasic, B., Yao, Z., Graybuck, L.T., Smith, K.A., Nguyen, T.N., Bertagnolli, D., Goldy, J., Garren, E., Economo, M.N., Viswanathan, S., et al. (2018). Shared and distinct transcriptomic cell types across neocortical areas. Nature *563*, 72–78. https://doi.org/10.1038/s41586-018-0654-5.
3. Zeisel, A., Hochgerner, H., Lönnerberg, P., Johnsson, A., Memic, F., van der Zwan, J., Häring, M., Braun, E., Borm, L.E., La Manno, G., et al. (2018). Molecular Architecture of the Mouse Nervous System. Cell *174*, 999–1014.e22. https://doi.org/10.1016/j.cell.2018.06.021.
4. Yao, Z., van Velthoven, C.T.J., Nguyen, T.N., Goldy, J., Sedeno-Cortes, A.E., Baftizadeh, F., Bertagnolli, D., Casper, T., Chiang, M., Crichton, K., et al. (2021). A taxonomy of transcriptomic cell types across the isocortex and hippocampal formation. Cell *184*, 3222–3241.e26. https://doi.org/10.1016/j.cell.2021.04.021.
5. Molnár, Z., Clowry, G.J., Šestan, N., Alzu'bi, A., Bakken, T., Hevner, R.F., Hüppi, P.S., Kostović, I., Rakic, P., Anton, E.S., et al. (2019). New insights into the development of the human cerebral cortex. J. Anat. *235*, 432–451. https://doi.org/10.1111/joa.13055.

6. Luria, V., Ma, S., Shibata, M., Pattabiraman, K., and Sestan, N. (2023). Molecular and cellular mechanisms of human cortical connectivity. Curr. Opin. Neurobiol. *80*, 102699. https://doi.org/10.1016/j.conb.2023.102699.

7. Kriegstein, A., and Alvarez-Buylla, A. (2009). The glial nature of embryonic and adult neural stem cells. Annu. Rev. Neurosci. *32*, 149–184. https://doi.org/10.1146/annurev.neuro.051508.135600.

8. Florio, M., and Huttner, W.B. (2014). Neural progenitors, neurogenesis and the evolution of the neocortex. Development *141*, 2182–2194. https://doi.org/10.1242/dev.090571.

9. Kierdorf, K., Erny, D., Goldmann, T., Sander, V., Schulz, C., Perdiguero, E.G., Wieghofer, P., Heinrich, A., Riemke, P., Hölscher, C., et al. (2013). Microglia emerge from erythromyeloid precursors via Pu.1- and Irf8-dependent pathways. Nat. Neurosci. *16*, 273–280. https://doi.org/10.1038/nn.3318.

10. Gomez Perdiguero, E., Klapproth, K., Schulz, C., Busch, K., Azzoni, E., Crozet, L., Garner, H., Trouillet, C., de Bruijn, M.F., Geissmann, F., et al. (2014). Tissue-resident macrophages originate from yolk-sac-derived erythro-myeloid progenitors. Nature *518*, 547–551. https://doi.org/10.1038/nature13989.

11. Silva, C.G., Peyre, E., and Nguyen, L. (2019). Cell migration promotes dynamic cellular interactions to control cerebral cortex morphogenesis. Nat. Rev. Neurosci. *20*, 318–329. https://doi.org/10.1038/s41583-019-0148-y.

12. Nayak, D., Roth, T.L., and McGavern, D.B. (2014). Microglia Development and Function. Annu. Rev. Immunol. *32*, 367–402. https://doi.org/10.1146/annurev-immunol-032713-120240.

13. Hattori, Y. (2023). The multifaceted roles of embryonic microglia in the developing brain. Front. Cell. Neurosci. *17*, 988952. https://doi.org/10.3389/fncel.2023.988952.

14. Marín, O., Valiente, M., Ge, X., and Tsai, L.H. (2010). Guiding Neuronal Cell Migrations. Cold Spring Harb. Perspect. Biol. *2*, a001834. https://doi.org/10.1101/cshperspect.a001834.

15. Martini, F.J., Valiente, M., López Bendito, G., Szabó, G.B., Moya, F., Valdeolmillos, M., and Marín, O. (2009). Biased selection of leading process branches mediates chemotaxis during tangential neuronal migration. Development *136*, 41–50. https://doi.org/10.1242/dev.025502.

16. Kettenmann, H., Hanisch, U.K., Noda, M., and Verkhratsky, A. (2011). Physiology of microglia. Physiol. Rev. *91*, 461–553. https://doi.org/10.1152/physrev.00011.2010.

17. Nadarajah, B., Brunstrom, J.E., Grutzendler, J., Wong, R.O., and Pearlman, A.L. (2001). Two modes of radial migration in early development of the cerebral cortex. Nat. Neurosci. *4*, 143–150. https://doi.org/10.1038/83967.

18. Nadarajah, B., Alifragis, P., Wong, R.O., and Parnavelas, J.G. (2003). Neuronal migration in the developing cerebral cortex: observations based on real-time imaging. Cereb. Cortex *13*, 607–611. https://doi.org/10.1093/cercor/13.6.607.

19. Tabata, H., and Nakajima, K. (2003). Multipolar migration: the third mode of radial neuronal migration in the developing cerebral cortex. J. Neurosci. *23*, 9996–10001. https://doi.org/10.1523/JNEUROSCI.23-31-09996.2003.

20. Kon, E., Cossard, A., and Jossin, Y. (2017). Neuronal Polarity in the Embryonic Mammalian Cerebral Cortex. Front. Cell. Neurosci. *11*, 163. https://doi.org/10.3389/fncel.2017.00163.

21. Tanaka, D.H., Yanagida, M., Zhu, Y., Mikami, S., Nagasawa, T., Miyazaki, J.-I., Yanagawa, Y., Obata, K., and Murakami, F. (2009). Random Walk Behavior of Migrating Cortical Interneurons in the Marginal Zone: Time-Lapse Analysis in Flat-Mount Cortex. J. Neurosci. *29*, 1300–1311. https://doi.org/10.1523/jneurosci.5446-08.2009.

22. Marín, O., and Rubenstein, J.L. (2001). A long, remarkable journey: tangential migration in the telencephalon. Nat. Rev. Neurosci. *2*, 780–790. https://doi.org/10.1038/35097509.

23. Lim, L., Pakan, J.M.P., Selten, M.M., Marques-Smith, A., Llorca, A., Bae, S.E., Rochefort, N.L., and Marín, O. (2018). Optimization of interneuron function by direct coupling of cell migration and axonal targeting. Nat. Neurosci. *21*, 920–931. https://doi.org/10.1038/s41593-018-0162-9.

24. Tiveron, M.-C., Rossel, M., Moepps, B., Zhang, Y.L., Seidenfaden, R., Favor, J., König, N., and Cremer, H. (2006). Molecular Interaction between Projection Neuron Precursors and Invading Interneurons via Stromal-Derived Factor 1 (CXCL12)/CXCR4 Signaling in the Cortical Subventricular Zone/Intermediate Zone. J. Neurosci. *26*, 13273–13278. https://doi.org/10.1523/jneurosci.4162-06.2006.

25. Yokota, Y., Gashghaei, H.T., Han, C., Watson, H., Campbell, K.J., and Anton, E.S. (2007). Radial Glial Dependent and Independent Dynamics of Interneuronal Migration in the Developing Cerebral Cortex. PLOS One *2*, e794. https://doi.org/10.1371/journal.pone.0000794.

26. Won, C., Lin, Z., Kumar T, P., Li, S., Ding, L., Elkhal, A., Szabó, G., and Vasudevan, A. (2013). Autonomous vascular networks synchronize GABA neuron migration in the embryonic forebrain. Nat. Commun. *4*, 2149. https://doi.org/10.1038/ncomms3149.

27. Andreone, B.J., Lacoste, B., and Gu, C. (2015). Neuronal and Vascular Interactions. Annu. Rev. Neurosci. *38*, 25–46. https://doi.org/10.1146/annurev-neuro-071714-033835.

28. Barber, M., Andrews, W.D., Memi, F., Gardener, P., Ciantar, D., Tata, M., Ruhrberg, C., and Parnavelas, J.G. (2018). Vascular-Derived Vegfa Promotes Cortical Interneuron Migration and Proximity to the Vasculature in the Developing Forebrain. Cereb. Cortex *28*, 2577–2593. https://doi.org/10.1093/cercor/bhy082.

29. Lepiemme, F., Stoufflet, J., Javier-Torrent, M., Mazzucchelli, G., Silva, C.G., and Nguyen, L. (2022). Oligodendrocyte precursors guide interneuron migration by unidirectional contact repulsion. Science *376*, eabn6204. https://doi.org/10.1126/science.abn6204.

30. Nimmerjahn, A., Kirchhoff, F., and Helmchen, F. (2005). Resting microglial cells are highly dynamic surveillants of brain parenchyma in vivo. Science *308*, 1314–1318. https://doi.org/10.1126/science.1110647.

31. Paolicelli, R.C., Bolasco, G., Pagani, F., Maggi, L., Scianni, M., Panzanelli, P., Giustetto, M., Ferreira, T.A., Guiducci, E., Dumas, L., et al. (2011). Synaptic pruning by microglia is necessary for normal brain development. Science *333*, 1456–1458. https://doi.org/10.1126/science.1202529.

32. Matcovitch-Natan, O., Winter, D.R., Giladi, A., Vargas Aguilar, S., Spinrad, A., Sarrazin, S., Ben-Yehuda, H., David, E., Zelada González, F., Perrin, P., et al. (2016). Microglia development follows a stepwise program to regulate brain homeostasis. Science *353*, aad8670. https://doi.org/10.1126/science.aad8670.

33. Rotterman, T.M., and Alvarez, F.J. (2020). Microglia Dynamics and Interactions with Motoneurons Axotomized After Nerve Injuries Revealed By Two-Photon Imaging. Sci. Rep. *10*, 8648. https://doi.org/10.1038/s41598-020-65363-9.

34. Bisht, K., Okojie, K.A., Sharma, K., Lentferink, D.H., Sun, Y.-Y., Chen, H.-R., Uweru, J.O., Amancherla, S., Calcuttawala, Z., Campos-Salazar, A.B., et al. (2021). Capillary-associated microglia regulate vascular structure and function through PANX1-P2RY12 coupling in mice. Nat. Commun. *12*, 5289. https://doi.org/10.1038/s41467-021-25590-8.

35. Goldmann, T., Wieghofer, P., Jordão, M.J.C., Prutek, F., Hagemeyer, N., Frenzel, K., Amann, L., Staszewski, O., Kierdorf, K., Krueger, M., et al. (2016). Origin, fate and dynamics of macrophages at central nervous system interfaces. Nat. Immunol. *17*, 797–805. https://doi.org/10.1038/ni.3423.

36. Mondo, E., Becker, S.C., Kautzman, A.G., Schifferer, M., Baer, C.E., Chen, J., Huang, E.J., Simons, M., and Schafer, D.P. (2020). A Developmental Analysis of Juxtavascular Microglia Dynamics and Interactions with the Vasculature. J. Neurosci. *40*, 6503–6521. https://doi.org/10.1523/jneurosci.3006-19.2020.

37. Goldmann, T., Wieghofer, P., Müller, P.F., Wolf, Y., Varol, D., Yona, S., Brendecke, S.M., Kierdorf, K., Staszewski, O., Datta, M., et al. (2013).

A new type of microglia gene targeting shows TAK1 to be pivotal in CNS autoimmune inflammation. Nat. Neurosci. *16*, 1618–1626. https://doi.org/10.1038/nn.3531.

38. Donat, C.K., Scott, G., Gentleman, S.M., and Sastre, M. (2017). Microglial Activation in Traumatic Brain Injury. Front. Aging Neurosci. *9*, 208. https://doi.org/10.3389/fnagi.2017.00208.

39. Kierdorf, K., Masuda, T., Jordão, M.J.C., and Prinz, M. (2019). Macrophages at CNS interfaces: ontogeny and function in health and disease. Nat. Rev. Neurosci. *20*, 547–562. https://doi.org/10.1038/s41583-019-0201-x.

40. Davalos, D., Grutzendler, J., Yang, G., Kim, J.V., Zuo, Y., Jung, S., Littman, D.R., Dustin, M.L., and Gan, W.B. (2005). ATP mediates rapid microglial response to local brain injury in vivo. Nat. Neurosci. *8*, 752–758. https://doi.org/10.1038/nn1472.

41. Witcher, K.G., Bray, C.E., Dziabis, J.E., McKim, D.B., Benner, B.N., Rowe, R.K., Kokiko-Cochran, O.N., Popovich, P.G., Lifshitz, J., Eiferman, D.S., et al. (2018). Traumatic brain injury-induced neuronal damage in the somatosensory cortex causes formation of rod-shaped microglia that promote astrogliosis and persistent neuroinflammation. Glia *66*, 2719–2736. https://doi.org/10.1002/glia.23523.

42. Kamei, R., and Okabe, S. (2023). In vivo imaging of the phagocytic dynamics underlying efficient clearance of adult-born hippocampal granule cells by ramified microglia. Glia *71*, 2005–2023. https://doi.org/10.1002/glia.24379.

43. Silvin, A., Qian, J., and Ginhoux, F. (2023). Brain macrophage development, diversity and dysregulation in health and disease. Cell. Mol. Immunol. *20*, 1277–1289. https://doi.org/10.1038/s41423-023-01053-6.

44. Wolff, J.R., Rajan, K.T., and Noack, W. (1974). The fate and fine structure of fragments of blood vessels in CNS tissue cultures. Cell Tissue Res. *156*, 89–102. https://doi.org/10.1007/BF00220103.

45. Moser, K.V., Schmidt-Kastner, R., Hinterhuber, H., and Humpel, C. (2003). Brain capillaries and cholinergic neurons persist in organotypic brain slices in the absence of blood flow. Eur. J. Neurosci. *18*, 85–94. https://doi.org/10.1046/j.1460-9568.2003.02728.x.

46. Bendfeldt, K., Radojevic, V., Kapfhammer, J., and Nitsch, C. (2007). Basic Fibroblast Growth Factor Modulates Density of Blood Vessels and Preserves Tight Junctions in Organotypic Cortical Cultures of Mice: A NewIn VitroModel of the Blood–Brain Barrier. J. Neurosci. *27*, 3260–3267. https://doi.org/10.1523/jneurosci.4033-06.2007.

47. Tran, C.H.T., and Gordon, G.R. (2015). Astrocyte and Microvascular Imaging in Awake Animals Using Two-Photon Microscopy. Microcirculation *22*, 219–227. https://doi.org/10.1111/micc.12188.

48. Humpel, C. (2015). Organotypic brain slice cultures: A review. Neuroscience *305*, 86–98. https://doi.org/10.1016/j.neuroscience.2015.07.086.

49. Hailer, N.P., Jarhult, J.D., and Nitsch, R. (1996). Resting microglial cells in vitro: Analysis of morphology and adhesion molecule expression in organotypic hippocampal slice cultures. Glia *18*, 319–331. https://doi.org/10.1002/(sici)1098-1136(199612)18:4<319::Aid-glia6>3.0.Co;2-s.

50. Czapiga, M., and Colton, C.A. (1999). Function of microglia in organotypic slice cultures. J. Neurosci. Res. *56*, 644–651. https://doi.org/10.1002/(sici)1097-4547(19990615)56:6<644::Aid-jnr10>3.0.Co;2-9.

51. Stence, N., Waite, M., and Dailey, M.E. (2001). Dynamics of microglial activation: A confocal time-lapse analysis in hippocampal slices. Glia *33*, 256–266. https://doi.org/10.1002/1098-1136(200103)33:3<256::Aid-glia1024>3.0.Co;2-j.

52. Delbridge, A.R.D., Huh, D., Brickelmaier, M., Burns, J.C., Roberts, C., Challa, R., Raymond, N., Cullen, P., Carlile, T.M., Ennis, K.A., et al. (2020). Organotypic Brain Slice Culture Microglia Exhibit Molecular Similarity to Acutely-Isolated Adult Microglia and Provide a Platform to Study Neuroinflammation. Front. Cell. Neurosci. *14*, 592005. https://doi.org/10.3389/fncel.2020.592005.

53. Huang, Q., Cohen, M.A., Alsina, F.C., Devlin, G., Garrett, A., McKey, J., Havlik, P., Rakhilin, N., Wang, E., Xiang, K., et al. (2020). Intravital imaging of mouse embryos. Science *368*, 181–186. https://doi.org/10.1126/science.aba0210.

54. Yanagida, M., Miyoshi, R., Toyokuni, R., Zhu, Y., and Murakami, F. (2012). Dynamics of the leading process, nucleus, and Golgi apparatus of migrating cortical interneurons in living mouse embryos. Proc. Natl. Acad. Sci. USA *109*, 16737–16742. https://doi.org/10.1073/pnas.1209166109.

55. Munz, M., Bharioke, A., Kosche, G., Moreno-Juan, V., Brignall, A., Rodrigues, T.M., Graff-Meyer, A., Ulmer, T., Haeuselmann, S., Pavlinic, D., et al. (2023). Pyramidal neurons form active, transient, multilayered circuits perturbed by autism-associated mutations at the inception of neocortex. Cell *186*, 1930–1949.e31. https://doi.org/10.1016/j.cell.2023.03.025.

56. Hattori, Y., Kato, D., Murayama, F., Koike, S., Asai, H., Yamasaki, A., Naito, Y., Kawaguchi, A., Konishi, H., Prinz, M., et al. (2023). CD206+ macrophages transventricularly infiltrate the early embryonic cerebral wall to differentiate into microglia. Cell Rep. *42*, 112092. https://doi.org/10.1016/j.celrep.2023.112092.

57. Kawasoe, R., Shinoda, T., Hattori, Y., Nakagawa, M., Pham, T.Q., Tanaka, Y., Sagou, K., Saito, K., Katsuki, S., Kotani, T., et al. (2020). Two-photon microscopic observation of cell-production dynamics in the developing mammalian neocortex in utero. Dev. Growth Differ. *62*, 118–128. https://doi.org/10.1111/dgd.12648.

58. Ang, E.S.B.C., Haydar, T.F., Gluncic, V., and Rakic, P. (2003). Four-dimensional migratory coordinates of GABAergic interneurons in the developing mouse cortex. J. Neurosci. *23*, 5805–5815. https://doi.org/10.1523/JNEUROSCI.23-13-05805.2003.

59. Villar-Cerviño, V., Molano-Mazón, M., Catchpole, T., Valdeolmillos, M., Henkemeyer, M., Martínez, L.M., Borrell, V., and Marín, O. (2013). Contact Repulsion Controls the Dispersion and Final Distribution of Cajal-Retzius Cells. Neuron *77*, 457–471. https://doi.org/10.1016/j.neuron.2012.11.023.

60. Yardeni, T., Eckhaus, M., Morris, H.D., Huizing, M., and Hoogstraten-Miller, S. (2011). Retro-orbital injections in mice. Lab Anim. *40*, 155–160. https://doi.org/10.1038/laban0511-155.

61. Li, S., Li, T., Luo, Y., Yu, H., Sun, Y., Zhou, H., Liang, X., Huang, J., and Tang, S. (2011). Retro-orbital injection of FITC-dextran is an effective and economical method for observing mouse retinal vessels. Mol. Vis. *17*, 3566–3573.

62. Bryson, J.L., Coles, M.C., and Manley, N.R. (2011). A Method for Labeling Vasculature in Embryonic Mice. J. Vis. Exp. *56*, 3267. https://doi.org/10.3791/3267.

63. Xiong, B., Li, A., Lou, Y., Chen, S., Long, B., Peng, J., Yang, Z., Xu, T., Yang, X., Li, X., et al. (2017). Precise Cerebral Vascular Atlas in Stereotaxic Coordinates of Whole Mouse Brain. Front. Neuroanat. *11*, 128. https://doi.org/10.3389/fnana.2017.00128.

64. Andjelkovic, A.V., Nikolic, B., Pachter, J.S., and Zecevic, N. (1998). Macrophages/microglial cells in human central nervous system during development: an immunohistochemical study. Brain Res. *814*, 13–25. https://doi.org/10.1016/S0006-8993(98)00830-0.

65. Shrirao, A.B., Schloss, R.S., Fritz, Z., Shrirao, M.V., Rosen, R., and Yarmush, M.L. (2021). Autofluorescence of blood and its application in biomedical and clinical research. Biotechnol. Bioeng. *118*, 4550–4576. https://doi.org/10.1002/bit.27933.

66. Blume, S.Y., Garg, A., Martí-Mateos, Y., Midha, A.D., Chew, B.T.L., Lin, B., Yu, C., Dick, R., Lee, P.S., Situ, E., et al. (2025). HypoxyStat, a small-molecule form of hypoxia therapy that increases oxygen-hemoglobin affinity. Cell *188*, 1580–1588.e11. https://doi.org/10.1016/j.cell.2025.01.029.

67. Long, D., Liu, M., Li, H., Song, J., Jiang, X., Wang, G., and Yang, X. (2021). Dysbacteriosis induces abnormal neurogenesis via LPS in a pathway requiring NF-κB/IL-6. Pharmacol. Res. *167*, 105543. https://doi.org/10.1016/j.phrs.2021.105543.

68. Lier, J., Streit, W.J., and Bechmann, I. (2021). Beyond Activation: Characterizing Microglial Functional Phenotypes. Cells *10*, 2236. https://doi.org/10.3390/cells10092236.

69. Bank, H.L. (1987). Assessment of islet cell viability using fluorescent dyes. Diabetologia *30*, 812–816. https://doi.org/10.1007/BF00275748.

70. Tabata, H., and Nakajima, K. (2008). Labeling embryonic mouse central nervous system cells by in utero electroporation. Dev. Growth Differ. *50*, 507–511. https://doi.org/10.1111/j.1440-169X.2008.01043.x.

71. Wonders, C.P., and Anderson, S.A. (2006). The origin and specification of cortical interneurons. Nat. Rev. Neurosci. *7*, 687–696. https://doi.org/10.1038/nrn1954.

72. Sultan, K.T., and Shi, S.H. (2018). Generation of diverse cortical inhibitory interneurons. Wiley Interdiscip. Rev. Dev. Biol. *7*. https://doi.org/10.1002/wdev.306.

73. Lim, L., Mi, D., Llorca, A., and Marín, O. (2018). Development and Functional Diversification of Cortical Interneurons. Neuron *100*, 294–313. https://doi.org/10.1016/j.neuron.2018.10.009.

74. Antypa, M., Faux, C., Eichele, G., Parnavelas, J.G., and Andrews, W.D. (2011). Differential gene expression in migratory streams of cortical interneurons. Eur. J. Neurosci. *34*, 1584–1594. https://doi.org/10.1111/j.1460-9568.2011.07896.x.

75. Marín, O., and Rubenstein, J.L.R. (2003). Cell migration in the forebrain. Annu. Rev. Neurosci. *26*, 441–483. https://doi.org/10.1146/annurev.neuro.26.041002.131058.

76. Jiménez, D., López-Mascaraque, L.M., Valverde, F., and De Carlos, J.A. (2002). Tangential migration in neocortical development. Dev. Biol. *244*, 155–169. https://doi.org/10.1006/dbio.2002.0586.

77. Marín, O. (2013). Cellular and molecular mechanisms controlling the migration of neocortical interneurons. Eur. J. Neurosci. *38*, 2019–2029. https://doi.org/10.1111/ejn.12225.

78. Su, Z., Tong, Y., and Wei, G.-W. (2024). Hodge Decomposition of Single-Cell RNA Velocity. J. Chem. Inf. Model. *64*, 3558–3568. https://doi.org/10.1021/acs.jcim.4c00132.

79. Selby, L., Zhang, C., and Sun, Q.-Q. (2007). Major defects in neocortical GABAergic inhibitory circuits in mice lacking the fragile X mental retardation protein. Neurosci. Lett. *412*, 227–232. https://doi.org/10.1016/j.neulet.2006.11.062.

80. La Fata, G., Gärtner, A., Domínguez-Iturza, N., Dresselaers, T., Dawitz, J., Poorthuis, R.B., Averna, M., Himmelreich, U., Meredith, R.M., Achsel, T., et al. (2014). FMRP regulates multipolar to bipolar transition affecting neuronal migration and cortical circuitry. Nat. Neurosci. *17*, 1693–1700. https://doi.org/10.1038/nn.3870.

81. Selimbeyoglu, A., Kim, C.K., Inoue, M., Lee, S.Y., Hong, A.S.O., Kauvar, I., Ramakrishnan, C., Fenno, L.E., Davidson, T.J., Wright, M., et al. (2017). Modulation of prefrontal cortex excitation/inhibition balance rescues social behavior in CNTNAP2-deficient mice. Sci. Transl. Med. *9*, eaah6733. https://doi.org/10.1126/scitranslmed.aah6733.

82. Vogt, D., Cho, K.K.A., Shelton, S.M., Paul, A., Huang, Z.J., Sohal, V.S., and Rubenstein, J.L.R. (2018). Mouse Cntnap2 and Human CNTNAP2 ASD Alleles Cell Autonomously Regulate PV+ Cortical Interneurons. Cereb. Cortex *28*, 3868–3879. https://doi.org/10.1093/cercor/bhx248.

83. Moldrich, R.X., Leanage, G., She, D., Dolan-Evans, E., Nelson, M., Reza, N., and Reutens, D.C. (2013). Inhibition of histone deacetylase in utero causes sociability deficits in postnatal mice. Behav. Brain Res. *257*, 253–264. https://doi.org/10.1016/j.bbr.2013.09.049.

84. Nicolini, C., and Fahnestock, M. (2018). The valproic acid-induced rodent model of autism. Exp. Neurol. *299*, 217–227. https://doi.org/10.1016/j.expneurol.2017.04.017.

85. Utz, S.G., See, P., Mildenberger, W., Thion, M.S., Silvin, A., Lutz, M., Ingelfinger, F., Rayan, N.A., Lelios, I., Buttgereit, A., et al. (2020). Early Fate Defines Microglia and Non-parenchymal Brain Macrophage Development. Cell *181*, 557–573.e18. https://doi.org/10.1016/j.cell.2020.03.021.

86. Ransohoff, R.M., and Cardona, A.E. (2010). The myeloid cells of the central nervous system parenchyma. Nature *468*, 253–262. https://doi.org/10.1038/nature09615.

87. Sheikh, B.N., Bondareva, O., Guhathakurta, S., Tsang, T.H., Sikora, K., Aizarani, N., Sagar, H., Holz, H., Grün, D., Hein, L., et al. (2019). Systematic Identification of Cell-Cell Communication Networks in the Developing Brain. iScience *21*, 273–287. https://doi.org/10.1016/j.isci.2019.10.026.

88. Ch'ng, E.S., and Kumanogoh, A. (2010). Roles of Sema4D and plexin-B1 in tumor progression. Mol. Cancer *9*, 251. https://doi.org/10.1186/1476-4598-9-251.

89. Garcia-Diaz, B., Bachelin, C., Coulpier, F., Gerschenfeld, G., Deboux, C., Zujovic, V., Charnay, P., Topilko, P., and Baron-Van Evercooren, A. (2019). Blood vessels guide Schwann cell migration in the adult demyelinated CNS through Eph/ephrin signaling. Acta Neuropathol. *138*, 457–476. https://doi.org/10.1007/s00401-019-02011-1.

90. Hatanaka, Y., Kawasaki, T., Abe, T., Shioi, G., Kohno, T., Hattori, M., Sakakibara, A., Kawaguchi, Y., and Hirata, T. (2019). Semaphorin 6A–Plexin A2/A4 Interactions with Radial Glia Regulate Migration Termination of Superficial Layer Cortical Neurons. iScience *21*, 359–374. https://doi.org/10.1016/j.isci.2019.10.034.

91. Silva, C.G., Peyre, E., Adhikari, M.H., Tielens, S., Tanco, S., Van Damme, P., Magno, L., Krusy, N., Agirman, G., Magiera, M.M., et al. (2018). Cell-Intrinsic Control of Interneuron Migration Drives Cortical Morphogenesis. Cell *172*, 1063–1078.e19. https://doi.org/10.1016/j.cell.2018.01.031.

92. Hupe, M., Li, M.X., Kneitz, S., Davydova, D., Yokota, C., Kele, J., Hot, B., Stenman, J.M., and Gessler, M. (2017). Gene expression profiles of brain endothelial cells during embryonic development at bulk and single-cell levels. Sci. Signal. *10*, eaag2476. https://doi.org/10.1126/scisignal.aag2476.

93. Egea, J., and Klein, R. (2007). Bidirectional Eph–ephrin signaling during axon guidance. Trends Cell Biol. *17*, 230–238. https://doi.org/10.1016/j.tcb.2007.03.004.

94. Brors, D., Bodmer, D., Pak, K., Aletsee, C., Schäfers, M., Dazert, S., and Ryan, A.F. (2003). EphA4 provides repulsive signals to developing cochlear ganglion neurites mediated through ephrin-B2 and -B3. J. Comp. Neurol. *462*, 90–100. https://doi.org/10.1002/cne.10707.

95. Fu, A.K.Y., Hung, K.-W., Huang, H., Gu, S., Shen, Y., Cheng, E.Y.L., Ip, F.C.F., Huang, X., Fu, W.-Y., and Ip, N.Y. (2014). Blockade of EphA4 signaling ameliorates hippocampal synaptic dysfunctions in mouse models of Alzheimer's disease. Proc. Natl. Acad. Sci. USA *111*, 9959–9964. https://doi.org/10.1073/pnas.1405803111.

96. Hattori, Y., and Miyata, T. (2018). Microglia extensively survey the developing cortex via the CXCL12/CXCR4 system to help neural progenitors to acquire differentiated properties. Genes Cells *23*, 915–922. https://doi.org/10.1111/gtc.12632.

97. Jiang, D., Burger, C.A., Akhanov, V., Liang, J.H., Mackin, R.D., Albrecht, N.E., Andrade, P., Schafer, D.P., and Samuel, M.A. (2022). Neuronal signal-regulatory protein alpha drives microglial phagocytosis by limiting microglial interaction with CD47 in the retina. Immunity *55*, 2318–2335.e7. https://doi.org/10.1016/j.immuni.2022.10.018.

98. Squarzoni, P., Oller, G., Hoeffel, G., Pont-Lezica, L., Rostaing, P., Low, D., Bessis, A., Ginhoux, F., and Garel, S. (2014). Microglia Modulate Wiring of the Embryonic Forebrain. Cell Rep. *8*, 1271–1279. https://doi.org/10.1016/j.celrep.2014.07.042.

99. Favuzzi, E., Huang, S., Saldi, G.A., Binan, L., Ibrahim, L.A., Fernández-Otero, M., Cao, Y., Zeine, A., Sefah, A., Zheng, K., et al. (2021). GABA-receptive microglia selectively sculpt developing inhibitory circuits. Cell *184*, 4048–4063.e32. https://doi.org/10.1016/j.cell.2021.06.018.

100. Hattori, Y. (2023). The microglia-blood vessel interactions in the developing brain. Neurosci. Res. *187*, 58–66. https://doi.org/10.1016/j.neures.2022.09.006.

101. Chen, S., Li, J., Meng, S., He, T., Shi, Z., Wang, C., Wang, Y., Cao, H., Huang, Y., Zhang, Y., et al. (2023). Microglia and macrophages in the neuro-glia-vascular unit: From identity to functions. Neurobiol. Dis. *179*, 106066. https://doi.org/10.1016/j.nbd.2023.106066.

102. Arnold, T., and Betsholtz, C. (2013). The importance of microglia in the development of the vasculature in the central nervous system. Vasc. Cell *5*, 4. https://doi.org/10.1186/2045-824X-5-4.

103. Shah, S.T.H., and Xuezhi, X. (2021). Traditional and modern strategies for optical flow: an investigation. SN Appl. Sci. *3*. https://doi.org/10.1007/s42452-021-04227-x.

104. Wang, G., Zhang, J., Hu, X., Zhang, L., Mao, L., Jiang, X., Liou, A.K.F., Leak, R.K., Gao, Y., and Chen, J. (2013). Microglia/macrophage polarization dynamics in white matter after traumatic brain injury. J. Cereb. Blood Flow Metab. *33*, 1864–1874. https://doi.org/10.1038/jcbfm.2013.146.

105. Napoli, I., and Neumann, H. (2009). Microglial clearance function in health and disease. Neuroscience *158*, 1030–1038. https://doi.org/10.1016/j.neuroscience.2008.06.046.

106. Lawrence, A.R., Canzi, A., Bridlance, C., Olivié, N., Lansonneur, C., Catale, C., Pizzamiglio, L., Kloeckner, B., Silvin, A., Munro, D.A.D., et al. (2024). Microglia maintain structural integrity during fetal brain morphogenesis. Cell *187*, 962–980.e19. https://doi.org/10.1016/j.cell.2024.01.012.

107. Patten, J., and Wang, K. (2021). Fibronectin in development and wound healing. Adv. Drug Deliv. Rev. *170*, 353–368. https://doi.org/10.1016/j.addr.2020.09.005.

108. Ousman, S.S., and Kubes, P. (2012). Immune surveillance in the central nervous system. Nat. Neurosci. *15*, 1096–1101. https://doi.org/10.1038/nn.3161.

109. Kamimura, D., Tanaka, Y., Hasebe, R., and Murakami, M. (2020). Bidirectional communication between neural and immune systems. Int. Immunol. *32*, 693–701. https://doi.org/10.1093/intimm/dxz083.

110. Kabata, H., and Artis, D. (2019). Neuro-immune crosstalk and allergic inflammation. J. Clin. Investig. *129*, 1475–1482. https://doi.org/10.1172/jci124609.

111. Farrar, J.D. (2020). Neuro-immune interactions. Semin. Immunopathol. *42*, 667–668. https://doi.org/10.1007/s00281-020-00825-w.

112. Scott-Hewitt, N., Mahoney, M., Huang, Y., Korte, N., Yvanka de Soysa, T., Wilton, D.K., Knorr, E., Mastro, K., Chang, A., Zhang, A., et al. (2024). Microglial-derived C1q integrates into neuronal ribonucleoprotein complexes and impacts protein homeostasis in the aging brain. Cell *187*, 4193–4212.e24. https://doi.org/10.1016/j.cell.2024.05.058.

113. Rustenhoven, J., and Kipnis, J. (2022). Brain borders at the central stage of neuroimmunology. Nature *612*, 417–429. https://doi.org/10.1038/s41586-022-05474-7.

114. Muñoz-Castro, C., Mejias-Ortega, M., Sanchez-Mejias, E., Navarro, V., Trujillo-Estrada, L., Jimenez, S., Garcia-Leon, J.A., Fernandez-Valenzuela, J.J., Sanchez-Mico, M.V., Romero-Molina, C., et al. (2023). Monocyte-derived cells invade brain parenchyma and amyloid plaques in human Alzheimer's disease hippocampus. Acta Neuropathol. Commun. *11*, 31. https://doi.org/10.1186/s40478-023-01530-z.

115. Zhao, M., Tuo, H., Wang, S., and Zhao, L. (2020). The Roles of Monocyte and Monocyte-Derived Macrophages in Common Brain Disorders. BioMed Res. Int. *2020*, 9396021. https://doi.org/10.1155/2020/9396021.

116. Orsenigo, F., Stewart, A., Hammer, C.P., Clarke, E., Simpkin, D., Attia, H., Rockall, T., Gordon, S., and Martinez, F.O. (2024). Unifying considerations and evidence of macrophage activation mosaicism through human CSF1R and M1/M2 genes. Cell Rep. *43*, 114352. https://doi.org/10.1016/j.celrep.2024.114352.

117. Ge, R., Tornero, D., Hirota, M., Monni, E., Laterza, C., Lindvall, O., and Kokaia, Z. (2017). Choroid plexus-cerebrospinal fluid route for monocyte-derived macrophages after stroke. J. Neuroinflamm. *14*, 153. https://doi.org/10.1186/s12974-017-0909-3.

118. Wang, H., Huang, Q., Zhang, Z., Ji, J., Sun, T., and Wang, D. (2022). Transient post-operative overexpression of CXCR2 on monocytes of traumatic brain injury patients drives monocyte chemotaxis toward cerebrospinal fluid and enhances monocyte-mediated immunogenic cell death of neurons in vitro. J. Neuroinflamm. *19*, 171. https://doi.org/10.1186/s12974-022-02535-6.

119. Xu, H., Lotfy, P., Gelb, S., Pragana, A., Hehnly, C., Byer, L.I.J., Shipley, F.B., Zawadzki, M.E., Cui, J., Deng, L., et al. (2024). The choroid plexus synergizes with immune cells during neuroinflammation. Cell *187*, 4946–4963.e17. https://doi.org/10.1016/j.cell.2024.07.002.

120. Ruprecht, V., Monzo, P., Ravasio, A., Yue, Z., Makhija, E., Strale, P.O., Gauthier, N., Shivashankar, G.V., Studer, V., Albiges-Rizo, C., et al. (2017). How cells respond to environmental cues - insights from bio-functionalized substrates. J. Cell Sci. *130*, 51–61. https://doi.org/10.1242/jcs.196162.

121. Berzat, A., and Hall, A. (2010). Cellular responses to extracellular guidance cues. EMBO J. *29*, 2734–2745. https://doi.org/10.1038/emboj.2010.170.

122. Stanco, A., Szekeres, C., Patel, N., Rao, S., Campbell, K., Kreidberg, J.A., Polleux, F., and Anton, E.S. (2009). Netrin-1-alpha3beta1 integrin interactions regulate the migration of interneurons through the cortical marginal zone. Proc. Natl. Acad. Sci. USA *106*, 7595–7600. https://doi.org/10.1073/pnas.0811343106.

123. López-Bendito, G., Luján, R., Shigemoto, R., Ganter, P., Paulsen, O., and Molnár, Z. (2003). Blockade of GABA(B) receptors alters the tangential migration of cortical neurons. Cereb. Cortex *13*, 932–942. https://doi.org/10.1093/cercor/13.9.932.

124. Southwell, D.G., Paredes, M.F., Galvao, R.P., Jones, D.L., Froemke, R.C., Sebe, J.Y., Alfaro-Cervello, C., Tang, Y., Garcia-Verdugo, J.M., Rubenstein, J.L., et al. (2012). Intrinsically determined cell death of developing cortical interneurons. Nature *491*, 109–113. https://doi.org/10.1038/nature11523.

125. Southwell, D.G., Froemke, R.C., Alvarez-Buylla, A., Stryker, M.P., and Gandhi, S.P. (2010). Cortical plasticity induced by inhibitory neuron transplantation. Science *327*, 1145–1148. https://doi.org/10.1126/science.1183962.

126. Li, G., Adesnik, H., Li, J., Long, J., Nicoll, R.A., Rubenstein, J.L.R., and Pleasure, S.J. (2008). Regional distribution of cortical interneurons and development of inhibitory tone are regulated by Cxcl12/Cxcr4 signaling. J. Neurosci. *28*, 1085–1098. https://doi.org/10.1523/JNEUROSCI.4602-07.2008.

127. Miyoshi, G., Ueta, Y., Yagasaki, Y., Kishi, Y., Fishell, G., Machold, R.P., and Miyata, M. (2024). Developmental trajectories of GABAergic cortical interneurons are sequentially modulated by dynamic FoxG1 expression levels. Proc. Natl. Acad. Sci. USA *121*, e2317783121. https://doi.org/10.1073/pnas.2317783121.

128. Trimm, E., and Red-Horse, K. (2022). Vascular endothelial cell development and diversity. Nat. Rev. Cardiol. *20*, 197–210. https://doi.org/10.1038/s41569-022-00770-1.

129. Tata, M., Ruhrberg, C., and Fantin, A. (2015). Vascularisation of the central nervous system. Mech. Dev. *138*, 26–36. https://doi.org/10.1016/j.mod.2015.07.001.

130. Mancuso, M.R., Kuhnert, F., and Kuo, C.J. (2008). Developmental Angiogenesis of the Central Nervous System. Lymph. Res. Biol. *6*, 173–180. https://doi.org/10.1089/lrb.2008.1014.

131. Hattori, Y. (2021). The behavior and functions of embryonic microglia. Anat. Sci. Int. *97*, 1–14. https://doi.org/10.1007/s12565-021-00631-w.

132. Ou, Z., Duh, Y.S., Rommelfanger, N.J., Keck, C.H.C., Jiang, S., Brinson, K., Jr., Zhao, S., Schmidt, E.L., Wu, X., Yang, F., et al. (2024). Achieving optical transparency in live animals with absorbing molecules. Science *385*, eadm6869. https://doi.org/10.1126/science.adm6869.

133. Zhang, Y., Wang, M., Zhu, Q., Guo, Y., Liu, B., Li, J., Yao, X., Kong, C., Zhang, Y., Huang, Y., et al. (2024). Long-term mesoscale imaging of

3D intercellular dynamics across a mammalian organ. Cell *187*, 6104–6122.e25. https://doi.org/10.1016/j.cell.2024.08.026.

134. Schefzik, R., Flesch, J., and Goncalves, A. (2021). Fast identification of differential distributions in single-cell RNA-sequencing data with waddR. Bioinformatics *37*, 3204–3211. https://doi.org/10.1093/bioinformatics/btab226.

135. Singh, S.P., Wang, L., Gupta, S., Goli, H., Padmanabhan, P., and Gulyás, B. (2020). 3D Deep Learning on Medical Images: A Review. Sensors (Basel) *20*, 5097. https://doi.org/10.3390/s20185097.

136. Radtke, A.J., Chu, C.J., Yaniv, Z., Yao, L., Marr, J., Beuschel, R.T., Ichise, H., Gola, A., Kabat, J., Lowekamp, B., et al. (2022). IBEX: an iterative immunolabeling and chemical bleaching method for high-content imaging of diverse tissues. Nat. Protoc. *17*, 378–401. https://doi.org/10.1038/s41596-021-00644-9.

137. Agarwal, A., Gupta, S., and Singh, D.K. (2016). Review of optical flow technique for moving object detection 2nd International Conference on Contemporary Computing and Informatics (IC3I), pp. 409–413. https://doi.org/10.1109/IC3I.2016.7917999.

138. Hengzhen, G., Mrinal, K.M., Gencheng, G., and Jianwei, W. (2010). Singular point detection using Discrete Hodge Helmholtz Decomposition in fingerprint images. IEEE International Conference on Acoustics, Speech and Signal Processing, pp. 1094–1097.

139. Bhatia, H., Pascucci, V., and Bremer, P.-T. (2014). The Natural Helmholtz-Hodge Decomposition for Open-Boundary Flow Analysis. IEEE Trans. Vis. Comput. Graph. *20*, 1566–1578. https://doi.org/10.1109/tvcg.2014.2312012.

140. Akram, M., and Michel, V. (2010). Regularisation of the Helmholtz decomposition and its application to geomagnetic field modelling. GEM Int. J. Geomath. *1*, 101–120. https://doi.org/10.1007/s13137-010-0001-y.

141. Zhang, Y., Kan, Z., Yang, Y., Tse, Y.A., and Wang, M.Y. (2019). Effective Estimation of Contact Force and Torque for Vision-Based Tactile Sensors With Helmholtz–Hodge Decomposition. IEEE Robot. Autom. Lett. *4*, 4094–4101. https://doi.org/10.1109/lra.2019.2930477.

142. Kendall, D.G. (1977). The diffusion of shape. Adv. Appl. Probab. *9*, 428–430. https://doi.org/10.2307/1426091.

143. Bhatia, H., Gyulassy, A., Wang, H., Bremer, P., and Pascucci, V. (2014). Robust Detection of Singularities in Vector Fields (Springer International Publishing), pp. 3–18.

144. Edelsbrunner, H., and Mücke, E.P. (1990). Simulation of Simplicity: A Technique to Cope with Degenerate Cases in Geometric Algorithms. ACM Trans. Graph. *9*, 66–104. https://doi.org/10.1145/77635.77639.

145. Lavin, Y., Batra, R., and Hesselink, L. (1998). Feature Comparisons of Vector Fields Using Earth Mover's Distance. In Proceedings Visualization '98 (Cat. No.98CB36276) (IEEE), pp. 103–109. https://doi.org/10.1109/VISUAL.1998.745291.

146. Anselin, L. (1995). Local Indicators of Spatial Association—LISA. Geogr. Anal. *27*, 93–115. https://doi.org/10.1111/j.1538-4632.1995.tb00338.x.

147. Emerson, C.W., Lam, N.S.N., and Quattrochi, D.A. (2007). A comparison of local variance, fractal dimension, and Moran's I as aids to multispectral image classification. Int. J. Remote Sens. *26*, 1575–1588. https://doi.org/10.1080/01431160512331326765.

148. Zhang, C., Luo, L., Xu, W., and Ledwith, V. (2008). Use of local Moran's I and GIS to identify pollution hotspots of Pb in urban soils of Galway, Ireland. Sci. Total Environ. *398*, 212–221. https://doi.org/10.1016/j.scitotenv.2008.03.011.

149. Mathur, M. (2015). Spatial autocorrelation analysis in plant population: An overview. J. Appl. Nat. Sci. *7*, 501–513. https://doi.org/10.31018/jans.v7i1.639.

STAR★METHODS

KEY RESOURCES TABLE

REAGENT or RESOURCE	SOURCE	IDENTIFIER
Antibodies		
anti-PDGFRB, goat (1:200)	R&D systems	Cat# AF385, RRID: AB_355339
anti-PAX6, rabbit (1:400)	Proteintech	Cat# 12323-1-AP, RRID: AB_2159695
anti-TBR1, mouse (1:400)	Proteintech	Cat# 66564-1-Ig, RRID: AB_2883604
anti-DCX, rabbit (1:400)	CST	Cat# 4604S, RRID: AB_561007
anti-OLIG2, mouse (1:400)	Millipore	Cat# MABN50, RRID: AB_10807410
anti-PH3, mouse (1:200)	CST	Cat# 9706S, RRID: AB_331748
anti-Cleaved Caspase-3, rabbit (1:200)	CST	Cat# 9661S, RRID: AB_2341188
anti-P2Y12, rabbit (1:200)	CST	Cat# 69766S, RRID: AB_2943477
anti-GFP, chicken (1:500)	Aves	Cat# GFP-1010, RRID: AB_2307313
anti-KI67, rabbit (1:200)	Abcam	Cat# ab16667, RRID: AB_302459
anti-CD68, rat (1:200)	Abcam	Cat# ab53444, RRID: AB_869007
anti-CD206, rat (1:500)	BioLegend	Cat# 141701, RRID: AB_10900263
anti-FN1, rabbit (1:200)	Millipore	Cat# AB2033, RRID: AB_2105702
Anti-CSF1R, rabbit (1:500)	Abcam	Cat# ab254357, RRID: AB_2927559
Donkey anti-Mouse, Alexa Fluor Plus 488	Thermo Fisher Scientific	Cat# A32766, RRID: AB_2762823
Donkey anti-Chicken, Alexa Fluor 488	Thermo Fisher Scientific	Cat# A78948, RRID: AB_2921070
Donkey anti-Goat, Alexa Fluor 488	Abcam	Cat# ab150133, RRID: AB_2832252
Donkey anti-Rabbit, Alexa Fluor 488	Thermo Fisher Scientific	Cat# A-21206, RRID: AB_2535792
Donkey anti-Rabbit, Alexa Fluor 568	Thermo Fisher Scientific	Cat# A10037, RRID: AB_11180865
Donkey anti-Rat, Alexa Fluor 568	Abcam	Cat# ab175475, RRID: AB_2636887
Donkey anti-Rabbit, Alexa Fluor 647	Abcam	Cat# ab150063, RRID: AB_2687541
Chemicals, peptides, and recombinant proteins		
Biotinylated IB4	Vector Laboratories	Cat# B-1205
Streptavidin, Alexa Fluor 546 conjugate	Thermo Fisher Scientific	Cat# S11225
Fast-Green dye	Sigma-Aldrich	Cat# F7252
Tamoxifen	Sigma-Aldrich	Cat# T5648-1G
Corn oil	Sigma-Aldrich	Cat# C8267
Tomato Lectin-488	Vector Laboratories	Cat# DL-1174-1
Tomato Lectin-594	Vector Laboratories	Cat# DL-1177-1
Low melting-point agarose	Yeasen	Cat# 10214ES60
Stroke-physiological saline solution	Leagene	Cat# CZ0030
Sodium citrate	Aladdin	Cat# S116311
Normal donkey serum	Jackson ImmunoResearch	Cat# 017-000-121
PBS (1x)	Servicebio	Cat# G4202
PBS (20x)	Solarbio	Cat# P1032
Triton X100	Sigma-Aldrich	Cat# T8787
Hibernate-E Medium	Gibco	Cat# A1247601
D-(+)-Trehalose dihydrate	Sigma-Aldrich	Cat# T0167-100G
Pronase	Roche	Cat# 10165921001
AOPI	Countstar	Cat# RE010211
Hoechst	Beyotime	Cat# C1022
Antifade mounting medium	Leagene	Cat# IH0252
Eukitt Quick-hardening mounting medium	Sigma-Aldrich	Cat# 03989

(*Continued on next page*)

Continued

REAGENT or RESOURCE	SOURCE	IDENTIFIER
Tribromoethanol	Sigma-Aldrich	Cat# T48402
Tertiary amyl alcohol	Sigma-Aldrich	Cat# 240486
Optical adhesive	Norland Products	Cat# NOA63
Resin	Wenext	Cat# 8200Pro
Trizol	Thermo Scientific	Cat# 15596018
Chloroform	Sinoreagent	Cat# 10006818
Isopropanol	Sinoreagent	Cat# 80109218
EdU	Beyotime	Cat# ST067
Valproic acid sodium salt	Sigma-Aldrich	Cat# P4543
KYL peptide	MedChemExpress	Cat# HY-P2264
Critical commercial assays		
Modified Lillie-Mayer Hematoxylin Staining Kit	Leagene	Cat# DH0001
Fast Wright's-Giemsa Stain kit	Yeasen	Cat# 60529ES01
HiPure Plasmid EF Maxi Kit	Magen	Cat# P1156
HiScript III All-in-one RT SuperMix Perfect for qPCR	Vazyme	Cat# R333
Taq Pro Universal SYBR qPCR Master Mix	Vazyme	Cat# Q712
Click-iT™ Plus EdU Alexa Fluor™ 647 Imaging Kit	Thermo Fisher Scientific	Cat# C10640
Deposited data		
scRNA-seq data	Bilal et al.[87]	GEO: GSE133079
bulk RNA-seq for embryonic interneurons	Carla et al.[91]	GEO: GSE104090
bulk RNA-seq for embryonic microglia	Sebastian et al.[85]	GEO: GSE146928
bulk RNA-seq for embryonic brain endothelial cells	Mike et al.[92]	GEO: GSE79306
Experimental models: Organisms/strains		
Mouse: *SST*$^{Cre+/+}$	The Jackson Laboratory	RRID: IMSR_JAX:018973
Mouse: *Emx1*$^{CreERT2/+}$	The Jackson Laboratory	RRID: IMSR_JAX:027784
Mouse: *Nkx2.1*$^{CreER+/-}$	The Jackson Laboratory	RRID: IMSR_JAX:014552
Mouse: *Cx3cr1*$^{GFP+/+}$	Qionghai Dai laboratory (Tsinghua University)	RRID: IMSR_JAX:008451
Mouse: *R26*$^{Ai14+/+}$	The Jackson Laboratory	RRID: IMSR_JAX:007914
Mouse: C57BL/6J	The Jackson Laboratory	RRID: IMSR_JAX:000664
Oligonucleotides		
Vegfa Forward: TGGTTCTTCACTCC CTCAAATC	This paper	N/A
Vegfa Reverse: GGTCTCTCTCTCTCT TCCTTGA	This paper	N/A
Acer2 Forward: GTGCGAGGACAACTA CACTATC	This paper	N/A
Acer2 Reverse: CACATGCAGATGGG AGGTAAA	This paper	N/A
Adm Forward: ATGTCTCAGCAAGG TGTAAGG	This paper	N/A
Adm Reverse: TTCTTCATCCACAGGC GATAAT	This paper	N/A
Angpt2 Forward: ACAGCTGTGATGATAGA GATTGG	This paper	N/A

(*Continued on next page*)

Continued

REAGENT or RESOURCE	SOURCE	IDENTIFIER
Angpt2 Reverse: CGAGTCTTGTCGTCT GGTTTAG	This paper	N/A
Depp1 Forward: CTCTCTCTAGCTTT CCTCTCCT	This paper	N/A
Depp1 Reverse: GCTAGACTGTCAT CGCTCTTT	This paper	N/A
IL-6 Forward: AGTCCGGAGAGG AGACTTCA	This paper	N/A
IL-6 Reverse: ATTTCCACGATTTC CCAGAG	This paper	N/A
IL-1β Forward: CTTTGAAGTTGAC GGACCC	This paper	N/A
IL-1β Reverse: TGAGTGATACTGC CTGCCTG	This paper	N/A
TNF-α Forward: CACCACCATCAAG GACTCAA	This paper	N/A
TNF-α Reverse: AGGCAACCTGACC ACTCTCC	This paper	N/A
GAPDH Forward: CATGGCCTTCCG TGTTCCTA	This paper	N/A
GAPDH Reverse: GCCTGCTTCACCA CCTTCTT	This paper	N/A
Recombinant DNA		
LV-CMV-EGFP-T2A-Puro-WPRE	This paper	N/A
Software and algorithms		
Blender	Blender 4.2 LTS	https://www.blender.org/
ImageJ	NIH Image for the Macintosh	https://imagej.nih.gov/ij/index.html; RRID: SCR_003070
Imaris 10.0	Oxford Instruments	https://imaris.oxinst.com/; RRID: SCR_007370
OlyVIA	Olympus Microsystems	https://www.olympus-lifescience.com/en/downloads/detail-iframe/?0[downloads][id]=847252030; RRID: SCR_016167
Dragonfly 2002.1	ORS, Montreal, version 2022.1	https://www.theobjects.com/index.html; RRID: SCR_025150
GraphPad Prism 9.5	GraphPad Software	RRID: SCR_000306
Python 3.10.11	Python	https://www.python.org; RRID: SCR_008394
R software 4.2.2	GNU Project	https://www.r-project.org/; RRID: SCR_001905
MATLAB	Mathworks	https://www.mathworks.com/products/matlab.html; RRID: SCR_001622
Illustrator CC 2021	Adobe	https://www.adobe.com/products/illustrator.html; RRID: SCR_010279
Cellpose 3.0.7	Cellpose software	https://www.cellpose.org; RRID: SCR_021716
R package: Plotly 4.10.4	GitHub	https://github.com/plotly/plotly.R; RRID: SCR_013991
R package: WaddR 1.16.0	Schefzik et al.[134]	https://github.com/goncalves-lab/waddR
R package: Circular 0.5-0	GitHub	https://github.com/cran/circular
R package: pheatmap 1.0.12	GitHub	https://github.com/raivokolde/pheatmapSCR_016418
R package: metR 0.15.0	GitHub	https://github.com/eliocamp/metR;
R package: Seurat 4.4	GitHub	https://github.com/satijalab/seurat
R package: CellChat 2.1.2	GitHub	https://github.com/jinworks/CellChat
Python: SimpleITK 2.2.1	GitHub	https://github.com/SimpleITK/SimpleITK; RRID: SCR_024693
Python: OpenCV 4.7.0.72	GitHub	https://github.com/opencv/opencv; RRID: SCR_015526
Python: POT 0.9.4	GitHub	https://github.com/PythonOT/POT

(*Continued on next page*)

Continued

REAGENT or RESOURCE	SOURCE	IDENTIFIER
Python: SciPy 1.10.1	GitHub	https://github.com/scipy/scipy; RRID: SCR_008058
HHD	Zhe et al.[78]	https://github.com/WeilabMSU/HHD
Construction of vector fields by interpolation	This study	https://github.com/MiLabTsinghua/IMEE
L^2 norm	This study	https://github.com/MiLabTsinghua/IMEE
Others		
Multiphoton Laser Scanning Microscope FVMPE-RS	Olympus	https://www.olympus-lifescience.com/en/laser-scanning/fvmpe-rs/
Olympus SpinSR10 spinning disk confocal super resolution microscope	Olympus	https://www.olympus-lifescience.com/en/super-resolution/spinsr10/
Olympus VS200 Slide Scanner	Olympus	https://www.olympus-lifescience.com/en/solutions-based-systems/vs200/; RRID: SCR_024783
SMZ745/745T stereoscopic microscope	Nikon	https://www.microscope.healthcare.nikon.com/products/stereomicroscopes-macroscopes/smz745-745t
R500 Small Animal Anesthesia Machine	RWD	https://www.rwdstco.com/product-item/r500-rodent-anesthesia-machine/
Countstar Rigel S3	Countstar	https://www.countstar.cn/productshow.php?cid=5&id=22
Sutter P-2000 Laser Micropipette Puller	SUTTER INSTRUMENT	https://www.sutter.com/MICROPIPETTE/p-2000.html; RRID: SCR_018640
ECM 830 Square Wave Electroporation System	BTX	https://www.btxonline.com/ecm-830-square-wave-electroporation-system.html; RRID: SCR_016841
Drummond PCR Pipettes	Drummond Scientific	https://pipette.com/drummond-5-000-1001-x10.html?srsltid=AfmBOopCoq7DuZqrhvgKLJUklUxJMsfcrpmYq92fmobd8KiOdWRxme8s
Drummond Capillaries	Drummond Scientific	https://www.fishersci.com/shop/products/drummond-replacement-capillaries-nanojet-ii-injectors/211714
Peristaltic Pump	LEFOO	https://www.lefoo.com/products/lfp104-quick-installation-peristaltic-pump
Micro Forceps	RWD	https://www.rwdstco.com/product-item/f11029-11/
VANNAS Spring Scissor	RWD	https://www.rwdstco.com/product-item/s11001-08/
Round cover glass	Solarbio	http://www.solarbio.net/goods-10928.html
Optical Plate	Fly-opt	http://www.fly-opt.com/pd.jsp?id=39#keyword=otab&_pp=0_1873
NanoDrop 2000c spectrophotometer	Thermo Fisher Scientific	https://www.thermofisher.cn/order/catalog/product/cn/zh/840-317400
CFX96 Touch Real-Time PCR Detection System	Biorad	https://www.bio-rad.com/zh-cn/product/cfx96-touch-real-time-pcr-detection-system?ID=LJB1YU15

EXPERIMENTAL MODEL AND STUDY PARTICIPANT DETAILS

Wild type and all transgenic mouse lines used in this study are listed in the key resources table. All mice were maintained on a C57BL/6J background and housed under a 12 h light/dark cycle with *ad libitum* access to food and water. Only time-mated pregnant female mice were housed individually. The day of vaginal plug formation was considered E0.5. All the experimental procedures were approved by the Institutional Animal Care & Use Committee and the Animal Welfare and Ethics Committee of Tsinghua University, Beijing, China.

METHOD DETAILS

IMEE device

The bracket, chuck and pallet of the IMEE device were designed using Blender and 3D printed using resin material (Wenext, Cat# 8200Pro).

The round cover glass (Solarbio, Cat# YA0776-1pk) was glued on the chuck by UV curing optical adhesives (Norland Products, Cat# NOA63). The donut-shaped chuck was concave up, composed of an outer ring with shallower depth than the middle ring and a middle ring surrounding a hole in the middle. The outer ring maintained a steady stream of water coverage of the glass surface at the bottom, making the device suitable for the water immersion objective of two-photon microscopes; the inner ring acted as a reservoir for warm saline solution; and the hole in the middle was shaped as a conic frustum at the bottom of the chuck to better fit the shape of the fetal head. Four extended adaptors of the outer ring ensured stable attachment to the bracket, and among them, the bilateral hollow adaptors were connected to the water circulation system. In addition, the adaptor of the middle ring on one side was connected to the syringe through a pipe.

The donut-shaped pallet had a hollow interior that connected to the water circulation system via bilateral adaptors of the pallet, which allowed the flowing of the heated water. Bilateral poles were attached to the pallet with screws, thereby forming rotatable joints, allowing the adjustment of the height of the pallet to various maternal physiques.

IMEE experiments

Device preparation

Before surgery, we first prepared the IMEE components used for immobilization. The bracket and the pole were installed to the optical plate (Fly-opt, Cat# OTAB). The chuck of suitable size was used for each embryonic age. The three hoses were respectively connected to the hollow adaptors of the outer ring and the middle ring of the chuck, and the hose attaching the middle ring was also connected to the syringe with a valve. The warm saline solution was injected through the syringe, moisturizing the chuck while removing all air bubbles. The water-proof PU film was glued to the bottom of the pallet, which supported the embryo with an upward force. The heating pad was attached to the lifting table with gummed tapes. The 3% low melting-point agarose (Yeasen, Cat# 10214ES60) was prepared and incubated in a water bath at 55°C. Next, we prepared the water circulation component. The peristaltic pump (LEFOO, Cat# LFP104) was connected with a glass bottle containing 50 mL of distilled water through a hose, and this glass bottle was incubated in a water bath at 42°C, so that the water flowing via the hose was maintained at 37°C when passing through the chuck. Finally, the gas anesthesia component was set up and ready to run before intravital imaging.

Surgery

First, pregnant females were anesthetized with Avertin (2.5% Avertin reservoir in 0.9% NaCl saline solution) by intraperitoneal injection at a dose of 0.02 ml/g of body weight. Avertin reservoir was formulated from 100% (w/v) Tribromoethanol (Sigma-Aldrich, Cat# T48402) dissolved in Tertiary amyl alcohol (Sigma-Aldrich, Cat# 240486). The mouse was placed on the heated lifting table and their feet were secured with gummed tapes. The appropriate amount of erythromycin eye ointment was applied to the mouse eyes. After depilation and disinfection of the mouse's abdomen, a longitudinal incision was performed along the midline of the abdomen through the skin and muscle layers, followed by placement of a sterile gauze.

Second, part of the uterus was exposed, and a fissure was created in the uterine wall by the VANNAS Spring Scissor (RWD, Cat# S11001-08) to separate an embryo for the subsequent operation (Methods S1). A hole was created, slightly larger than the cross-sectional area of the embryo, in the PU film at the bottom of the pallet. And the embryo was carefully passed through the hole and subsequently the pallet was stabilized by their bilateral rotatable poles being fixed with two pieces of cube-shaped clay (Methods S1).

Third, the uterine wall near the top of the fetal head was delicately clamped by micro forceps (RWD, Cat# F11029-11) and partially scissored by the VANNAS spring scissor (RWD, Cat# S11001-08), without any disruption to the fetal amnion. The orientation of the embryo in the amniotic fluid was adjusted by the tip cotton swabs to the desired viewing angle. The lifting table was placed beneath the bracket and raised slowly until the fetal amnion reached the liquid inside the hole of the chuck. The amnion was closely attached to the cover glass of the chuck as a result of the suction from the syringe (Methods S1). Then the valve between the syringe and the hose was sealed off slowly before detaching the syringe.

Fourth, the optical plate, along with the aforementioned attachments, was placed under the objective of the two-photon microscope, and the fluorescent signals inside the brain were quickly examined. If no desired signals were observed, another adjacent embryo would be taken out and pass through the PU film of the pallet, and then the third procedure described above would be performed on this embryo. Instead, between the chuck and pallet, the low-melting point agarose was added around the embryo, and the valve was opened to release pressure. Simultaneously, the gas anesthesia and water circulation components were turned on for long-term intravital imaging. The concentration of isoflurane was gradually increased to 0.5% and remained stable until the end of imaging.

Image acquisition

In vivo images were acquired with an Olympus FVMPE-RS multiphoton laser scanning microscope equipped with an Olympus XLPLAN N 25X objective (NA1.05). The blood cells in cortical vasculature were imaged in the resonant scanning mode, averaging five frames (6 fps; 0.994 pixel / μm) (Figure S1F; Videos S3 and S8), while the other *in vivo* images were acquired in the Galvano scanning mode. The step size between each image in each stack was 10 μm (Figures 2, 3, 6, 7, and S4B–S4F) or 5 μm (Figures 4, 5, S4J, S4K, and S5G). Stack images were first processed in ImageJ. The 3D reconstruction of images was performed using volume rendering in Imaris. The volume could be optically sliced at any position using the "Orthoslicer" tool. The 3D displays of interactions were rendered using "Surface" tool in Imaris. The 3D pictures and movies were generated using "Snapshot" tool and "Animation" tool in Imaris.

ENDOGENOUS TRANSGENIC LABELING

For sparse labeling of excitatory neurons, *Emx1*$^{CreERT2/+}$; *R26*$^{Ai14+/+}$ males were crossed with wild-type C57/B6 females. At 24 hours prior to IMEE, pregnant females were injected intraperitoneally with tamoxifen (Sigma-Aldrich, Cat# T5648-1G) dissolved in corn oil (Sigma-Aldrich, Cat# C8267) at E12.5 or E14.5 at a dose of 2.5 μg/g of body weight. For labeling of cortical interneurons, *Nkx2.1*$^{CreER+/-}$; *R26*$^{Ai14+/+}$ males were crossed with wild-type C57/B6 females. At 48 hours prior to IMEE, pregnant females were injected intraperitoneally with tamoxifen dissolved in corn oil at E12.5 at a dose of 25 μg/g or 100 μg/g of body weight for sparse or dense labeling, respectively.

VPA-INDUCED MOUSE MODEL

Nkx2.1$^{CreER+/-}$; *R26*$^{Ai14+/+}$ males were crossed with wild-type C57/B6 females. Pregnant females carrying E12.5 embryos were injected intraperitoneally with VPA (Sigma-Aldrich, Cat# P4543) dissolved in saline solution at a dose of 600mg/kg of body weight. Control animals were administered equivalent volumes of vehicle (saline solution) alone. Following 48 hours of VPA exposure (from E12.5 to E14.5), we performed IMEE on VPA-exposed and control embryos at E14.5.

IN UTERO RETRO-ORBITAL INJECTION

Pregnant wild-type females, mated to *Cx3cr1*$^{GFP+/+}$ males or *Nkx2.1*$^{CreER+/-}$; *R26*$^{Ai14+/+}$ males, carrying E11.5, E12.5 or E14.5 embryos were anesthetized with isoflurane (3.5% for induction, 2% during the surgery). The uterine horns were exposed after laparotomy, and ∼ 1 μL Tomato Lectin-488 (Vector Laboratories, Cat#DL-1174-1) or Tomato Lectin-594 (Vector Laboratories Cat#DL-1177-1) mixed with 1% Fast-Green dye (Sigma-Aldrich, Cat# F7252) was injected through the uterine wall into the eye of each embryo using a pulled glass micropipette (Drummond Scientific, Cat# 5-000-1001-X10). After the procedure, the abdomen was filled with an antibiotic/analgesic-containing phosphate-buffered saline (PBS) and the wound was closed using a surgical suture and wound clips on the skin. The embryos were left to recover in the mother's womb for 2 hours followed by IMEE or immunohistochemistry.

For EphA4 blockade, ∼1μl of KYL peptide solution (1mM in saline; MedChemExpress, Cat# HY-P2264) together with ∼ 1 μl Tomato Lectin-488 (containing 1% Fast-Green dye) were injected through the uterine wall into the eye of each embryo using a pulled glass micropipette. Control embryos received equivalent volumes of saline with Lectin-488/Fast Green mixture. After surgery, embryos were left to recover in the mother's womb for 4 hours followed by IMEE.

IN UTERO ELECTROPORATION

Pregnant wild-type females carrying E14.5 embryos were anesthetized with isoflurane (3.5% for induction, 2% during the surgery). The uterine horns were exposed after laparotomy, and ∼ 0.5 μL DNA (at a concentration of 1-3 mg/ml mixed with 1% Fast-Green dye [Sigma-Aldrich, Cat# F7252]) was injected through the uterine wall into the lateral ventricle of each embryo using a pulled glass micropipette (Drummond Scientific, Cat# 5-000-1001-X10). For electroporation, five pulses (50 ms each, 950-ms intervals) of 35 mV were delivered dorsolaterally at an ∼ 45° angle through the embryonic brain to target the lateral cortex using 5-mm electrode paddles connected to a BTX ECM830 electroporator. After the procedure, the abdomen was filled with an antibiotic/analgesic-containing PBS solution and the wound was closed using a surgical suture and wound clips on the skin. The mice were placed on heating pads to recover. After waking up, the mice were housed individually for three days before the following IMEE.

IN UTERO LESIONS

Pregnant wild-type females, mated to *Cx3cr1*$^{GFP+/+}$ males, carrying E14.5 embryos were anesthetized with isoflurane (3.5% for induction, 2% during the surgery). The uterine horns were exposed after laparotomy. IULs were induced unilaterally using a 100 μm diameter glass capillary (Drummond Scientific, Cat# 3-000-203-G/X), which pierced through the cortical plate horizontally to reach the contralateral hemisphere of embryos at E14.5. After the procedure, the abdomen was filled with an antibiotic/analgesic-containing PBS solution and the wound was closed using a surgical suture and wound clips on the skin. Lesioned E14.5 embryos were left to recover in the mother's womb for 2.5 h and were collected for immunohistochemistry, or recover for 30 minutes followed by the IMEE.

Pregnant wild-type females, mated to *Cx3cr1*$^{GFP+/+}$ males, carrying E11.5 or E12.5 embryos were anesthetized with Avertin (2.5% Avertin reservoir in 0.9% NaCl saline solution) by intraperitoneal injection at a dose of 0.02 ml/g of body weight. The uterine horns were exposed after laparotomy, and ∼ 1 μl Tomato Lectin-594 mixed with 1% Fast-Green dye was injected through the uterine wall into the eye of each embryo using a pulled glass micropipette. Following IU-ROI, IULs were induced unilaterally using a 100 μm diameter glass capillary, which pierced either through the cortical plate horizontally to reach the contralateral hemisphere of embryos at E12.5 or in the hindbrain of embryos at E11.5. After 10 minutes post-IULs, we performed IMEE for *in vivo* observations or collected brain samples for immunohistochemistry.

IMMUNOHISTOCHEMISTRY

The brains were isolated from embryos and incubated in 4% PFA for 2-4 h on a slow-speed rocking platform at 4°C. Tissue was washed with PBS, incubated in 15% followed by 30% sucrose in PBS and sliced with a freezing microtome into 16 μm coronal sections, and stored at -20°C or processed for immunohistochemistry. Coronal sections were stained using the following primary antibodies: goat anti-PDGFRB (1/200; R&D systems, Cat# AP385, RRID: AB_355339), rabbit anti-PAX6 (1/400; Proteintech, Cat# 12323-1-AP, RRID:AB_2159695), mouse anti-Tbr1 (1/200; Proteintech, Cat# 66564-1-Ig, RRID: AB_2883604), rabbit anti-DCX (1/400; Cell Signaling Technology, Cat# 4604S, RRID: AB_561007), mouse anti-OLIG2 (1/400; Millipore Cat# MABN50, RRID:AB_10807410), mouse anti-PH3 (1/200; Cell Signaling Technology, Cat# 9706S, RRID: AB_331748), rabbit anti-Cleaved Caspase3 (1/200; Cell Signaling Technology, Cat# 9661S, RRID: AB_2341188), rabbit anti-P2Y12 (1/200; Cell Signaling Technology, Cat#69766S, RRID: AB_2943477), chicken anti-GFP (1/500; Aves Labs, Cat# GFP-1010, RRID:AB_2307313), rabbit anti-KI67 (1/200; Abcam, Cat# ab16667, RRID:AB_302459), rat anti-CD68 (1/200; Abcam, Cat# ab53444, RRID: AB_869007), rat anti CD206 (1/500; BioLegend, Cat# 141701, RRID: AB_10900263), rabbit anti-FN1 (1/200; Millipore, Cat# AB2033, RRID: AB_2105702), and rabbit anti-CSF1R (1/500; Abcam, Cat# ab254357, RRID: AB_2927559). Antigen retrieval was used for PAX6, TBR1, DCX, OLIG2, PH3, Cleaved Caspase-3 and KI67 immunohistochemistry. Sections were washed with PBS and then was blocked with 3% donkey serum in 0.25% triton-X-100-PBS for 1h at RT. Primary antibodies were incubated overnight at 4 °C in 3% donkey serum in 0.2% triton-X-100-PBS. The following secondary antibodies conjugated to Alex Fluor dyes were used: donkey anti-mouse IgG (H+L) 488, donkey anti-chicken IgY (H+L) 488, donkey anti-rabbit IgG (H+L) 488, and donkey anti-rabbit IgG (H+L) 568 (all from Thermo Fisher Scientific, used at 1/1000); donkey anti-goat IgG (H+L) 488, donkey anti-rat IgG (H+L) 568, donkey anti-rabbit IgG (H+L) 647 (all from Abcam, used at 1/1000). Secondary antibodies were incubated for 2 h at RT followed by Hoechst (1/1000; Beyotime, Cat# C1022) for 10 minutes at RT. In between steps, sections were washed three times for 10 minutes with 0.2% triton-X-100 in PBS. Brain sections were mounted in Antifade mounting medium (Leagene, Cat# IH0252). Brain sections were imaged using an Olympus SpinSR10 spinning disk confocal super-resolution microscope (20x Apochromat/NA0.8). Subsequent image processing was performed using ImageJ.

EdU labeling and detection

Solution of EdU (Beyotime, Cat# ST067) was dissolved in PBS (5 mg/ml) and shielded from light at all times. Immediately after IULs on E14.5 *Cx3cr1*$^{GFP+/-}$ mouse embryos, pregnant females were injected intraperitoneally with EdU at a dose of 50 mg/kg of body weight. We then harvested E14.5 embryos 2.5 hours after EdU administration for the subsequent staining. We used the Click-iT™ Plus EdU Alexa Fluor™ 647 Imaging kit (Thermo Fisher Scientific, Cat# C10640) for EdU detection.

H&E staining

Mouse embryos were incubated in 4% PFA overnight on a slow-speed rocking platform at 4°C. Tissue was washed with PBS, incubated in 10% followed by 30% sucrose in PBS and cut on a freezing microtome into 20 μm sagittal sections, and stored at -20°C or processed for H&E staining (Leagene Biotechnology, Cat# DH0001). Embryo sections were stained by hematoxylin solution for 10 min and eosin Y solution for 1 min. Then, sections were dehydrated and mounted in Eukitt Quick-hardening mounting medium (Sigma-Aldrich, Cat# 03989). Sections were imaged using an Olympus VS200 Slide Scanner (20X Apochromat/NA0.8). Subsequent image processing was performed using ImageJ.

CARDIOVASCULAR BLOOD TEST

The right atrium of the E14.5 embryos was gently opened. Three microliters of cardiovascular blood were collected via micropipette and immediately transferred to EDTA-anticoagulated tubes. One microliter of whole blood was uniformly smeared onto microscope slides. The Fast Wright's-Giemsa Stain Kit (Yeasen Biotech, Cat# 60529ES01) was used in the following staining. The smears were dipped completely into the mixture of Wright's-Giemsa solution for 7 min and were gently rinsed with distilled water. The sections were dried at RT and mounted in Eukitt Quick-hardening mounting medium (Sigma-Aldrich, Cat# 03989). Sections were imaged using an Olympus VS200 Slide Scanner (20X Apochromat/NA0.8). Subsequent image processing was performed using ImageJ. Neutrophils and monocytes were counted within 1 cm^2 monolayer regions of each smear slide according to standardized morphological criteria: Neutrophils were identified by their segmented nuclei (2-5 lobes; cell diameter 10-12 μm), while monocytes were distinguished by their kidney-shaped or lobulated nuclei (diameter 12-20 μm).

CELL VIABILITY MEASUREMENT

Mouse embryos isolated from timed pregnant females were stored in 1x PBS on ice and then their telencephalons were dissected out. Dissected tissue was then immediately transferred to warm (37°C) lysis solution (Hibernate-E Medium [Gibco, Cat# A1247601] containing 1x Pronase [Roche, Cat# 10165921001] and 2% D-(+)-Trehalose dihydrate [Sigma-Aldrich, Cat#T0167-100G]) in a 15 ml conical tube and incubated for 15 min at 37°C. After centrifugation, cells were re-suspended in 1x PBS and filtered through a 35-μm cell strainer (Falcon, Cat# 352235). Then, we employed the AOPI viability assay, a well-established fluorescence-based technique

that enables simultaneous discrimination of live (AO^+) and dead (PI^+) cell populations.[69] A 10 μL cell suspension was removed and mixed with the same volume of AOPI (Countstar, Cat#RE010211). Following AOPI staining, cell viability was automatically quantified using a Cell Counter (Countstar Rigel S3).

REAL-TIME PCR

Embryonic brains were collected either without IMEE treatment or following 8-hour/12-hour IMEE procedure. Dissected samples were immediately lysed using Pronase (Roche, Cat# 10165921001) and then transferred to 1 ml Trizol (Thermo Scientific, Cat# 15596018). Samples were incubated at room temperature for 5 minutes, then 200 μL of chloroform (Sinoreagent, Cat# 10006818) was added and mixed. After another 10-minute incubation at room temperature, samples were centrifuged at 12,000 rpm for 15 minutes at 4°C. 300 μl of the aqueous layer was collected and mixed with 300 μl isopropanol (Sinoreagent, Cat# 80109218). After incubating at room temperature for 10 minutes, samples were centrifuged at 12,000 rpm for 10 minutes at 4°C. Samples were placed on ice, and the supernatant was removed. 1 ml of 75% ethanol was added before centrifuging at 8000 rpm for 5 minutes at 4°C. Following the removal of supernatant, 20-50 μl DEPC water was added, depending on the size of the pellet. RNA concentration and quality was determined using a NanoDrop One spectrophotometer (Thermo Fisher Scientific). Samples containing 1 μg RNA were reverse transcribed using the HiScript III All-in-one RT SuperMix Perfect for qPCR kit (Vazyme, Cat# R333). Resulting cDNA was stored at -20°C. For each qPCR reaction, 10 μl 2x Taq Pro Universal SYBR qPCR Master Mix (Vazyme, Cat# Q712) was mixed with 8.2 μl water, 0.8 μl of forward and reverse primer mix, and 1 μl cDNA in a well of a 96-well plate. Each sample was run in triplicate. The plate was then sealed and inserted into a CFX96 (Biorad) for determination of cycle threshold (CT) values. Thermal cycle scheme was: 50°C for 2 minutes, 95°C for 10 minutes, then 40 cycles of 95°C for 15 seconds and 60°C for 1 minute, followed by 95°C for 15 seconds, 60°C for 1 minute, and 95°C for 15 seconds. For each set of triplicates, an average CT value was obtained, and the difference in average CT between the target gene and *GAPDH* was calculated (ΔCT). Next, the difference in ΔCT value between each sample and the average of the controls was calculated (ΔΔCT). Relative expression of each gene was determined by calculating $2^{-\Delta\Delta CT}$.

SECTION RECONSTRUCTION AND ALIGNMENT

The embryonic brains undergoing long-term *in vivo* imaging were cut serially on a freezing microtome into 16-μm coronal or sagittal sections. After immunohistochemistry, sections were imaged using an Olympus SpinSR10 spinning disk confocal super-resolution microscope (20x Apochromat/NA0.8) with a 5-μm z-axial resolution. Series of 16-μm sections were analyzed in sequential order. Adjacent sections were aligned by line regions of interest (ROI) using ImageJ based on the cortical axis and lateral ventricles. The image stack, composed of series of aligned sections, with an xy resolution of 3.15 pixels/μm and z resolution of 5 pixels/μm, was displayed in three dimensions using Imaris (Figures 1H and 7K).

The *in vivo* image stack captured by IMEE was mapped back to the reconstructed brain using ORS Dragonfly (version 2002.1, RRID:SCR_025150) (Figure 1H). The two input stacks were displayed as different color channels in the same three-dimensional space, which could be moved separately to align with each other, allowing for image detail inspection on two-dimensional layers.

MOTION CORRECTION OF TIME-LAPSE IMAGE STACKS

We used the registration method provided by the python module SimpleITK v2.2.1, which was widely used in biological and medical imaging.[135,136] The vast majority of the offsets when aligning the time-lapse *in vivo* image stacks were caused by parallel displacements as a result of the respiratory and bowel movements of the maternal mice. For image stacks of two adjacent time points, the initial values of parameter estimation in translatory motion were obtained by the ‘‘ImageRegistrationMethod’’ function. Based on the alignment of boundary structures and non-specific vasculature signals, transformation parameters were fine-tuned.

MODELING OF CELLULAR MOVEMENT TRAJECTORIES

For modelling the movement trajectories of a large number of interneurons, we used Cellpose (version 3.0.7, RRID: SCR_021716) to automatically recognize the somata of interneurons, generating the masks of somal locations. For each time point, we implemented two channels in ImageJ, one for the original image stack, the other for its mask. Based on the original image stacks, the movements of interneurons were traced manually between adjacent time points, with these newly established correspondences of somal locations between adjacent time points marked with the ‘‘Wand Tool’’ for individual neurons on the masks. The x, y and z coordinates of the center of each soma were determined by the ‘‘ROI Measurements’’ tool. We used the R package Plotly v4.10.4 to display these cellular movement trajectories in the three-dimensional space (Figures 3D, S3A, and S3B). For tangentially migrating interneurons, we calculated the angular speed as the derivative of migratory direction on the xy plane, and the linear speed in the three-dimensional space (Figures 3 and S3).

INDIVIDUAL CELL TRACKING

For the *in vivo* image stacks of sparsely labeled neurons and microglia, we used the ''Manual tracking with TrackMate'' tool in ImageJ to track the movement of individual cells. After motion correction of time-lapse image stacks, for the image stack of each time point, blocks containing the cells of interests were extracted and projected onto the xy-plane. These image projections on the xy-plane across time points were sequentially stacked in ImageJ. Finally, using ''Manual tracking with TrackMate'' tool, cellular movement trajectories were drawn and their track features were exported (Figure 7C; Videos S2, S4, S5, and S7).

TRANSCRIPTOMIC ANALYSIS

Single-cell RNA-seq data analysis

The single-cell RNA-seq data were obtained from GEO with accession number: GSE133079. Data analysis was performed using the R package Seurat. After quality check, data was first normalized using ''NormalizeData'' function (normalization.method = "LogNormalize", scale.factor = 10000), and PCA was performed. The dimensionality reduction and visualization were performed using the ''RunUMAP'' function, and the cell clustering was performed using FindClusters function. Differentially expressed (DE) genes were identified using ''FindMakers'' function in Seurat. We visualized cell type-specific gene expression patterns through heatmaps, wherein columns represent individual cells grouped by cluster identity and rows display z-score normalized expression values of selected marker genes. The ligand and receptor expression values as well as their interactions that inferred from the cell-cell communication network among neurons, microglia, and endothelial cells at E14.5 were obtained from the ''Brain interactome explorer'' (https://mpi-ie.shinyapps.io/braininteractomeexplorer).[87] We visualized the receptor-ligand pairing patterns with showing the specific ligand-receptor interaction strength (weighted by gene expression values) between any two cell populations using circle plot, provided by R package CellChat.

Bulk RNA-seq data analysis

The bulk RNA-seq data for embryonic interneurons were obtained from GEO (GSE133079), comprising three biological replicates at E13.5 (GSM2789662, GSM2789663, and GSM2789664); the bulk RNA-seq data for embryonic microglia were obtained from GEO (GSE146928), comprising four biological replicates at E14.5 (GSM4411099, GSM4411108, GSM4411109 and GSM4411110); and bulk RNA-seq data for embryonic brain endothelial cells were obtained from GEO (GSE79306), comprising three biological replicates at E13.5 (GSM2091176, GSM2091177, and GSM2091178) and three biological replicates at E15.5 (GSM2091218, GSM2091219, and GSM2091220). Gene expression levels were quantified as reads per kilobase per million mapped reads (RPKM) values. We visualized gene expression patterns through heatmaps, wherein columns represent biological replicates of different cell populations and rows display z-score normalized RPKM expression values of selected genes (Figure S5D). We visualized RPKM expression values of top ten genes for different cell populations through heatmaps (Figure S5E).

QUANTIFICATION AND STATISTICAL ANALYSIS

Statistical analysis

Results were plotted and tested for statistical significance using Prism 9.5 or R v4.3.3. Statistical significance between two groups was evaluated by Mann-Whitney U test, while Wilcoxon signed-rank test was utilized for paired two-group comparisons. For more than two groups, Kruskal-Wallis H test followed by Dunn's multiple comparisons or Two-way ANOVA followed by Bonferroni's multiple comparisons was performed. When evaluating the differences in probability distributions, we utilized Wasserstein test for non-circular data and Watson's U^2 test for circular data. Data were presented as either: (1) mean values together with the standard error, (2) violin plots displaying data distributions and median values (central line), or (3) box plots illustrating median values (central line), interquartile ranges (box boundaries), and paired data connections (green lines). The p values below 0.05 were considered statistically significant (*$p < 0.05$; **$p < 0.01$; ***$p < 0.001$; ****$p < 0.0001$; n.s., non significant). All of the statistical details of experiments, specifically the size and type of individual samples, were indicated and specified in the figure legends.

Topological analysis of vector fields

Construction of vector fields by interpolation or optical flows

For delineating the dynamics of interneuron migration at cell population level, we constructed the original vector fields based on the true velocity vectors of sampled neurons (Figures 3H, S3J, and S3K). We generated fixed 2D grid $\{\mathbf{X}_{jk} = (X_j, Y_k)\}_{j,k=1}^{L}$ with equal length (10 μm) for the step size in the 2 directions, which covered the half cortex. Some of grid points, location $\mathbf{x_i} = (x_i, y_i) \in \mathbb{R}^2$ and velocity $\mathbf{v_i} = (u_i, v_i) \in \mathbb{R}^2$, represented the true neuron samples, were obtained from our modeling of neuron movement trajectories. And for the other grid points, we used the strategy of mutual nearest neighbors (MNN) to select neuron samples for generating the velocity vectors and interpolations. To be specific, we calculated the distances between neuron samples and generated the distribution of distances. For interpolation, we chose neuron samples, whose distance to the grid point is in the lowest ten percent of the distribution, as its nearest neighbors. For each grid point $\mathbf{X}_{jk}$, we assigned a velocity vector $\mathbf{V}_{jk}$ based on its nearest neighbors, and we considered the following Gaussian smoothing:

$$\mathbf{V}_{jk} = \frac{\sum_{i \in I} \exp\left\{ -\frac{\left\|\mathbf{X}_{jk} - \mathbf{x}_i\right\|_2^2}{2\sigma^2} \right\} \mathbf{v}_i}{\sum_{i \in I} \exp\left\{ -\frac{\left\|\mathbf{X}_{jk} - \mathbf{x}_i\right\|_2^2}{2\sigma^2} \right\}}, \quad \text{(Equation 1)}$$

where $\|\cdot\|_2$ is the Euclidean metric, and the parameter I contains all the nearest neighbors of grid point $\mathbf{X}_{jk}$. The σ^2 is the blur parameter that controls the sharpness of Gaussian smoothing. We used $\sigma^2 = 10^3$ for all tasks.

For delineating the dynamics of microglial processes at individual cell level, we utilized the dense optical flow method, which is widely used in objects tracking and computer vision,[103,137] to construct the vector fields of the motions of cellular processes (Figures 6G and S6K). We first extracted the morphological profiles from the microglia of interests using ImageJ, and the central locations of cell bodies are determined manually by trained personnels. Next, all binarized contours are placed in the image grids of the same size, and the marked centers of cell bodies are aligned. To stabilize the generation of optical flows, we used the convolutional Wasserstein barycenter method provided by the python module POT v0.9.4 to interpolate transitory frames between adjacent time points. In practice, we interpolated 9 frames with weights vary from 0.1 to 0.9 by a step of 0.1. After such interpolation, we used DIS method provided by the python module OpenCV v4.7.0.72 to generate optical flows. Then, we used the 2D Gaussian density function provided by the python module SciPy v1.10.1 to generate a unified round boundary encircling all contours, ready for the HHD analysis.

Helmholtz-Hodge decomposition (HHD)

As a powerful and celebrated tool, Hodge decomposition could decompose any vector fields into three orthogonal vector fields, the curl-free, divergence-free and harmonic vector fields, facilitating deeper understanding of the topological properties of the original vector fields. In low dimensional space, it was also called Helmholtz-Hodge decomposition (HHD).[78,138–141] We used the HHD algorithm[78] (MATLAB toolbox from https://github.com/WeilabMSU/HHD) to decompose the original vector fields constructed based on cellular dynamics (Figures 3H, S3J, S3K, 6G, and S6K). Let M be a n-dim oriented smooth manifold and $\Omega^k(M)$ be all smooth differential k-forms ($k \leq n$). Then the Hodge theorem claims the following decomposition of $\Omega^k(M)$

$$\Omega^k(M) = \mathrm{Img}\left(\mathrm{d}^{k-1}\right) \oplus \mathrm{Img}\left(\delta^{k+1}\right) \oplus H_\Delta^k(M), \quad \text{(Equation 2)}$$

Where d, δ are differential and codifferential operator, respectively. $\mathrm{Img}(\cdot)$ is the image space, $H_\Delta^k(M) = Ker\left(\mathrm{d}^{k-1}\right) \cap Ker\left(\delta^{k+1}\right)$, $\mathrm{Ker}(\cdot)$ is the kernel space and $\oplus$ is the operational sign for direct sum. On 2D or 3D manifold, by viewing vector field as 1-form, we have the following decomposition:

$$\boldsymbol{v} = \nabla f + \nabla \times \mathbf{g} + \mathbf{h}, \quad \text{(Equation 3)}$$

where f is the scalar function, $\mathbf{g}$ and $\mathbf{h}$ are vectors. ∇f, $\nabla \times \mathbf{g}$, and $\mathbf{h}$ are curl-free, divergence-free and harmonic components of the original vector $\mathbf{v}$ and ∇ is gradient operator. Given reasonable boundary conditions, the decomposition in Equation 3 is unique. In 2D condition, the divergence-free component $\nabla \times \mathbf{g}$ degenerates to form $J\nabla g$, where g is a scalar function and J is a 2×2 matrix which rotates the vectors counterclockwise by $\frac{\pi}{2}$. For visualization of the vector fields, we used the R package metR v0.15.0.

Contribution of decomposed components analysis

In our study, we used the HHD on 2D compact regions. Equipped with the usual Euclidean metric $\|\cdot\|_2$, the three decomposed components were orthogonal to each other with respect to the usual vector inner product. And by taking square on the equation 3, we had

$$\|\boldsymbol{v}\|_2^2 = \|\nabla f\|_2^2 + \|\mathrm{J}\nabla \mathrm{g}\|_2^2 + \|\boldsymbol{h}\|_2^2. \quad \text{(Equation 4)}$$

These terms represented the energies of the original vector fields and three decomposed components. Moreover, we defined the ratio between energy of each decomposed component to the total energy as the contribution to the original vector field.

For velocity fields of cortical interneuron populations at 20-minute duration, the contributions of their decomposed vector fields were calculated and grouped into MZ and SVZ for the subsequent Two-way ANOVA followed by Bonferroni's multiple comparisons (Figure 3J). For each microglial cell, seven morphological profiles were extracted at 10-minute intervals over a 60-minute period (0, 10, 20, 30, 40, 50 and 60 minutes). Consequently, six original vector fields were generated per microglial cell. Each of these vector fields underwent HHD, yielding a total of 18 decomposed vector fields per cell (comprising 6 curl-free, 6 divergence-free, and 6 harmonic vector fields). The values for each microglial cell were derived from averaging the values of decomposed vector fields across all time points (Figures 6H, 6I, and S6I). The contributions of decomposed vector fields were grouped into CAMs and PCMs for the subsequent Two-way ANOVA followed by Bonferroni's multiple comparisons (Figure 6H).

Comparisons of vector fields

We calculated the L^2 norm for comparing vector fields constructed from cellular movement at cell population level (Figure 3I). Based on the ideas from functional data analysis (FDA), we compared each vector fields by viewing its energy as a continuous function in L^2 space equipped with the L^2 norm. Let $M \subseteq \mathbb{R}^2$ be a compact set and we define the L^2 space on M as

$$L^2(M) = \left\{ f : M \to \mathbb{R} \middle| \int_M |f|^2 dx < \infty \right\}, \quad \text{(Equation 5)}$$

i.e. all square-integrable functions supported on M. The L^2 norm is induced by the inner product $< f, g >_{L^2} = \int_M f\, g dx, \forall f, g \in L^2(M)$

$$\|f\|_{L^2} = \left(\int_M |f|^2 dx \right)^{1/2}, \quad \text{(Equation 6)}$$

where $(L^2(M), \|\cdot\|_{L^2})$ is a separable Hilbert space. Therefore, for any two energy functions E_1, E_2 of two different vector fields, we calculated their distance by L^2 norm as $d(E1, E2) = \|E1 - E2\|_{L^2}$. Then we hierarchically clustered the normalized distance values using the default clustering method of R package pheatmap v1.0.12.

As for comparing vector fields constructed from the cellular processes' motion of each individual microglial cell, we considered that the locational and rotational effects of such image data interfered with the analysis of cellular process dynamics.[142] Therefore, we standardized the somal locations of microglial cells and calculated topological features of each vector field based on its critical points. With the locational and rotational effects removed, subsequent comparisons of vector fields of different microglial cells were performed (Figure 6I). For robust detection of critical points, we utilize the combinatorial method created by Bhatia et al.[143] and the Simulation of Simplicity method for robust implementation.[144] Then, we extracted feature vectors of these critical points, forming feature distributions for each vector fields.[145] We hierarchically clustered the Wasserstein distance values, which are calculated from feature distributions, using the default clustering method of R package pheatmap v1.0.12.

Wasserstein distance

To compare two distributions, we used the Wasserstein distance and Wasserstein test provided by R package WaddR[134] v1.16.0. For $p \in [1, +\infty)$ and two Borel probability measure μ, ν with finite p-moments on $\mathbb{R}$, we have the Wasserstein distance in the following formulation as

$$W_p(\mu, \nu) = \left(\int_0^1 \left| F^{-1}(t) - G^{-1}(t) \right|^p dt \right)^{1/p}, \quad \text{(Equation 7)}$$

where $F^{-1}(\cdot)$ and $G^{-1}(\cdot)$ are quantile functions of measures μ and ν , respectively. Consider two discrete samples sampled from two 1D Borel probability measures μ and ν with n and m samples, respectively. Let $F_n^{-1}(t) = inf_x\{F_n(x) \geq t\}$ be the empirical quantile function, where $F_n(x) = \frac{1}{n} \sum_{i=1}^n I\{x_i \leq t\}$ is the empirical cumulative distribution function (ECDF). By plugging the ECDF in the Equation 6, we could calculate the distances between two empirical distributions, which we used in the subsequent clustering analysis.

In addition, we can construct goodness-of-fit test between two distributions based on Wasserstein distance. Under the null hypothesis H_0: $\mu = \nu$, we have an asymptotic distribution for the following test statistic as

$$\frac{mn}{m+n} W_p^p(G_{m\#}\mu_n, G_{\#}\mu) = \frac{mn}{m+n} \int_0^1 \left(G_m \circ F_n{}^{-1}(t) - t \right)^p dt \xrightarrow{w} \int_0^1 (B(t))^p dt, \quad \text{(Equation 8)}$$

where $G_{\#}(\mu)$ is the push-forward measure of μ by function $G(\cdot)$, $\xrightarrow{w}$ is weak convergence and B*(t)* is the standard Brownian bridge on [0,1]. Based on the conventional usage, we picked $p = 2$ in our study.

Circular statistics

When analyzing circular data, we considered the periodicity and expected the analysis method holding the rotation invariant property in general. Therefore, we used the Watson's U^2 test, provided by R package Circular v0.5-0, when comparing two distributions of circular data. Let $F_i, i = 1, 2$ be ECDFs of two circular datasets each with n_i observations. For null hypothesis $H_0 : F_1 = F_2$, consider the following Watson statistic

$$U^2_{n_1,n_2} = \frac{n_1 n_2}{n_1 + n_2} \int \left(F_1 - F_2 - \int (F_1 - F_2) dF^* \right)^2 dF^*, \quad \text{(Equation 9)}$$

where $F^* = \frac{n_1 F_1 + n_2 F_2}{n_1 + n_2}$. It can be shown that when $n_1, n_2 \to \infty, n_1 / n_2 \to \lambda, \lambda \in (0, 1)$, the tail probability of $U^2_{n_1,n_2}$ is given by

$$\lim_{n_1,n_2 \to \infty} \mathbb{P}\left(U^2_{n_1,n_2} > t \right) = 2 \sum_{k=1}^{\infty} (-1)^{k-1} e^{-2k^2\pi^2 t}. \quad \text{(Equation 10)}$$

Besides, we also used the Watson statistic in the clustering of the circular data.

Fluorescence intensity analysis

We drew a 30-μm line ROI on the muti-channel image, covering the position of cellular interactions. We used the "Plot Profile" tool in ImageJ to obtain the gray values of each pixel at different color channels. We normalized gray values of each group by the minimax method:

$$X_{normalized} = \frac{X - X_{min}}{X_{max} - X_{min}}. \quad \text{(Equation 11)}$$

Spatial association analysis

As a local indicator for spatial association, local Moran's *I* index can reflect the variations in the spatial association between regions of interest and their neighbors.[146–149] For our image data (Figures 4E–4G, 5E, and 5G), we utilized the bivariate local Moran's *I* index to evaluate the spatial association between the fluorescence intensities of two channels. We consider the nearby 8 pixels within a 3×3 grid to be the neighbors for the pixel in the center. Let W_{ij} be the spatial weight between the *i*th and *j*th pixels. If *i* and *j* are not neighbors, we take $W_{ij} = 0$; otherwise, we take the unnormalized weight as $W_{ij} = \exp\left(-\frac{1}{2}\left\|\boldsymbol{p_i} - \boldsymbol{p_j}\right\|_2^2\right)$, where $\boldsymbol{p_i}, \boldsymbol{p_j}$ are the coordinate of pixel *i* and *j*. The spatial weights of all neighbors of one pixel are normalized, such that their total sum equals to 1. We defined the two channels of the same ROI as X and Y. Let the Z-score normalized intensity of the *i*th pixel of X and Y to be x_i and y_i, respectively. Then, bivariate local Moran's *I* statistic is denoted as

$$I_i = x_i \sum_j W_{ij} y_j, \qquad \text{(Equation 12)}$$

where W_{ij} is the spatial weight of Y between pixel *i* and *j*. Therefore, we obtained the local spatial association between the *i*th pixel of X and Y as I_i.

To further test statistical significance of spatial association for each pixel, we utilized the conditional permutation test. For the channel Y, we fixed the intensity of pixel *i* and permutated the rest of the pixels for *B* times, generating the background distribution with $I'_{ib} (1 \leq b \leq B)$. Then we obtained *p* values as

$$p_i = \frac{1}{B} \sum_b \mathbb{I}\{I'_{ib} \geq I_i\}, \qquad \text{(Equation 13)}$$

where $\mathbb{I}\{\cdot\}$ is the indicator function. Considering multiple comparisons, we used the Benjamini-Hochberg method to obtain the adjusted *p* values. In practice, we set the green channel as X, the red channel as Y, and *B* as 10,000 for conditional permutation test.

Cell density

For immunostaining quantification, at least 3 sections of each brain spanning cortical regions on the rostrocaudal axial were quantified. ROIs were manually defined on E14.5 coronal sections. The 250 μm width ROIs were defined at the corresponding positions across sections and brains for the quantification of the numbers of $PAX6^+$, $TBR1^+$ and $PH3^+$ cells (Figures S2M–S2O, S2S, and S2U), while the numbers of DCX^+ and $OLIG2^+$ cells were calculated in the 250 μm × 500 μm regions at MGE (Figures S2P–S2R). The numbers of $P2Y12^+$, $P2Y12^+CD68^+$, Cleaved Caspase-3^+, $P2Y12^+$ GFP^+, and GFP^+ cells were quantified in a 1000 μm width ROI of each section (Figures S2J–S2L, S2T, S2V, S6B, and S6C). The cell numbers were quantified by "Cell Counter" tool in ImageJ.

CellPress
OPEN ACCESS

Supplemental figures

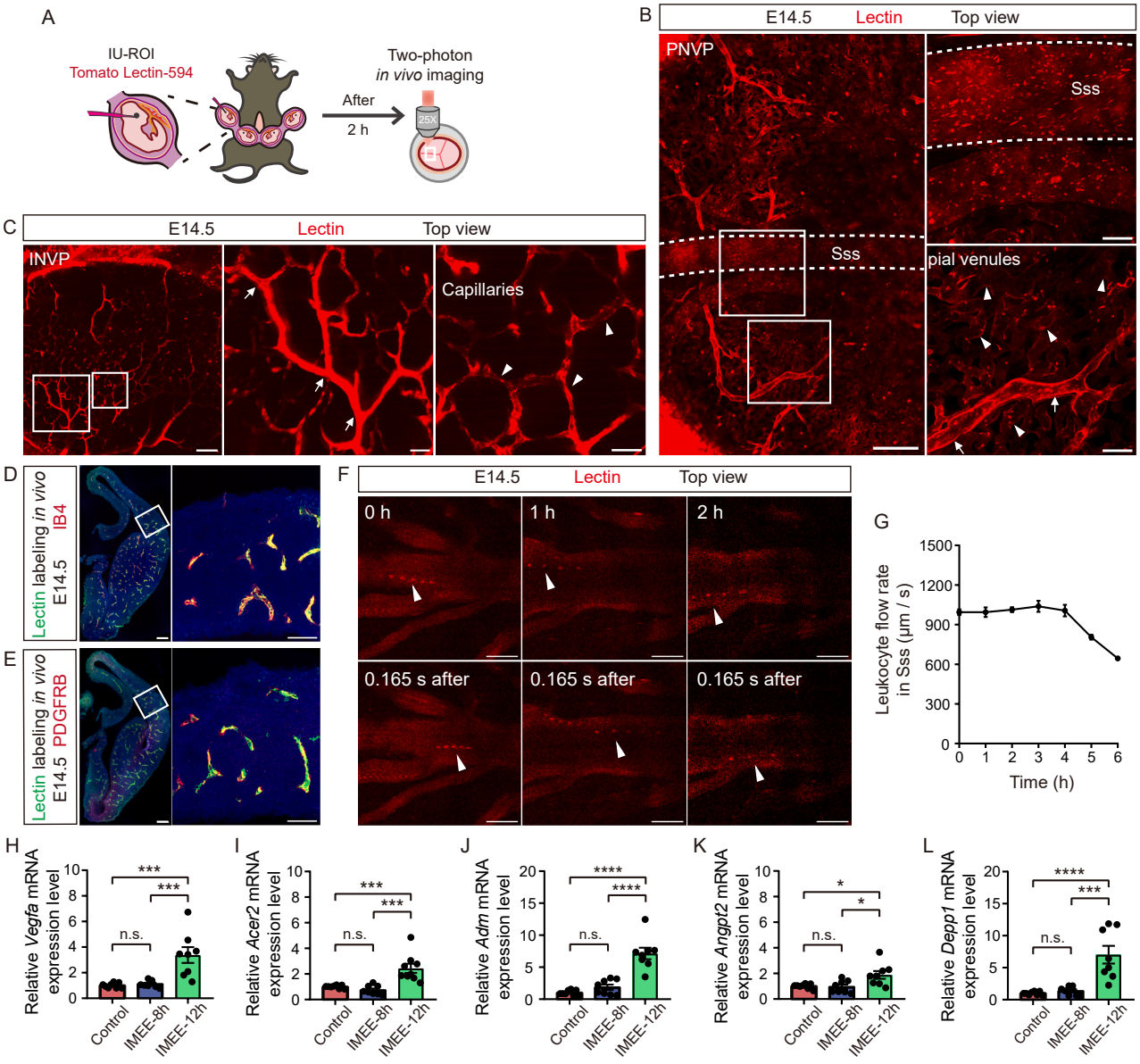

Figure S1. Intravital imaging of the vasculature in the developing mouse cortex, related to Figure 1

(A) Cortical vasculature labeling by IU-ROI and two-photon *in vivo* imaging.

(B) The top view *in vivo* images of perineural vascular plexus (PNVP) on the pial side at E14.5 (z = 150 μm). Arrows, penetrating arterioles; arrowheads, pial venules that converge to larger draining veins and sinuses; and Sss, superior sagittal sinuses. Scale bars, 200 μm (left) and 50 μm (right).

(C) The top view *in vivo* images of intraneural vascular plexus (INVP) in the brain parenchyma at E14.5 (z = 100 μm). Arrows, precapillary arterioles branching from the penetrating arterioles; arrowheads, capillaries. Scale bars, 200 μm (left) and 50 μm (middle and right).

(D and E) Coronal sections of the E14.5 embryonic brains were labeled by lectin-488 and were stained for IB4 (red) and Hoechst (blue) (D) and PDGFRB (red) and Hoechst (blue) (E). Scale bars, 500 μm (left) and 200 μm (right).

(F) The representative *in vivo* time-lapse sequence showing the flowing of tomato lectin-labeled leukocytes in the Sss. Arrowheads, flowing cells. Scale bars, 100 μm.

(G) Quantification of the flow rate of lectin-labeled leukocytes in the Sss at different time points at E14.5 (n = 4 embryos from 4 dams).

(H–L) Relative mRNA expression levels of *Vegfa* (H), *Acer2* (I), *Adm* (J), *Angpt2* (K), and *Depp1* (L) in E14.5 brains quantified by real-time PCR (n = 8 embryos from 8 dams per group).

Data: mean ± SEM. Statistics: Kruskal-Wallis H test followed by Dunn's multiple comparisons; n.s., non-significant ($p > 0.05$).

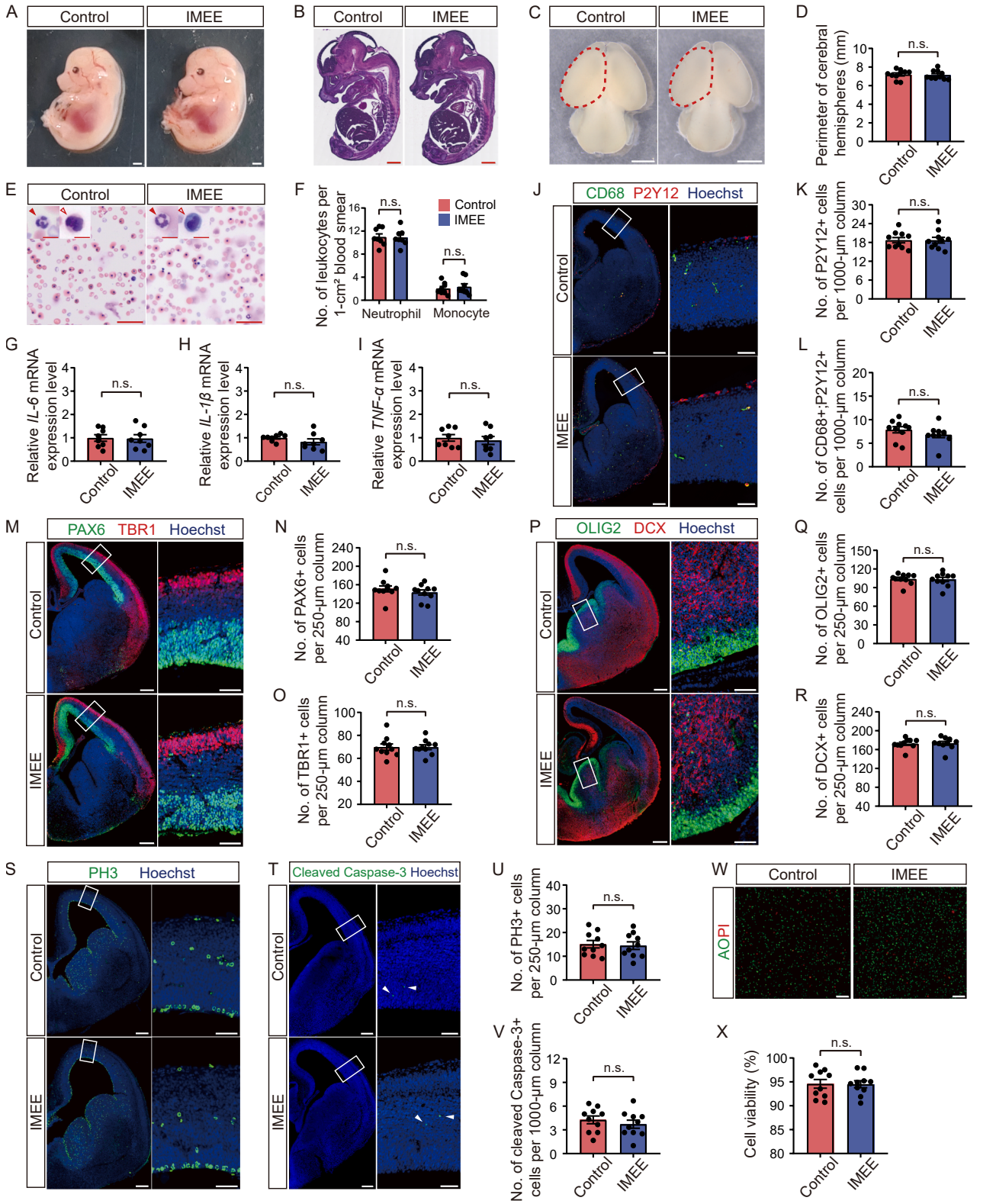

Figure S2. Normal development of mouse embryos during IMEE, related to Figure 1

(A) Images of the E14.5 embryos of control and 8-h IMEE groups. Scale bars, 1 mm.

(B) H&E staining of the E14.5 embryos of control and 8-h IMEE groups. Scale bars, 1 mm.

(legend continued on next page)

(C) Representative images of the E14.5 brains of control and 8-h IMEE groups. Scale bars, 1 mm.
(D) Quantification of the perimeters of the cerebral hemispheres (n = 10 embryos from 10 dams per group).
(E) Wright's-Giemsa staining of blood cells collected from E14.5 embryos of control and 8-h IMEE groups. Solid arrowheads, neutrophils; hollow arrowheads, monocytes. Scale bars, 50 μm and 10 μm (high magnification).
(F) Quantification of the number of neutrophils and monocytes per 1-cm^2 blood smear (n = 8 embryos from 8 dams per group).
(G–I) Relative mRNA expression levels of interleukin (*IL*)-*6* (G), *IL-1β* (H), and tumor necrosis factor alpha (*TNF-α*) (I) in E14.5 brain tissues of control and 8-h IMEE groups quantified by real-time PCR (n = 8 embryos from 8 dams per group).
(J, M, P, S, and T) Coronal sections of E14.5 brains of control and 8-h IMEE groups were stained for CD68 (activated microglia marker; green), P2Y12 (microglia marker; red), and Hoechst (blue) (J); PAX6 (cortical radial glial cell marker; green), TBR1 (cortical newborn neuron marker; red), and Hoechst (blue) (M); OLIG2 (subpallial radial glial cell marker; green), DCX (migrating neuron marker; red), and Hoechst (blue) (P); PH3 (dividing cell marker; green) and Hoechst (blue) (S); and cleaved caspase-3 (apoptotic cell marker; green) and Hoechst (blue) (T). Arrowheads indicate the cleaved caspase-3^+ cells. Scale bars, 200 μm (left) and 50 μm (right).
(K, L, N, O, Q, R, U, and V) Quantification of the number of $PAX6^+$ (N), $TBR1^+$ (O), $OLIG2^+$ (Q), DCX^+ (R), and $PH3^+$ (U) cells per 250-μm column and $P2Y12^+$ (K), $CD68^+P2Y12^+$ (L), and cleaved caspase-3^+ (V) cells per 1,000-μm column (n = 10 embryos from 10 dams per group).
(W) AOPI staining of cells dissociated from the developing mouse cortex of control and 8-h IMEE groups at E14.5. Scale bars, 100 μm.
(X) Quantification of cell viability of the developing mouse cortex (n = 10 embryos from 10 dams per group).
Data: mean ± SEM. Statistics: Mann-Whitney U test; n.s., non-significant ($p > 0.05$).

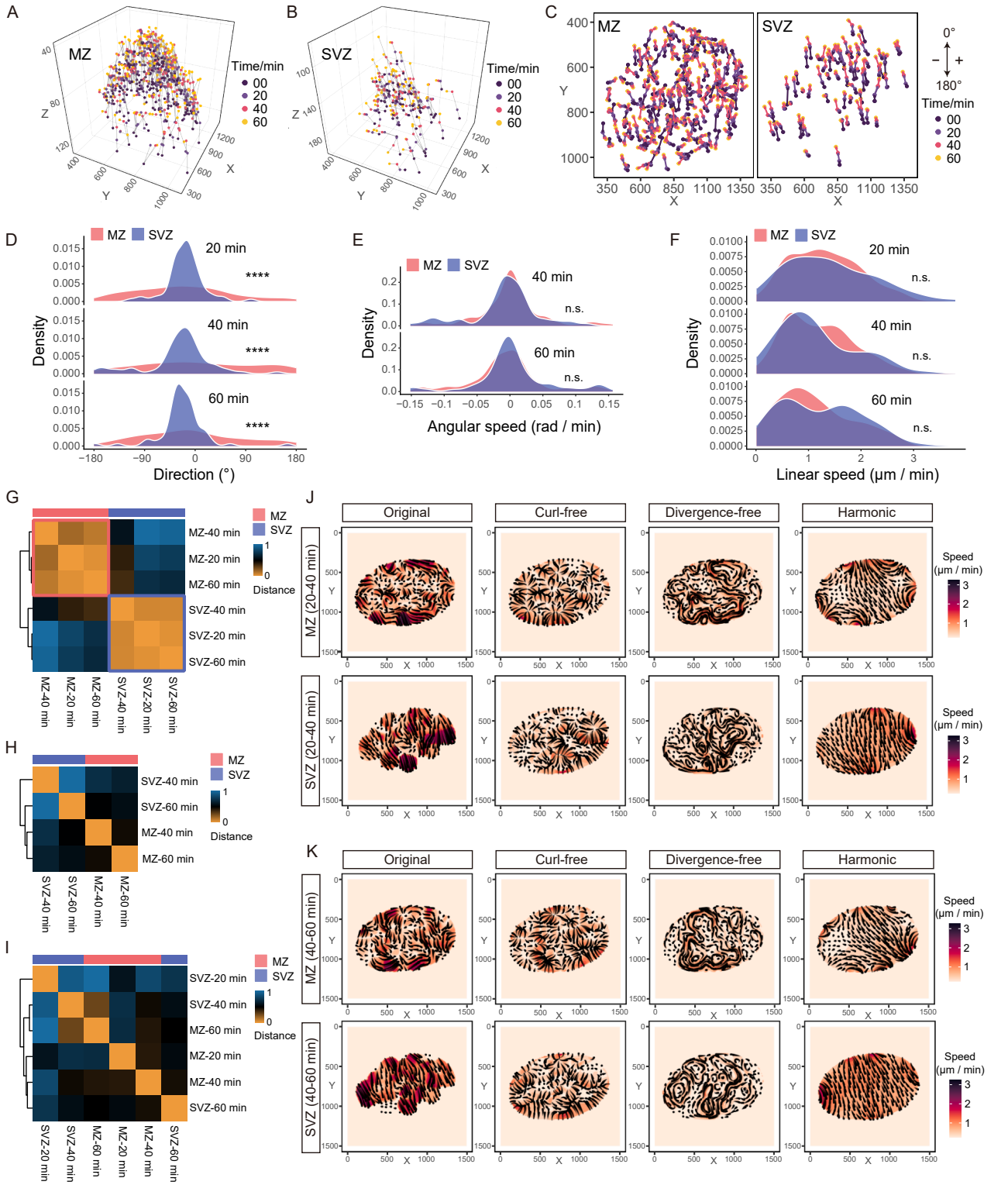

Figure S3. The analysis of migration trajectories of cortical interneurons using the TVF, related to Figure 3

(A and B) Modeling of interneuron migration trajectories in MZ (A) and SVZ (B). Each line shows the trajectory of a single neuron, connected by four colored nodes that represent the spatial position of the neuron at 0, 20, 40, and 60 min.

(C) The projection of the MZ (left) and the SVZ (right) interneuron migration trajectories on the plane parallel to the imaging top view.

(legend continued on next page)

(D–F) The distribution of the migration direction (D), angular speed (E), and linear speed (F) of migrating interneurons at 20-min durations (e.g., 0–20, 20–40, and 40–60 min). Angular speeds are the derivatives of directions, i.e., a 20 to 40 min angular speed corresponds to the measurements of direction from 0 to 20 and 20 to 40 min. MZ, $n = 249$ cells; SVZ, $n = 70$ cells; all cells from one embryo.

(G, H, and I) Heatmaps illustrating the distribution distances of the migration direction (G), angular speed (H), and linear speed (I) of the MZ and SVZ interneurons at different time points.

(J and K) The original velocity vector fields constructed by the velocity at which neurons migrate from 20 to 40 min (J) and 40 to 60 min (K), and their three decomposed components: curl-free, divergence-free, and harmonic vector fields.

Statistics: Watson test (D) and Wasserstein test (E and F); $^{****}p < 0.0001$, n.s., non-significant ($p > 0.05$).

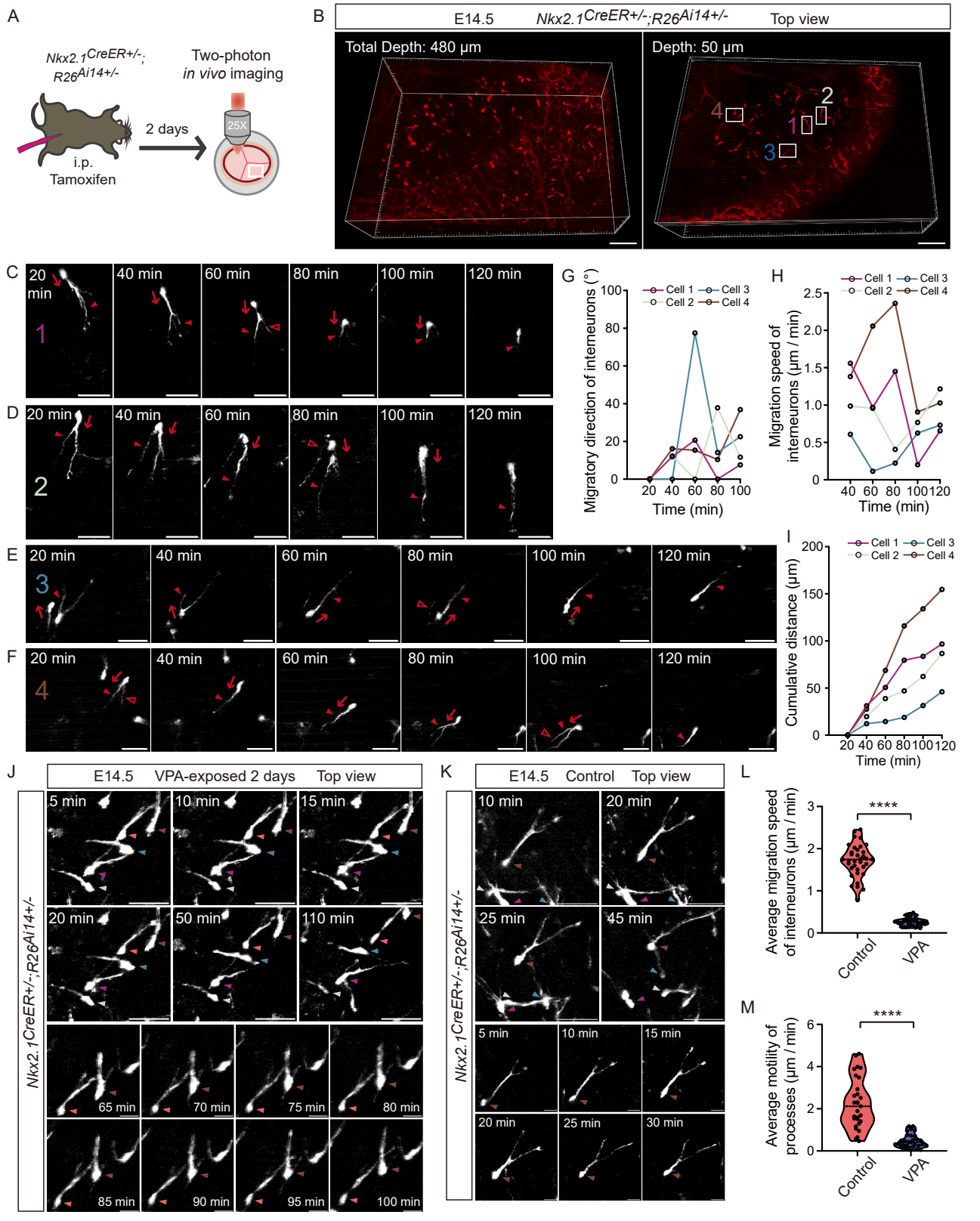

(legend on next page)

Figure S4. Intravital imaging of sparsely labeled interneurons, depicting their migration patterns in the developing mouse cortex, related to Figure 4

(A) Endogenous labeling of MGE-derived cortical interneurons and two-photon *in vivo* imaging.

(B) The top view *in vivo* image stack of MGE-derived cortical interneurons at E14.5 (z = 480 μm; left), and the cross-section at a 50 μm depth (right). Scar bars, 200 μm.

(C–F) Representative *in vivo* time-lapse sequences showing tangential migration of four cortical interneurons, marked in Figure S5B. Arrows, migratory directions; solid arrowheads, leading process branches that guide the migratory direction of interneurons; and hollow arrowheads, leading process branches that retract during the interneuron migration. Scar bars, 100 μm.

(G–I) Quantification of the changes of migratory directions (G), cumulative distances (H), and migration speed (I) of interneurons shown in Figure S5B.

(J and K) Representative *in vivo* time-lapse sequences showing tangential migration of cortical interneurons in the VPA-exposed embryos (J) and the controls (K) at E14.5. Scale bars, 50 μm (upper panels) and 20 μm (lower panels).

(L) Quantification of the average migration speed of interneurons in control and VPA-exposed embryos (n = 35 cells per group; 2 embryos from 2 dams per group).

(M) Quantification of the average motility of interneuron processes in control and VPA-exposed embryos (n = 29 cells per group; 2 embryos from 2 dams per group).

Data: violin plots (L and M). Statistics: Mann-Whitney U test; ****$p < 0.0001$.

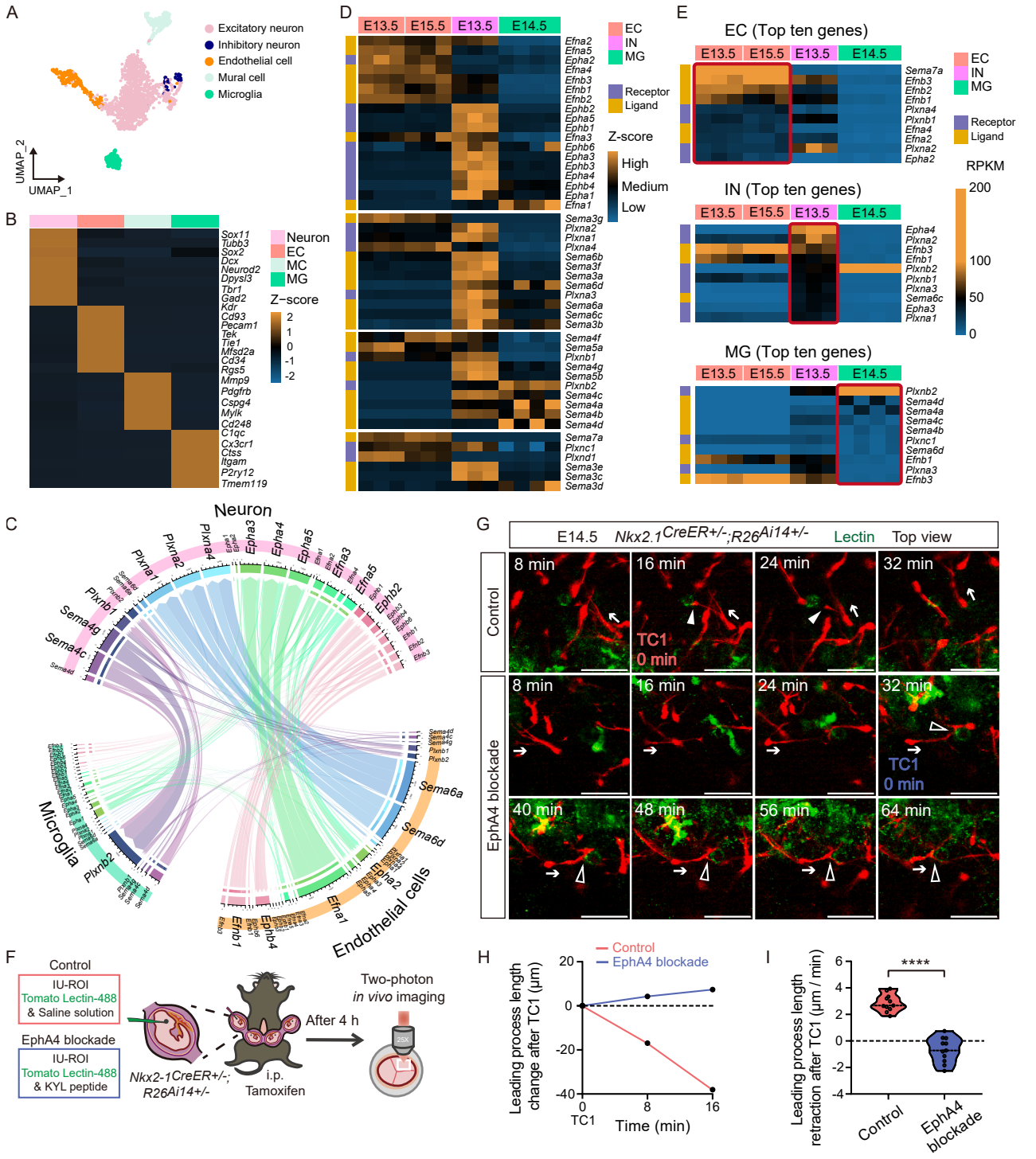

Figure S5. The expression profiles and functional roles of chemorepulsive cues in the cell-cell interactions, related to Figures 4 and 5

(A) Visualization of different cell clusters by uniform manifold approximation and projection (UMAP).

(B) Heatmap illustrating differentially expressed genes (DEGs) enriched in each cluster.

(C) Ligand-receptor pairing patterns of the Eph-ephrin and plexin-semaphorin (Plxn-Sema) signaling families among embryonic neurons, microglia, and endothelial cells.

(D) Heatmap depicting the expression profiles of the Eph-ephrin and Plxn-Sema signaling families among embryonic interneurons, microglia, and endothelial cells.

(E) Heatmaps of the top 10 enriched genes from the Eph-ephrin and Plxn-Sema signaling families in embryonic endothelial cells, interneurons, and microglia.

(legend continued on next page)

(F) Endogenous labeling of MGE-derived cortical interneurons, followed by vascular labeling (lectin-488) and EphA4 blockade (KYL peptide) by IU-ROI, and two-photon *in vivo* imaging after 4 h.

(G) Representative *in vivo* time-lapse sequences showing the interactions between tangentially migrating interneurons with blood vessels in control and EphA4 blockade groups at E14.5. Arrows, migratory directions. Solid arrowheads indicate the TC1 of an interneuron with a blood vessel and the subsequent branch retraction in control, while hollow arrowheads indicate that an interneuron made TC1 with a blood vessel and subsequently wrapped around this blood vessel in the EphA4-blockade group. Scar bars, 50 μm.

(H) Quantification of leading process length change in interneurons (shown in Figure S6G) following TC1 with blood vessels.

(I) Quantification of leading process length retraction per minute following the TC1 of interneurons with blood vessels in the control and the EphA4-blockage groups (n = 11 cells per group; 2 embryos from 2 dams per group).

Data: violin plots (I). Statistics: Mann-Whitney U test; $^{****}p < 0.0001$.

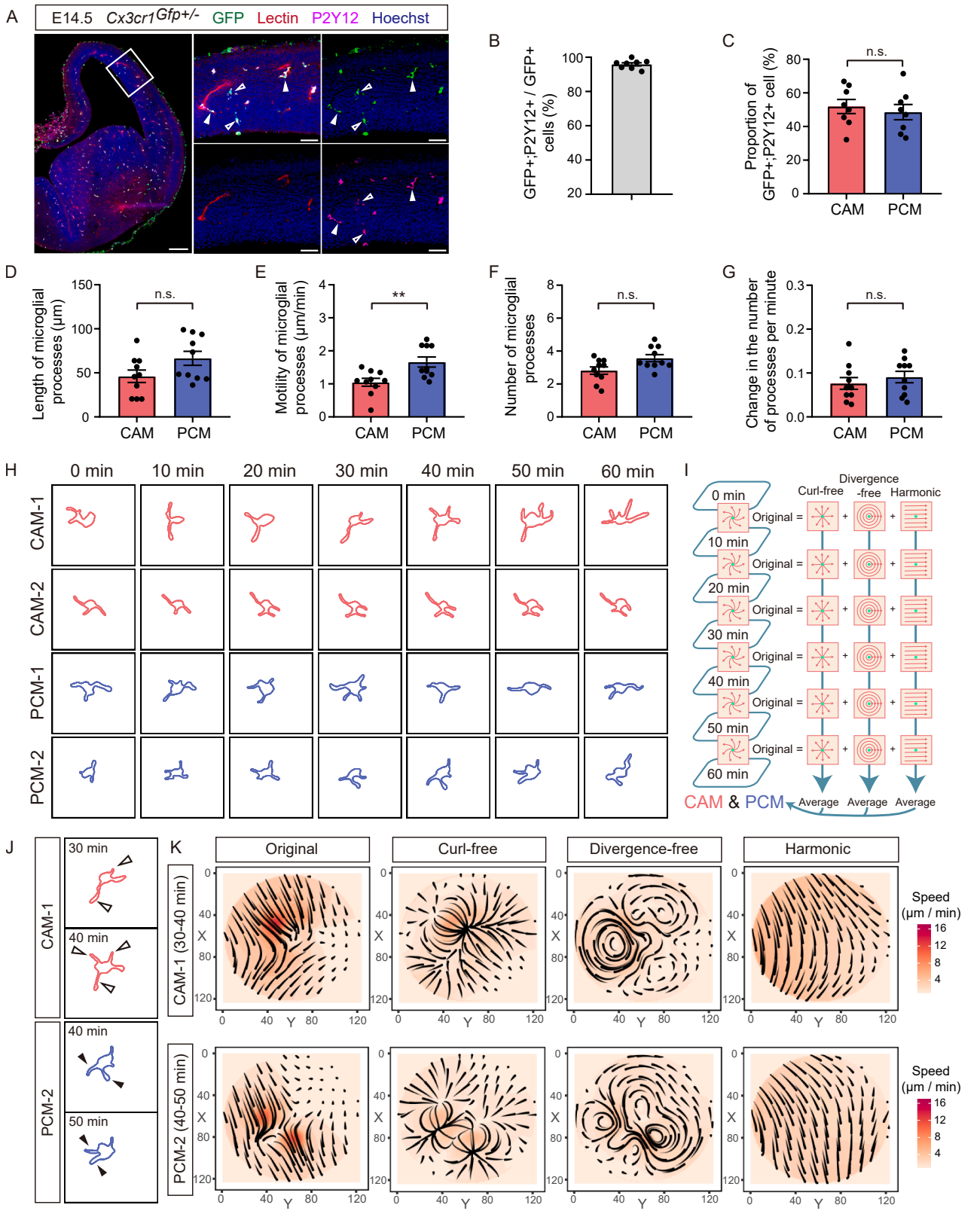

(legend on next page)

Figure S6. The analysis of dynamic motions of CAMs and PCMs in the developing mouse cortex, related to Figure 6

(A) Coronal sections of the E14.5 *Cx3cr1*$^{GFP+/-}$ brains were labeled by lectin-594 (red) and were stained for GFP (green), P2Y12 (purple), and Hoechst (blue). Solid arrowheads, CAMs; hollow arrowheads, PCMs. Scale bars, 200 μm (left) and 50 μm (middle and right).

(B) Quantification of the proportion of GFP$^+$P2Y12$^+$ cells in all GFP$^+$ cells (n = 8 embryos from 2 dams).

(C) Quantification of the proportion of CAMs and PCMs in the GFP$^+$P2Y12$^+$ cells (n = 8 embryos from 2 dams).

(D–G) Quantification of the process length (D), process motility (E), process number (F), and change in the number of processes per minute (G) of CAMs and PCMs (CAM, n = 10 cells; PCM, n = 10 cells; 2 embryos from two dams). Data presented for each cell are the averaged value of measurements collected every 10 min within a 1-h time window of *in vivo* imaging.

(H) The morphological profiles of CAMs and PCMs in a 1-h time-lapse sequence.

(I) Schematic illustration of the TVF analysis for each microglial cell.

(J) Representative morphological profiles of CAMs and PCMs at two adjacent time points.

(K) The original vector fields constructed by microglial motions at two adjacent time points, shown in Figure S6J, and their three decomposed components: curl-free, divergence-free, and harmonic vector fields.

Data: mean ± SEM. Statistics: Mann-Whitney U test; $^{**}p < 0.01$, n.s., non-significant ($p > 0.05$).

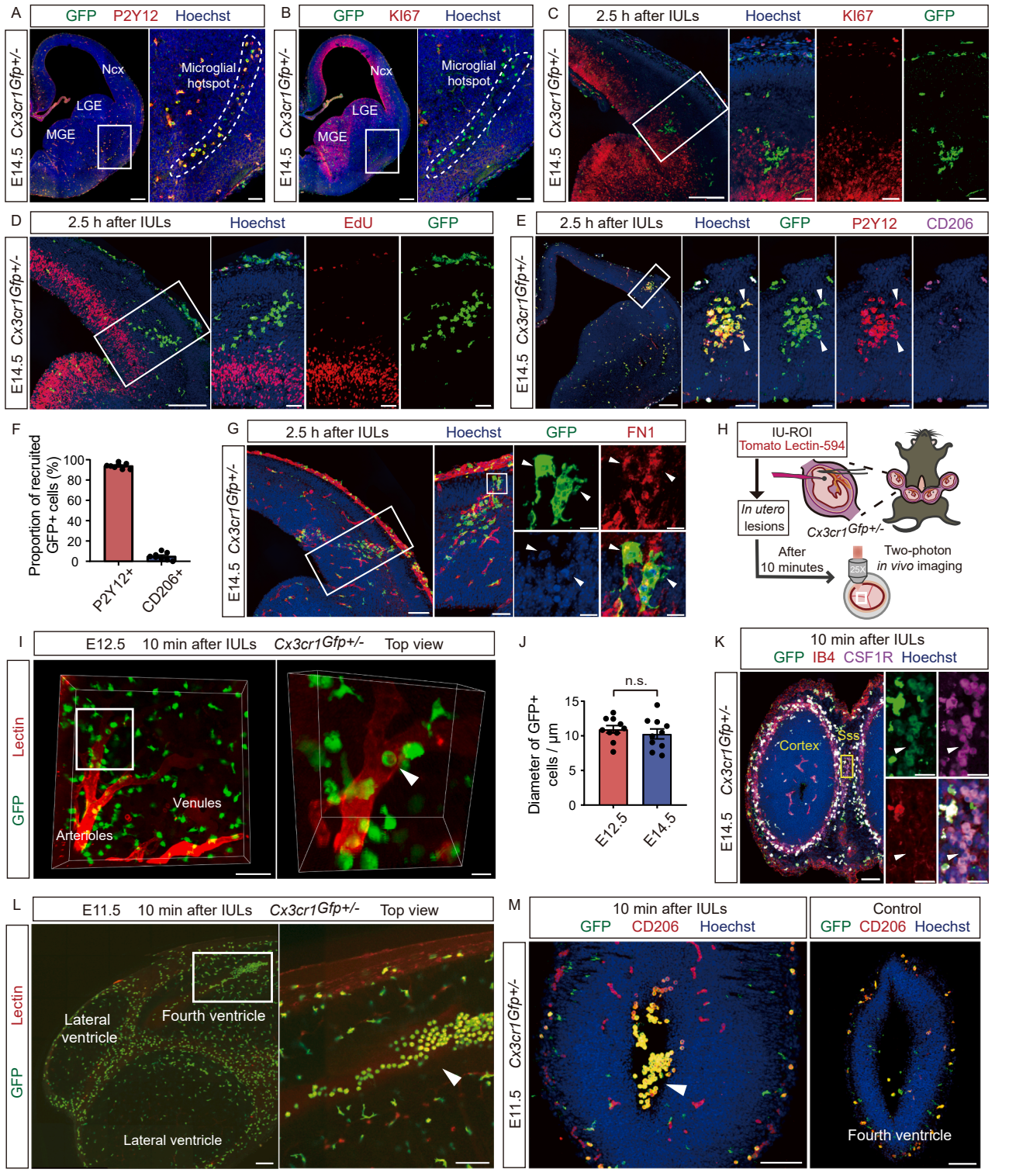

Figure S7. The recruitment of immune cells in the brain in response to the environmental stress, related to Figure 7

(A and B) Coronal sections of the E14.5 *Cx3cr1*$^{GFP+/-}$ brains were stained for GFP (green), P2Y12 (red), and Hoechst (blue) (A); and GFP (green), KI67 (red), and Hoechst (blue) (B). The marked regions indicate the microglial hotspots at the CSA. Scale bars, 200 μm (left) and 50 μm (right).

(C–E and G) Coronal sections of the E14.5 *Cx3cr1*$^{GFP+/-}$ brains were acquired 2.5 h after IULs and were stained for GFP (green), KI67 (red), and Hoechst (blue) (C); GFP (green), EdU (red), and Hoechst (blue) (D); GFP (green), P2Y12 (red), CD206 (purple), and Hoechst (blue) (E); and GFP (green), FN1 (red), and Hoechst (blue) (G). Arrowheads indicate the GFP$^+$P2Y12$^+$ cells (E) and the FN1$^+$GFP$^+$ cells (G). Scale bars, 200 μm (first columns) and 50 μm.

(legend continued on next page)

(F) Quantification of the proportion of P2Y12$^+$ microglia and CD206$^+$ border-associated macrophages in the recruited GFP$^+$ cells at the lesion sites (n = 8 embryos from 2 dams).
(H) Endogenous labeling of microglia and IU-ROI labeling of blood vessels followed by IULs and subsequent two-photon *in vivo* imaging.
(I) The top view *in vivo* image stack of pial vasculature and CX3CR1$^+$ cells 10 min after IULs at E12.5 (z = 110 μm). Arrow, monocyte in the pial arterioles. Scale bars, 100 μm (left) and 20 μm (right).
(J) Quantification of the diameter of GFP$^+$ cells flowing in the pial vasculature of E12.5 and E14.5 embryos 10 min after IULs (n = 10 cells per group; 2 embryos from 2 dams per group).
(K) A representative horizontal section of E14.5 *Cx3cr1*$^{GFP+/-}$ brains that were acquired 10 min after IULs and were stained for GFP (green), IB4 (red), CSF1R (purple), and Hoechst (blue). Arrowheads, GFP$^+$CSF1R$^+$ cells in the Sss. Scale bars, 100 μm (first columns) and 20 μm.
(L) The top view *in vivo* images of brain ventricles and CX3CR1$^+$ cells 10 min after IULs at E11.5. Arrowhead indicates the accumulation of CX3CR1$^+$ macrophages in the fourth ventricle. Scale bars, 200 μm (left) and 100 μm (right).
(M) Representative horizontal sections of E11.5 *Cx3cr1*$^{GFP+/-}$ brains that were acquired 10 min after IULs versus the controls. Brains were stained for GFP (green), CD206 (red), and Hoechst (blue). Arrowheads indicate the accumulated GFP$^+$CD206$^+$ cells in the fourth ventricle. Scale bars, 100 μm.
Data: mean ± SEM. Statistics: Mann-Whitney U test; n.s., non-significant (p > 0.05).